Spin-Polarized Atomic Hydrogen

an experimental study

ACADEMISCH PROEFSCHRIFT

ter verkrijging van de graad van
doctor aan de Universiteit van Amsterdam
op gezag van de Rector Magnificus
dr S.K. Thoden van Velzen,
hoogleraar in de Faculteit der Tandheelkunde,
in het openbaar te verdedigen in de Aula der Universiteit
(Oude Lutherse Kerk, ingang Singel 411, hoek Spui)
op woensdag 16 september 1987 te 15.00 uur precies

door

AUGUSTINUS PETRUS MARIA MATTHEY

geboren te Arnhem

1987
druk: krips repro meppel

Promotor: Prof. Dr. I.F. Silvera
Co-promotor: Dr. J.T.M. Walraven

The work described in this thesis was carried out at the
"Natuurkundig Laboratorium" of the University of Amsterdam
and supported financially by the
"Stichting voor Fundamenteel Onderzoek der Materie" (FOM).

Aan Johanna en Thomas

CONTENTS

Introduction

Spin polarized atomic hydrogen is an attractive substance to create and to study. The hydrogen atom, consisting of two tightly bound Fermions (the electron with spin S = 1/2, and the proton with spin I = 1/2) behaves as a composite boson. A collection of spin polarized hydrogen atoms is expected to display fascinating phenomena, the most prominent being its gaseous nature, even at zero temperature, and Bose-Einstein condensation (BEC) and related superfluid behavior[1]. Apart from the statistical nature of the hydrogen atom, these properties originate from its low atomic mass, resulting in a large zero point motion, and the weak interatomic interactions.

London[2] showed in 1938 that in a non-interacting gas of Boson particles, a transition occurs at a critical density, where the lowest momentum state is macroscopically populated. The role of the interactions was explored in a series of papers by Lee, Huang and Yang[3], dealing with the properties of a gas of weakly interacting boson spheres. Although it is generally believed that some connection exists between superfluid behavior and BEC, it was never possible to establish this connection into a clear picture. Liquid helium-4, becoming a superfluid below a temperature of 2.17 Kelvin, condenses under its own vapor pressure. In the gaseous phase, the density is too low for BEC to occur, and in the liquid phase the effects of the interatomic interactions mask the relation between BEC and superfluid behavior. The low atomic mass and the weak interatomic interactions make spin-polarized atomic hydrogen the ideal substance to study the properties of a weakly interacting Bose gas as the density is not limited by condensation into the liquid state.

A gas of atomic hydrogen of substantial density is not provided by nature, as it is highly unstable due to the recombination reaction $H + H \rightarrow H_2$. As first pointed out by Hecht in 1959[4], this reaction may be surpressed by polarizing the atoms in a strong magnetic field at low temperature. His suggestion had to await realization until 1979, when Silvera and Walraven stabilized spin-polarized atomic hydrogen for the first time in observable quantities [5]. This experiment marks the launching of a new field of research, showing that polarizing the atoms increased the stability of the gas by many orders of magnitude. However, this was insufficient to bring the maximum density into the BEC range. Furthermore, it showed that covering the walls of the chamber, containing the sample, with a thin coating of liquid helium-4 is essential. In the following years, most of the efforts were directed towards getting an understanding of the destabilization processes.

This thesis work may be considered as being a part of these efforts. Of particular interest was the study of the role of the liquid helium surface, surrounding the sample. As hydrogen atoms are weakly bound to the surface of the liquid, a small fraction of the gas condenses to the surface at low temperatures. However, the collision frequency is high due to the lack of the third dimension. Furthermore, the recombination of H towards H_2 needs the assistance of a third body, which is available at the surface in large quantities in the form of helium atoms. Thus the surface may catalyse recombination of hydrogen atoms towards the molecular state or cause magnetic relaxation, which often appears as an intermediate step. A systematic investigation has been carried out of the destabilisation processes as a function of temperature and magnetic field.

This thesis is organized as follows. In chapter I the theoretical concepts underlying the experiments will be reviewed. Chapter II deals with techniques, particularly those that were developed in the course of this work. Chapter III gives a description of the various experiments, together with their results and interpretation. A separate chapter is devoted to microwave pumping experiments using ESR.

References

1. I.F. Silvera, J.T.M. Walraven, *Progress in Low Temperature Physics* vol. X, D.F. Brewer, Ed., North Holland Publishing Co., Amsterdam.
2. F. London, Phys. Rev. 54, 947; Nature 141, 663 (1938).
3. T.D. Lee, K. Huang and C.N. Yang, Phys. Rev. 106, 1135 (1957) and references therein.
4. C.E. Hecht, Physica 25, 1159 (1959).
5. I.F. Silvera and J.T.M. Walraven, Phys. Rev. Lett. 44, 107 (1980).

CHAPTER I OVERVIEW

Introduction

In this chapter, the concepts underlying the stability of spin polarized hydrogen will be reviewed. Much of the material covered is the subject of the experimental investigations to be described in later chapters. With the appearance of review articles at regular time intervals and increasing size[1-3], no attempt was made to aim for completeness.

The first two sections deal with static properties of atomic hydrogen. In section 1.1, single atom properties and pair interactions will be treated. Interactions between the atom and the liquid helium-4 surface are covered in section 1.2. The last two sections describe dynamical processes, limiting the stability. Section 1.3 contains a review of the relevant mechanisms, and in section 1.4 the material contained in the preceding sections is brought into a form that may be compared with experimental results.

1.1 Atomic states and interatomic potentials

The magnetic energy levels of an isolated hydrogen atom in its ground state may be found by diagonalizing the spin Hamiltonian

$$H = g_e \mu_B S_z B_z - g_N \mu_N I_z B_z + a\,\vec{I}.\vec{S} \qquad (1.1)$$

The first two terms stand for the electronic and nuclear Zeeman energy, S_z and I_z are the components of the electronic and nuclear spin operators along the direction of the applied magnetic field B, μ_B is the Bohr magneton and μ_N the nuclear magneton; the electronic and nuclear g factors are denoted by g_e and g_n, and are both defined as being positive. The last term in the Hamiltonian represents the hyperfine interaction with coupling constant ($a/h = 1420$ MHz, $a/k_B = 68$ mK). The eigenstates of this Hamiltonian, labeled $|a\rangle$, $|b\rangle$, $|c\rangle$ and $|d\rangle$, are in increasing order of energy

$$|a\rangle = -\cos\theta\ |\downarrow\Uparrow\rangle + \sin\theta\ |\uparrow\Downarrow\rangle \qquad (1.2\ a)$$

$$|b\rangle = |\downarrow\Downarrow\rangle \qquad (1.2\ b)$$

$$|c> = \cos\theta \;\; |\uparrow\text{↧}> + \sin\theta\,|\downarrow\text{↥}> \qquad (1.2\ c)$$

$$|d> = \;\; |\uparrow\text{↥}> \qquad (1.2\ d)$$

where ↑ (↥) refers to an electron (proton) spin up state. The hyperfine mixing parameter $\epsilon = \sin\theta$ is given by:

$$\epsilon = \{1 + [\mu^+B/a + (1 + (\mu^+B/a)^2)^{\frac{1}{2}}]^2\}^{-\frac{1}{2}} \qquad (1.3)$$

where $\mu^{\pm} = g_e\mu_B \pm g_N\mu_N$. In high fields ($B \gg a/\mu^+ = 506.2$ Gauss) this expression may be simplified giving $\epsilon \propto a/(2\mu^+B)$. In zero field, $\epsilon = \frac{1}{2}\sqrt{2}$.
In strong magnetic fields and at sufficiently low temperatures, only the |a> and |b> states are thermally populated. Such a spin-polarized two component mixture has a greatly enhanced stability against recombination, and is referred to as spin polarized hydrogen (H↓). The |b> states and |d> states are pure Zeeman states. Due to the hyperfine interaction, an amount ϵ of the other electron spin orientation is mixed into the |a> and |c> states. The probability of finding a spin up |a> state atom is given by ϵ^2. In a 10 Tesla field, ϵ^2 has a value of $6.4*10^{-6}$. Complete electron spin polarization in a strong field is therefore inhibited due to this admixture. This admixture plays a key role in the recombination of two hydrogen atoms towards the molecular state.

The energies of the atomic states are given by

$$E_a = -(a/4)\;[1 + 2(1 + (\mu^+B/a)^2)^{\frac{1}{2}}] \qquad (1.4\ a)$$

$$E_b = +(a/4)\;[1 - 2(\mu^-B/a)] \qquad (1.4\ b)$$

$$E_c = -(a/4)\;[1 - 2(1 + (\mu^+B/a)^2)^{\frac{1}{2}}] \qquad (1.4\ c)$$

$$E_d = +(a/4)\;[1 + 2(\mu^-B/a)] \qquad (1.4\ d)$$

The energies are shown in fig. 1.1 as a function of magnetic field, together with the allowed ESR and NMR transitions.

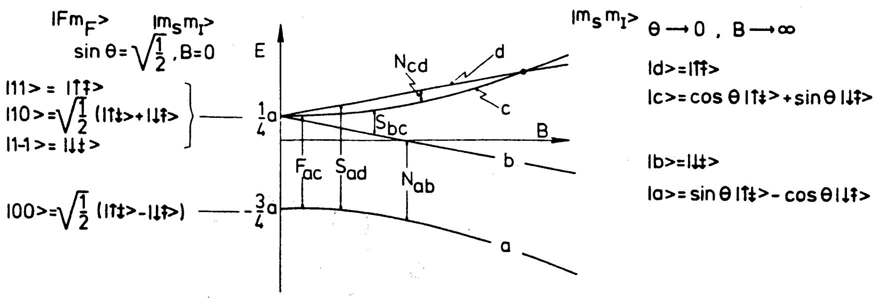

Fig. 1.1 Hyperfine levels of H in a magnetic field. Also shown are the possible electronic (S), nuclear (N) and longitudinal (F) magnetic resonance transitions (after Silvera and Walraven[1]*).*

The interaction between a pair of hydrogen atoms is represented by an effective Hamiltonian of the form

$$H_{int} = H_D + H_{exch} + H_{dd} \tag{1.5}$$

where H_D and H_{ex} are the direct and exchange interactions between the atoms, and H_{dd} is the interaction due to magnetic dipole forces. The last term is much weaker than the other terms. Accurate ab initio calculations of H_D + H_{exch} were made by Kolos and Wolniewicz[4]. The potential depends on the total spin of the electrons $S = s_1 + s_2$. Leaving aside the weak intra-atomic hyperfine interactions, one may distinghuish two potentials; in the electronic ground state this leads to the ${}^1\Sigma_g^+$ or singlet potential V_S, if the electronic spin state is antisymmetric ($S = 0$), and the ${}^3\Sigma_u^+$ or triplet potential V_T for the symmetric electronic spin state ($S = 1$). The singlet and triplet potentials are shown in fig. 1.2.a and 1.2.b. The singlet potential has a bound state with a dissociation energy of 36118.6±0.2cm^{-1} [14,15], making a sample of atomic hydrogen highly unstable against molecule formation in zero magnetic field. The triplet potential has a shallow minimum of 6.46 Kelvin at an interatomic separation of 4.16 Å, which is insufficient to support a bound state. In a magnetic field, the degeneracy of the triplet state is lifted, and one of the triplet potentials is partially shifted below the singlet potential. Polarization of the electronic spins in a strong field in combination with sufficiently low temperatures, forces the atoms to interact pairwise via the triplet potential. This strongly surpresses

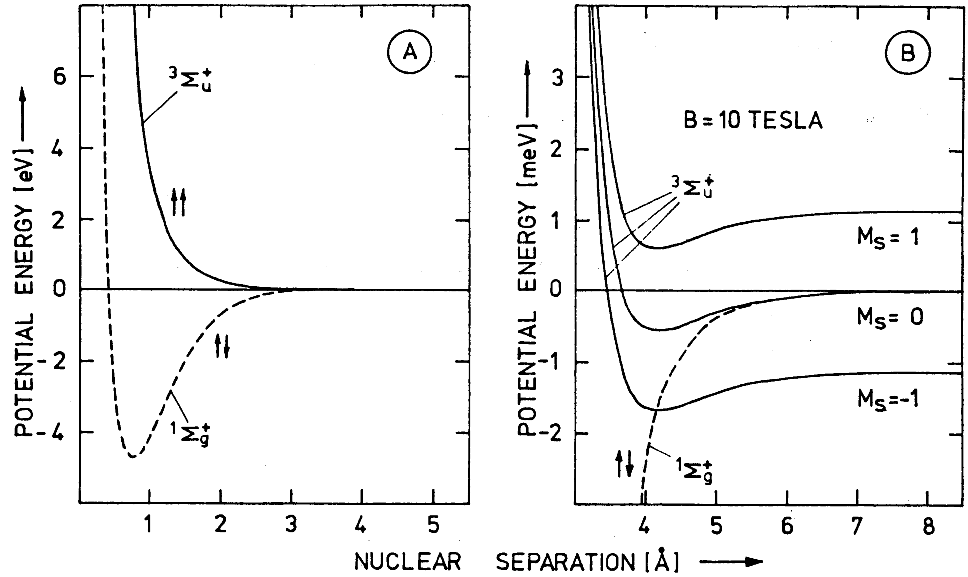

Fig. 1.2 Interatomic potentials for a pair of hydrogen atoms in the singlet (dashed line) and triplet (solid line) states in zero field (a) and in a field of 10 Tesla (b). Note the expanded scale in fig. 1.2.b (after Silvera and Walraven[1]).

recombination.

In terms of the triplet and singlet potentials V_T and V_S one may write:

$$H_D + H_{exch} = {}^{\wedge}{}_{D}(r_{12}) + J(r_{12})\ \vec{s}_1 \cdot \vec{s}_2 \qquad (1.6)$$

where $V_D = (1/4)(V_S + 3V_T)$ and $J = V_T - V_S$.

The magnetic dipole-dipole interactions are represented by the Hamiltonian:

$$H_{dd} = (\mu_0 \hbar^2 / 8\pi r_{12}^3) \quad [\gamma_e^2 f(\vec{s}_1, \vec{s}_2)$$

$$- \gamma_e \gamma_n \, (f(\vec{s}_1, \vec{i}_2) + f(\vec{s}_2, \vec{i}_1)) + \gamma_n^2 \, f(\vec{i}_1, \vec{i}_2)] \qquad (1.7\ a)$$

where $f(\vec{s}, \vec{i}) = \vec{s} \cdot \vec{i} - 3(\vec{s} \cdot \hat{r}_{12}) \cdot (\vec{i} \cdot \hat{r}_{12}) \quad . \qquad (1.7\ b)$

Here $\hat{r}_{12}$ is a unit vector. The nucleon-nucleon term is small compared to the electron-electron and electron-nucleon interactions; usually it is neglected.

1.2 Interactions of H with the helium surface

The role of the surface proved to be of critical importance in stabilization experiments. If the atoms are strongly bound to the surface, a high surface density builds up, which severely limits the stability of the gas. In the early experiments [5, 28, 29] it was established that covering the sample chamber walls with liquid helium is essential. Liquid helium provides an almost ideal surface: it has a low binding energy for atomic hydrogen and is essentially free from contaminations. Hydrogen molecules, which are the product of the recombination reaction, were found to enter the bulk liquid [6], eventually becoming a part of the solid substrate underneath the liquid. The adsorption isotherm is of primary importance, as it reveals the role of the surface in attaining BEC.

The basic ingredient for the binding of a hydrogen atom to the liquid is the H-He Van der Waals potential. A calculation of the binding energy has to take into account the surface density profile of the liquid and the many body nature of the problem, in particular the H-He density correlations. Neither the surface density profile, nor the H-He correlation function is precisely known. Theoretical estimates of the binding energy were made by Guyer and Miller [7], Mantz and Edwards [8] and De Simone and Maraviglia [9]. Here we follow the calculations of Mantz and Edwards in some detail. They used a variational approach, based upon Feynman [30] and Lekner [31], that had been succesfully applied to predict the binding of helium-3 atoms to the free surface of helium-4 [32]. In this method, knowledge of the ground state wave function $\Psi_o(\vec{r}_1,\vec{r}_2,.......,\vec{r}_N)$ is assumed of a system of N helium atoms with coordinates $\vec{r}_1,....,\vec{r}_N$. The hydrogen atom is treated as an impurity. As the true He-H correlation function is unknown, it is assumed to have the same correlations as the helium atom. The helium atom with coordinate $\vec{r}_1$ is replaced by a hydrogen atom, and a trial wavefunction of the form

$$\Psi(\vec{r}_1,......,\vec{r}_N) = f(\vec{r}_1)\ \Psi_o(\vec{r}_1,.....,\vec{r}_N) \tag{1.8}$$

is used to minimize the energy by variation of $f(\vec{r}_1)$. The minimalization procedure yields a single particle Schrödinger equation for the motion

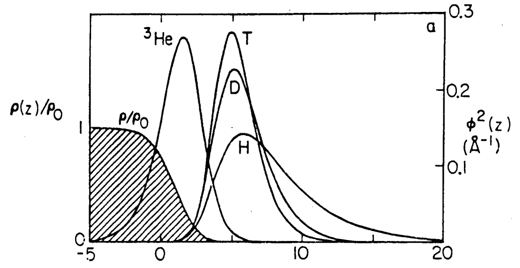

Fig. 1.3.a Calculated density profiles for ^3He and the hydrogen isotopes adsorbed on the liquid ^4He surface. Also shown is the ^4He density distribution ρ/ρ_0.

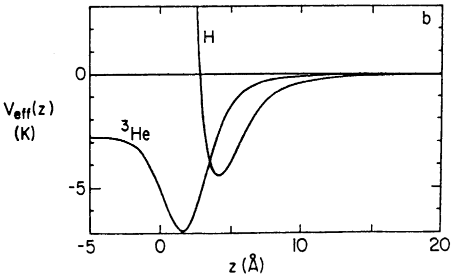

Fig. 1.3.b Effective potentials for H and ^3He (after Mantz and Edwards [8]).

perpendicular to the surface:

$$-(\hbar^2/2m)d^2\varphi(z)/dz^2 + V_{eff}(z)\varphi(z) = E_z\ \varphi(z) \qquad (1.9)$$

where m is the mass of the hydrogen atom, z the distance to the surface, E_z the bound state energy and $\varphi(z) = f(z).(\rho(z)/\rho_0)^{1/2}$ is an effective single particle wavefunction; $\rho(z)/\rho_0$ is the normalized density distribution of the liquid in the ground state. The motion of the hydrogen atoms along the surface is free particle like. The effective potential V_{eff} depends on the one particle, two particle and kinetic energy densities of the liquid in the ground state, and the H-He and He-He potentials. The resulting potential for hydrogen, together with the density distributions for the hydrogen isotopes is shown in figs. 1.3 a and b. The potential yields a single bound state for hydrogen, having a binding energy of 0.63 Kelvin. In view of the uncertainties involved in the calculation, the agreement with the experimentally determined value of 1 Kelvin is reasonable.

In the low density limit, the effects of Bose statistics and interactions between the hydrogen atoms may be neglected. The adsorption isotherm is then given by

$$n_s = n_v \lambda_{th} \exp [E_A/k_BT] \tag{1.10}$$

where n_s is the density at the surface, n_v is the density in the bulk, $\lambda_{th} = (2\pi\hbar^2/mk_BT)^{\frac{1}{2}}$ is the thermal de Broglie wavelength. The isotherm, neglecting interactions between the hydrogen atoms yields unrealistic results at high surface densities. Due to the effect of Bose statistics, the surface density diverges if the chemical potential μ approaches zero. As $\mu = 0$ is also the condition for the onset of BEC in the bulk, BEC in this noninteracting two phase system is impossible. The inclusion of interactions between the hydrogen atoms changes this picture drastically. Calculations on the effect of interactions on the adsorption isotherm were carried out by Silvera and Goldman [10] and Edwards and Mantz[11]. In a linear density expansion, the chemical potentials in the volume and at the surface may be written

$$\mu_v = \mu_{v0} + 2\ \alpha_3\ n_v, \text{ and } \mu_s = \mu_{s0} + 2\ \alpha_2\ n_s \tag{1.11}$$

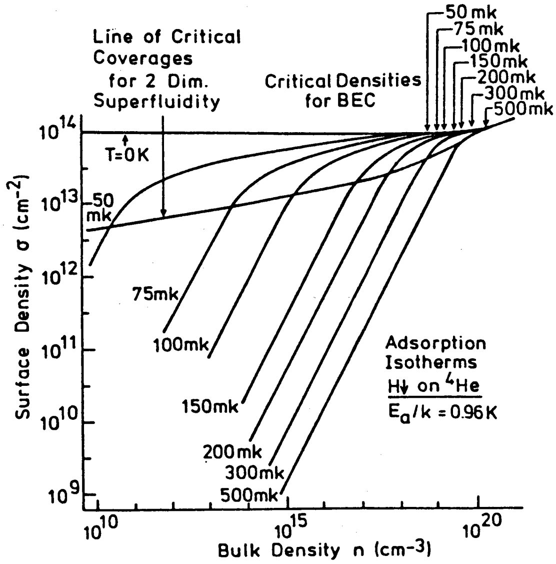

Fig. 1.4 Adsorption isotherms of H on liquid ^{4}He (after Silvera and Walraven[1]).

where μ_V and μ_S are the chemical potentials in the volume and at the surface, μ_{V0} and μ_{S0} are the chemical potentials neglecting interactions and α_2 and α_3 are the linear coefficients in the density expansion of the interaction energy. The resulting isotherms are shown in fig. 1.4 for several temperatures. Interactions may be neglected at surface densities of $5 * 10^{12}$ cm^{-2} and below, depending on temperature; at BEC conditions in the gas the surface is saturated at an estimated density of about $10^{14} cm^{-2}$ for a ^4He surface and $3.10^{13} cm^{-2}$ for a ^3He surface[1].

1.3 *Decay processes in gaseous and adsorbed hydrogen*

A sample of atomic hydrogen has a finite lifetime due to the formation of hydrogen molecules. Recombination is the last stage in a reaction chain, which also may involve one or more relaxation steps. Sometimes the decay rate is influenced by transport of atoms to a certain region in the experimental system, where recombination is likely to occur. In the case that one of these steps is rate determining, the density decay rate becomes proportional to a simple power (r) of the number density (n) of the gas:

$$dn/dt = - K n^r \tag{1.12}$$

Here K is the rate constant and r corresponds to the number of hydrogen atoms, that participate in the rate limiting reaction (r = 1, 2 or 3).

Recombination of atomic hydrogen has been widely covered in the chemical literature during the past fifty years. Recent studies of this elementary reaction, encouraged by the need to find the best strategy towards stabilizing high densities at low temperatures, has revealed a wealth of possible new routes to the molecular state. Thus far, more than one hundred relaxation and recombination channels have been identified. These processes may be classified according to the type of interaction that is responsible for the reaction (exchange or dipolar interaction) or to the nature of the species that catalyses the process (a helium atom or hydrogen atom in the gaseous phase, or the liquid helium surface). In the coming section a brief description will be given, with some emphasis on processes that are effective at moderate densities ($\sim10^{14}$-10^{16}/cc).

1.3.1 Recombination

In practice the formation of a hydrogen molecule from a pair of atoms always needs the assistance of a third body, either in a single ternary collision or two consecutive binary collisions. The two body process

$$H + H \rightarrow H_2 + h\nu$$

requires the release of the dissociation energy by the emission of radiation. This however is prohibited, due to the absence of a permanent dipole moment in the molecule. The role of the third body is to provide extra degrees of freedom to obey the conservation laws of energy and momentum. It may be useful to spend a few sentences on standard room temperature recombination. In this case, the reaction proceeds in two steps. A possible mechanism is

$$H + X \rightarrow (HX)^*$$

$$(HX)^* + H \rightarrow H_2 + X$$

where $X \neq H$. In the first step, a metastable molecule $(HX)^*$ is formed; the last stage is an exchange reaction. The dominant process at ambient temperatures is resonance recombination, also following a two step scheme:

$$H + H \rightarrow (H_2)^*$$

$$(H_2)^* + X \rightarrow H_2 + X$$

where $X = H$ or some different species. In the first stage, a metastable molecule having an energy above the dissociation limit is formed. This process is resonant in the sense that it requires a close matching between the incoming energy of the recombining atoms and the vibrational-rotational energy of the quasimolecule. The quasimolecule may be stabilized by energy transfer, if it collides with some particle X before it can dissociate.

The exchange mechanism is not effective at temperatures below 1 Kelvin, as the only relevant candidates for X, the helium isotopes, do not form a quasi bound state with H. Several authors explored the possible relevance of resonance recombination at temperatures below 1 Kelvin. The majority of the

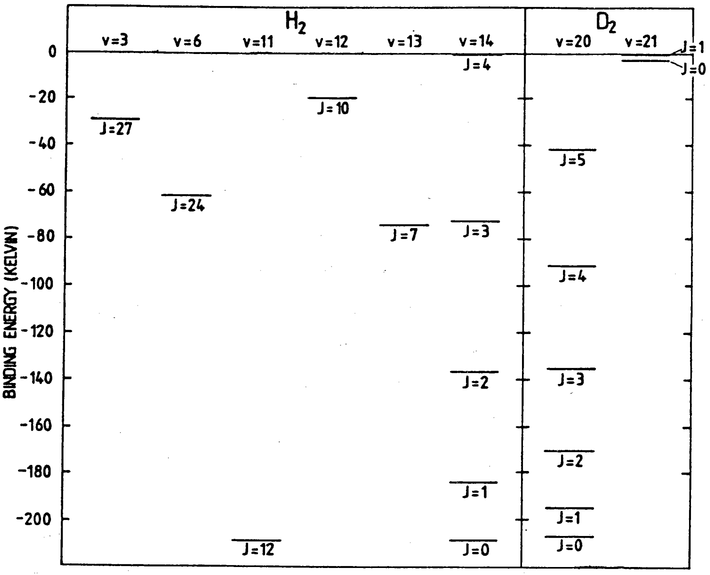

Fig. 1.5 Vibrational-rotational energy levels of the H_2 *molecule near the dissociation limit (after Silvera and Walraven* [1]*).*

quasi-molecular states, which are important at high temperatures, turn out to be thermally inaccessible in the low temperature regime. In fig 1.5 we depict some vibrational rotational levels with an energy near the dissociation limit. These bound molecular states may become quasibound by applying a magnetic field. This is due to triplet-singlet mixing. As pointed out by Stwalley [12], some of these states may be tuned above threshold by the application of a magnetic field, shifting the $M_S = -1$ asymptote of the triplet potential below the corresponding level. The resonance condition will be fulfilled for those pairs, having a kinetic plus Zeeman energy that coincides with the energy of the bound state. The v=12, J=10 level was considered within this context by Kagan, Vartanyantz and Shlyapnikov[13]. This state is accessible at fields > 14.6 Tesla. This channel however is expected to be unimportant for the following reason. Apart from energy constraints, also the existence of a centrifugal barrier governs the dynamics of the process. After separating out the center of mass motion, the Schrödinger equation for the pair takes the form

$$[-(\hbar^2/2\mu)\ d^2/dr^2 + V(r) + J(J+1)\ \hbar^2/(2\mu r^2)]\ Y_J(r) = E\ Y_J(r) \qquad (1.13)$$

where $\mu = m/2$ is the reduced mass of the pair, $r = |r_1 - r_2|$, and V(r) may be the singlet potential or the triplet potential. The effective potential between the two atoms depends on the rotational quantum number J, an effect which is characteristic for any central potential. The J-dependent term provides a rotational barrier, which may be appreciable at high J values, preventing an encounter, close enough to form a molecule.

The v=14, J=4 level was considered in detail recently [14] in relation to experimentally observed rates. From spectroscopic measurements it is known to be marginally bound, having an energy of .26(46) Kelvin below the dissociation limit[15]. The level is inaccessible at zero field[16], but opens a channel to recombination for pairs of |a> state atoms at fields of 0.52 Tesla and above. The quasimolecule is calculated to have a lifetime of 10 microseconds before it dissociates. In the limit, where the loss of atoms is bottlenecked by the formation of $(H_2)^*$, the rate constant is given by [14]

$$K^B_{aa} = 2\surd 2(\lambda^3_{th}/\tau)\exp[-(\Delta - D_{14,4})/k_BT)] \qquad (1.14)$$

where Δ is the Zeeman energy of the pair and $D_{14,4}$ the dissociation energy of the quasimolecule. The exponential threshold factor reflects the energy constraints, posed by the resonance condition. Experimentally observed rates consistent with this relation were observed at relatively high temperatures, a field of 4 Tesla and densities of order $10^{15}/cm^3$. The experimental data yield a value of 0.7 (0.1) Kelvin for the dissociation energy $D_{14,4}$, which is more accurate than the spectroscopically determined value. It is also possible to give an improved value of the ground state dissociation energy $D_{0,0}$ of 36118.6 (0.2) cm^{-1}, as the source of uncertainty in $D_{0,0}$ results from the uncertainty in $D_{14,4}$.

The dominant process at low temperatures is the direct process, involving three bodies in a single encounter:

$$H + H + X \rightarrow H_2 + X$$

where X may be either H in the gaseous phase or in a surface bound state, or a gaseous helium atom or the liquid surface itself. The rate constant for bulk recombination in a background gas of helium-4 was calculated by Greben, Thomas and Berlinsky [16]. In this case, the density decays according to

$$dn_H/dt = - K_3\, n_H^2\, n_{He} \tag{1.15}$$

where n_H and n_{He} are the hydrogen and helium densities respectively. The transition to the molecular state is enabled by the exchange interaction. The process is sometimes referred to as Van der Waals recombination, due to the interaction with the third body.

Both the Van der Waals interaction with the third body and the exchange interaction between the recombining atoms conserve the total spin of the electrons S and the total nuclear spin I. As a consequence, all spin dependence may be factorized out of the matrix elements in the expression for the rate constant. A rather simplistic picture turns therefore out to be substantially correct: the probability to recombine for two colliding atoms in the presence of an appropriate third body is simply related to the singlet character mixed into the electronic spin pair wavefunction. It is therefore relatively easy to derive the magnetic field dependence for this process, without going into the details of a full quantum mechanical three-body

h_2h_1		ba	ca	da		cb	db		dc						
h_1h_2	aa	ab	ac	ad	bb	bc	bd	cc	cd	dd	S	M_S	I	M_I	P
	$\varepsilon\eta$		$\frac{1}{2}(\eta^2-\varepsilon^2)$				$\frac{1}{2}$	$-\varepsilon\eta$			*0	0	0	0	+
				$\mp\alpha\eta$					$\pm\alpha\varepsilon$		0	0	1	1	−
			$\mp\frac{1}{2}$				$\pm\frac{1}{2}$				0	0	1	0	−
		$\mp\alpha\varepsilon$				$\mp\alpha\eta$					0	0	1	−	−
				$\pm\alpha\varepsilon$					$\pm\alpha\eta$		1	1	0	0	−
										1	*1	1	1	1	+
				$\alpha\varepsilon$					$\alpha\eta$		*1	1	1	0	+
	ε^2		$\varepsilon\eta$					η^2			*1	1	1	−	+
			$\pm\frac{1}{2}$				$\pm\frac{1}{2}$				1	0	0	0	−
				$-\alpha\eta$					$\alpha\varepsilon$		*1	0	1	1	+
	$-\varepsilon\eta$		$-\frac{1}{2}(\eta^2-\varepsilon^2)$				$\frac{1}{2}$	$\varepsilon\eta$			*1	0	1	0	+
		$\alpha\varepsilon$				$\alpha\eta$					*1	0	1	−	+
		$\pm\alpha\eta$				$\mp\alpha\varepsilon$					1	−	0	0	−
	η^2		$-\varepsilon\eta$					ε^2			*1	−	1	1	+
		$-\alpha\eta$				$\alpha\varepsilon$					*1	−	1	0	+
					1						*1	−	1	−	+

Table 1.1 Decomposition of hyperfine pair states of hydrogen with respect to the total spin representation \S M_S I M_I> (after Silvera and Walraven [1]).

approach. One merely has to decompose the hyperfine pair states with respect to a convenient basis, in which both S and I are specified. The decomposition of the pair states with respect to the total spin basis $|S\ M_S\ I\ M_I\rangle$ is worked out in table 1.1. The $|0\ 0\ 0\ 0\rangle$ and $|0\ 0\ 1\ {-1}\rangle$ states correspond to para-H_2 and ortho-H_2 respectively. The contributions of the various pairs to the rate may be expressed via the field dependent factors f_0 and f_1:

$$f_0(\theta) = \tfrac{1}{4}\ [(n_a^2 + n_c^2)\ \sin^2(2\theta) + 2n_a n_c \cos^2(2\theta) + 2n_b n_d] \tag{1.16a}$$

$$f_1(\theta) = \sin^2\theta(n_a n_b + n_c n_d) + \cos^2\theta(n_a n_d + n_b n_c) + \tfrac{1}{2}(n_a n_c + n_b n_d) \tag{1.16b}$$

where n_a, n_b, n_c and n_d denote the fractional populations of the hyperfine states. The recombination rate to the para state is proportional to f_0, and the ortho rate is proportional to f_1. We will discuss the characteristics of the process with the aid of the above expressions.

In zero field with equal occupation of the four hyperfine states ($n_a = n_b = n_c = n_d = \tfrac{1}{4}$) equations 1.16 a and b lead to $f_0 = 1/16$ and $f_1 = 3/16$. In a strong field the process has the following features. In the case of equal population of the lower hyperfine states ($n_a = n_b = 1/2$) the expressions for f_0 and f_1 lead to $f_0 = f_1 \simeq \tfrac{1}{2}\epsilon^2$. Thus, the application of a strong field will suppress the rate by a factor $1/(2\epsilon^2)$, which amounts 10^5 in a 10 Tesla field. Furthermore, the rate will be proportional to $1/B^2$, which may be verified experimentally. A collision between two $|b\rangle$ or two $|d\rangle$ state atoms cannot lead to the formation of a molecule. This is of particular importance if the sample contains only atoms in the lower hyperfine states. In a 50/50 mixture of $|a\rangle$ and $|b\rangle$, 75 % of the rate depletes the $|a\rangle$ state. Thus, in the absence of relaxation, all $|a\rangle$ state atoms will eventually be lost, leaving a gas of only $|b\rangle$ state atoms, which is doubly polarized with regard to both electron and nuclear spin and completely stable. In practice, a small $|a\rangle$ density will always exist due to dipolar relaxation, and the sample density will decay at a reduced rate. This relaxation bottleneck was predicted by Statt and Berlinsky [17], and later confirmed by experiments[26,27].

The surface analog of the above recombination process was never studied theoretically. However, as pointed out by Silvera and Walraven [1], the two-dimensional process and the bulk process have a lot in common. The interaction with the third body is still of a nonmagnetic nature. Thus, the arguments we used before to derive the magnetic field dependence, also apply to the surface process. In default of a detailed theoretical description, we use a simple two-dimensional gas kinetic model to analyse the experimental data. The collision frequency $\dot{N}$ in a two-dimensional gas of disks with a radius δ_0 is given by

$$\dot{N} = \surd 2\ \bar{v}_2\ \delta_0\ n_s^2 \tag{1.17}$$

where $\bar{v}_2 = (\pi k_B T/2m)^{\frac{1}{2}}$ is the average velocity of the disks and n_s the density. The crosslength $2\delta_0$ is the two-dimensional analog of a cross-section. In equation (1.17) it has been assumed that the cross-length is the same for a-a and a-b collisions. The decay is of second order in the hydrogen surface density with a rate constant K_s given by

$$K_s = 2\surd 2\ f(B)\ \delta_0\ \bar{v}_2 \tag{1.18}$$

where $f(B) = f_0 + f_1$ is the field dependent probability that the collision leads to the formation of a molecule. The loss of two atoms per recombination event results in a factor two in the expression for K_s. It has been assumed that there is always a third body in the form of a helium atom present if two atoms approach within a distance $2\delta_0$.

The currently observed maximum density in the gas is of order 10^{18}/cc [24]. In this density regime the direct three body process with a hydrogen atom as the third body becomes dominant. As a result of the interplay between various relaxation and recombination phenomena, this process involves three |b> atoms. The dipolar interaction with the third atom introduces singlet character in the interaction between the recombining atoms. We will not discuss this process in detail, as the high density regime falls outside the scope of this thesis.

1.3.2 Relaxation

Spin-exchange scattering of hydrogen atoms is the dominant relaxation process in low magnetic fields. Low-temperature spin-exchange cross sections were calculated by Berlinsky and Shizgal [20], and Morrow and Berlinsky [21], finding a value of about 1 Å^2. The field dependence of exchange depolarization was studied by Kagan, Vartanyantz and Shlyapnikov[13]. To find the channels which contribute to the process and their field dependence, we may follow the same line of reasoning as in the case of Van der Waals recombination. The allowed channels all involve a single or double electron spin flip. In strong fields the dominant rates vanish as $\epsilon^2 \sim 1/B^2$, and the process is inelastic due to the difference in the initial and final state Zeeman energies. The rates are therefore further surpressed by exponential factors of the form exp $[2\mu_B B/k_B T]$. An exception to these rules forms the ac→bd or bd→ac channel, which is independent of field and elastic, and has a very large rate constant. Normally however, the process is unimportant at strong fields, as the upper hyperfine states are completely empty. The process is of importance in the case of ESR experiments, where a small non-equilibrium population of the |c> or |d> state is created. This point will be worked out in detail in chapter 4.

In strong fields, in an almost pure |b> gas, the rate is bottlenecked by relaxation due to magnetic dipolar forces. Relaxation results either from pair collisions or from the interaction with magnetic impurities at the walls of the sample container [25].

Impurity relaxation gives rise to a first order decay, and may be rendered unimportant by cleaning the cell of magnetic impurities or coating the interior of the cell with solid H_2 in combination with a thick superfluid helium film. The process was investigated by Statt et al. [22,23], who interpreted their experimental results with a model, predicting an exponential dependence on coating thickness.

Two-body dipolar nuclear relaxation has been widely studied, as it is of critical importance for the stability of the gas. It is only important if the cell is clean of magnetic impurities, a condition never met in the course of this thesis work. The surface variant of this process has been a source of confusion for several years, as there was a factor 50 discrepancy between the observed [26,27] and theoretically predicted rates. Re-analysis of the observed rates[24,25] and an ESR study [34] then revealed that the observed decay was due to a surface three body recombination process.

At high temperatures or low fields, the upper hyperfine states may be thermally populated by electronic dipolar relaxation via two-body collisions. The rate constant for this process grows exponentially with $(\mu_B B/k_B T)$ as to be expected for a thermally activated process involving a single electronic spin flip.

1.3.3 Thermal escape

The sample chamber used for the experiments described in this thesis is placed in the center of a superconducting magnet. Due to fringe field effects, atoms in the |a> and |b> hyperfine states are driven to the field center by a force of the form

$$F = -\mu_B \, \partial B/\partial z \qquad (1.19)$$

where μ_B is the magnetic moment of the atom and $\partial B/\partial z$ is the field gradient along the field axis. The density distribution may be found by evaluating the grand-canonical sum over states, assuming a uniform chemical potential. In the low density regime, where interactions between the atoms may be neglected, this leads to a density distribution of the form:

$$n(z) = n(0) \exp\, [\mu_B(B(z) - B(0))/(k_BT)] \qquad (1.20)$$

where z is the coordinate along the field axis and z = 0 corresponds to the field center. In practice, our sample chamber is an open ended system. The tail of the density distribution may then extend into a zone of the filling tube, where no protective helium coating exist and where the field is almost zero. Atoms with sufficient velocity in the proper direction may escape from the center of the field to this zone in a single shot, and recombine immediately. The system will therefore behave as a volume V, connected via a tube to a perfect vacuum located at $z > z_d$, where z_d corresponds to the point where the zone, unprotected by a helium coverage starts. Hence, even in the absence of recombination within the sample container, the density will decay according to a first order process:

$$dn/dt = -n/\tau \qquad (1.21)$$

with a decay time $\tau = 4\ C_MV/K\bar{v}A$ where V is the volume of the sample chamber, $C_M = \exp[\mu_B(B(z_d) - B(0))/(k_BT)]$ is the magnetic compression factor, K the Clausing factor and A the cross-sectional area of the tube. For a typical geometry this leads to a time constant of about 100 seconds. Much longer time constants were observed in the first successful attempt to stabilize a sample of H↓ [5] and a following systematic study of thermal escape [19]. The difference was attributed to refluxing helium vapor in the filling tube, retarding the motion of the escaping atoms. This effect may be incorporated by including an additional compression factor C_{He} in the expression for the time constant, which has a value of about 80. In view of the recent results of Berkhout et al. [33], who observed substantial probabilities for specular wall reflection, the compression efficiency of the He-vapour should be even higher than originally estimated.

1.4 Rate equations

The decay of the densities of the four hyperfine states is governed by a set of four non-linear coupled first order differential equations. The upper hyperfine states are only occupied at high temperatures or low fields, or if a non equilibrium population of the upper states is created by resonant microwave radiation. Often these upper states may be completely neglected, leaving a set of two coupled differential equations.

Before we discuss the form of these equations for some important cases, we first introduce the use of effective quantities such as effective area and volume, and effective surface rate. Both the volume and the adsorbed phase contribute to the decay. As the densities in both phases are linked together by the adsorption isotherm (1.10), it is possible to specify the surface contributions to the total rate in terms of volume densities. The volume of the sample chamber is large enough that only a very small fraction of the atoms is in the adsorbed phase: $N = n_v V + n_s A \simeq n_v V$ where N is the total number of atoms, V is the volume and A the surface area of the sample container, n_v and n_s are the the volume and the surface densities respectively. For a surface decay process of order r with a rate constant K_s, the volume density decays according to

$$d(N/V)/dt \simeq dn_v/dt = - K_s \ (A/V) \ \lambda_{th}{}^r \exp \left[r \ E_A/k_B T\right] \qquad (1.22)$$

Thus one may translate K_s into an effective surface rate constant K_s^{eff}, given by

$$K_s^{eff} = \frac{A}{V} K_s \lambda_{th}^r \exp[r \ E_A/k_B T] \qquad (1.23)$$

However, for our experimental conditions, the sample distributes itself over an inhomogeneous field region, the density distribution n(z) being given by equation (1.20). To account for this effect both the rate equations and the expressions for the rate constants for the various processes may be modified by replacing n by the central density n(0) and introducing an effective volume V_{eff} and surface area A_{eff}. The density distributes itself over an effective volume V_o, defined by

$$N = V_o\, n(0) \tag{1.24}$$

Integrating the density distribution over the sample chamber yields

$$V_o = \int \frac{dV}{dz} \exp\,[\mu_B(B(z) - B(0))/k_BT]\; dz \tag{1.25}$$

where the real shape of the sample chamber is taken into account via dV/dz. With a surface rate constant K_s an effective area A_{eff} is associated, defined by the relation

$$dN/dt = -A_{eff}\, (n(0))^r K_s \lambda_{th}{}^r \exp[r\, E_A/k_BT] \tag{1.26a}$$

where r is the order of the process and K_s is the rate constant at the central field. Analogously, the effective volume associated with a volume rate constant K_v is defined by

$$dN/dt = -\, V_{eff}\, K_v\, (n(0))^r \tag{1.26b}$$

$$\text{or} \qquad dn(0)/dt = -\, (V_{eff}/V_o)\, K_v\, (n(0))^r \tag{1.26c}$$

Integrating the rates over the volume or surface of the sample chamber yields the following expressions for A_{eff} and V_{eff}:

$$V_{eff} = \int \frac{dV}{dz} \{K_v(B(z))/K_v(B(0))\} \exp\,[r\, \mu_B(B(z) - B(0))/k_BT]\; dz \tag{1.27a}$$

$$A_{eff} = \int \frac{dA}{dz} \{K_s(B(z))/K_s(B(0))\} \exp\,[r\, \mu_B(B(z) - B(0))/k_BT]\; dz \tag{1.27b}$$

Thus, every process has its own definition of A_{eff} or V_{eff}, determined by the temperature, density and field dependence. If the field distribution has a parabolic shape, the variation of A_{eff} and V_{eff} with field or temperature can be substantial [27]. In practice however, the field distribution often has sufficient homogeneity that variations in A_{eff} and V_{eff} are small, typically a few percent.

Note that for some processes the effective volume or surface area may be very large. This is particularly the case if the rate constant contains a magnetic threshold factor of the form $\exp[-2\mu_B B/k_B T]$. If the process is of second order, then the threshold factor and part of the exponential factor in equations (1.27a) and (1.27b) cancel, giving the contributions from the low density tail of the density distribution and the density at the field center equal weights. The above integrals diverge in this case. In practice, this is not a serious problem, since the actual effective area or volume will be bounded due to transport of particles from the center of the field to the low field region. The equilibrium density distribution then no longer applies, and a steady state distribution is set up, determined by the various rates, including diffusion and drift in the field gradient. As an accurate estimate of A_{eff} or V_{eff} is difficult in this case, these processes are best studied in a closed geometry.

To terminate this chapter, we discuss the form of the rate equations for the case that the atoms are lost by the direct surface process (see section 1.3.1) and thermal escape. This form is thought to be appropriate for those experiments where $B/T \gg 10$ T/K. Furthermore the densities should be sufficiently low that third-order recombination is unimportant. Using a shorthand notation n for $n_v(0)$, the rate equations are

$$dn_a/dt = -2K_{aa}^{eff} n_a^2 - K_{ab}^{eff} n_a n_b + G_{ab}^{eff} (n_a + n_b)(n_b - n_a) + G_{imp} (n_b - n_a) - n_a/\tau \tag{1.28a}$$

$$dn_b/dt = - K_{ab}^{eff} n_a n_b - G_{ab}^{eff} (n_a + n_b)(n_b - n_a) - G_{imp} (n_b - n_a) - n_b/\tau \tag{1.28b}$$

where K_{aa}^{eff} and K_{ab}^{eff} are the rate constants for recombination via a-a or a-b collisions, G_{ab}^{eff} is the rate constant for dipolar relaxation, either at the surface or in the volume, G_{imp} is the rate constant for relaxation caused by magnetic impurities, and τ is the time constant for thermal escape. The rate equations may be simplified in two extreme cases, fast relaxation and slow relaxation. Fast relaxation, compared to the recombination rate, may result from a large concentration of magnetic impurities at the walls of the sample container. In this case the populations of both hyperfine states are in thermal equilibrium ($n_a = n_b$ for T > 100 mK) and the equations reduce to

$$\frac{dn}{dt} = - (1/2)\ (K_{aa}^{eff} + K_{ab}^{eff})\ n^2 \tag{1.29}$$

If the relaxation is slow ($G_{imp} \simeq 0$), then the gas eventually will become doubly polarized ($n_a/n_b \ll 1$). In this case, the rate is bottlenecked by the dipolar relaxation:

$$\frac{dn}{dt} = - 2\ G_{ab}^{eff}\ n^2 \tag{1.30}$$

This may be verified by requiring d/dt (n_a/n_b) = 0 [25]. More complicated cases will be treated in the experimental chapters.

References

1. I.F. Silvera and J.T.M. Walraven, in "Progress in Low Temperature Physics", Vol. X, D.F. Brewer, ed., North-Holland, Amsterdam (1986).
2. T.J. Greytak and D. Kleppner, in "New Trends in Atomic Physics", North Holland Publ. Co., Amsterdam (1984).
3. W.N. Hardy, M. Morrow, R. Jochemsen, and A.J. Berlinsky, Physica 109 & 110B, 1964 (1982).
4. W. Kolos and L. Wolniewicz, J. Chem. Phys. 49, 404 (1968).
   W. Kolos and L. Wolniewicz, Chem. Phys. Lett. 24, 457 (1974).
   W. Kolos, and L. Wolniewicz, J. Mol. Spectr. 54, 303 (1975).
5. I.F. Silvera and J.T.M. Walraven, Phys. Rev. Lett, 44, 164 (1980).
6. I.F. Silvera, Phys. Rev. B 29, 3899 (1984).
7. R.A. Guyer and M.D. Miller, Phys. Rev. Lett. 42, 1754 (1979).
8. I.B. Mantz and D.O. Edwards, Phys. Rev. B 20, 4518 (1979).
9. C. De Simone and B. Maraviglia, Chem. Phys. Lett. 60, 289 (1979).
10. I.F. Silvera and V.V. Goldman, Phys. Rev. Lett. 45, 915 (1980).
11. D.O. Edwards and I.B. Mantz, J. de Phys. 41, C7-257 (1980).
12. W.C. Stwalley, Phys. Rev. Lett. 37, 1628 (1976).
13. Yu. Kagan, I.A. Vartanyantz and G.V. Shlyapnikov,

Sov. Phys. JETP 54, 590 (1981).

14. M.W. Reynolds, I. Shinkoda, R.W. Cline and W.N. Hardy, Phys. Rev. B 34, 4912 (1986).
15. I. Dabrowski, Can. J. Phys. 62,1639 (1984).
16. J.M. Greben, A.W. Thomas and A.J. Berlinsky, Can. J. Phys, 59, 945, (1981).
17. B.W. Statt and A.J. Berlinsky, Phys. Rev. Lett, 45, 2105 (1980). This effect was originally suggested by W.N. Hardy.
18. J.T.M. Walraven and I.F. Silvera, Phys. Rev. Lett 44, 168 (1980).
19. J.T.M. Walraven, I.F. Silvera, A.P.M. Matthey, Phys. Rev. Lett. 45, 118 (1980).
20. A.J. Berlinsky and B. Shizgal, Can. J. Phys. 58, 881 (1980).
21. M. Morrow and A.J. Berlinsky, Can. J. Phys. 61, 1042 (1983).
22. B.W. Statt, W.N. Hardy, A.J. Berlinsky and E.J. Klein, Journal of Low Temp. Phys. 61, 471 (1985).
23. B.W. Statt, A.J. Berlinsky and W.N. Hardy, Phys. Rev. B 31, 3169 (1985).
24. H.F. Hess, D.A. Bell, G.P. Kochanski, D. Kleppner and T.J. Greytak, Phys. Rev. Lett. 52, 1520 (1984).
25. R. Sprik, J.T.M. Walraven, G.H. van Yperen and I.F. Silvera, Phys. Rev B 34, 6172 (1986).
26. R.W. Cline, T.J. Greytak and D. Kleppner, Phys. Rev. Lett. 47, 1195 (1981).
27. R. Sprik, J.T.M. Walraven, G.H. van Yperen and I.F. Silvera, Phys. Rev. Lett. 49, 153 (1982).
28. W.N. Hardy, M. Morrow, R. Jochemsen, B.W. Statt, P.R. Kubik, R.M. Marsolais, A.J. Berlinsky and A. Landesman, Phys. Rev. Lett. 45, 453 (1980).
29. R.W. Cline, T.J. Greytak, D. Kleppner, and D.A. Smith, J. de Phys. 41, C7-151 (1980).
30. R.P. Feynman, Phys. Rev. 94, 262 (1954).
31. J.Lekner, Philos. Mag. 22, 669 (1970).
32. W.F. Saam, Phys. Rev. A 4, 1278 (1971).
33. J.J. Berkhout, E.J. Wolters, R. van Roijen, J.T.M. Walraven, Phys. Rev. Lett. 57, 2387 (1986).
34. M.W. Reynolds, I. Shinkoda, W.N. Hardy, A.J. Berlinsky, F. Bridges and B.W. Statt, Phys. Rev. B 31, 7503 (1985).

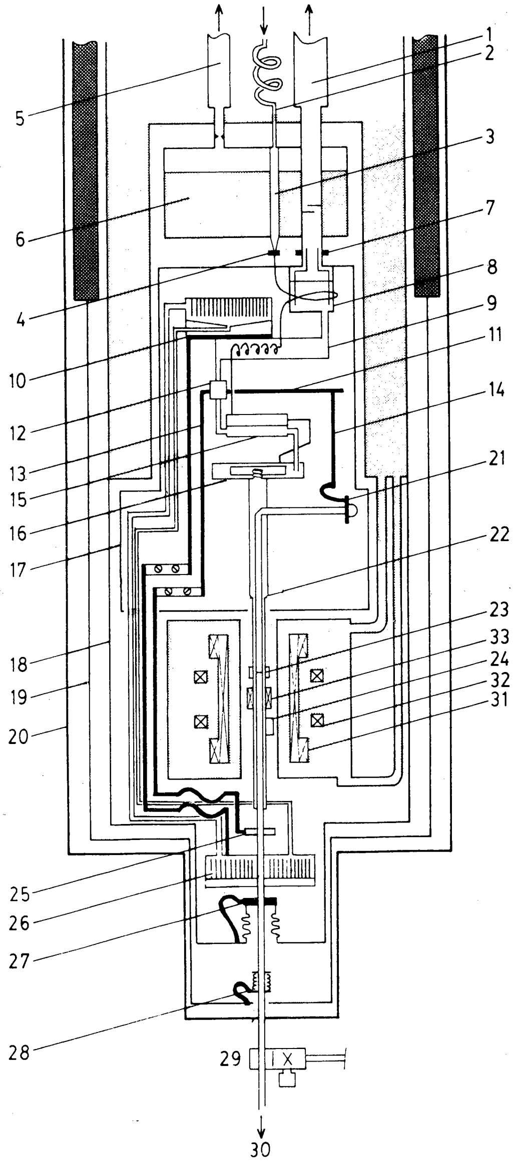

1 ^{3}He pumping tube
2 ^{3}He return line
3 ^{3}He condenser
4 Flow impedance
5 ^{4}He pumping line
6 1.2 Kelvin ^{4}He bath
7 Film burner
8 Still
9 Continuous (spiral) heat exchanger
10 Heatpipe condensor
11 Cold plate
12 Copper sinter
13 Cooling pole for Thermal Platform
14 Cooling pole for far infrared bolometer
15 Discrete heat exchanger
16 Mixing chamber
17 Still temperature radiation shield
18 4.2 K radiation shield
19 77 K radiation shield
20 Outer case
21 FIR bolometer
22 HSC pinning
23 Mylar window
24 Pressure gauge
25 Thermal Platform
26 HEVAC with heatpipe evaporator
27 Accommodator
28 77 K pinning
29 Teflon valve
30 To microwave source
31 7.5 T main coil
32 Quadrupole coils
33 250 G + 50 G coils

CHAPTER II APPARATUS

Stabilization of atomic hydrogen and the study of its properties requires the development of non-standard techniques. Special cooling precautions have to be taken to handle the large amounts of heat, produced by the recombining atoms. Suitable detection schemes, such as pressure measurement, calorimetric detection using bolometers and resonance techniques are useful to measure the density of the gas.

This chapter deals with experimental techniques, with emphasis on those developments that were part of this thesis work. The cryogenic system and stabilization cell are described in section 2.1. The remainder of the chapter is devoted to various detection techniques: pressure measurement (section 2.2), electron spin resonance (section 2.3), bolometric detection (section 2.4) and thermometry (section 2.5).

2.1 Cryogenic system

An overview of the apparatus is shown in figure 2.1. Figure 2.2 shows the Hydrogen Stabilization Cell (HSC) and the fill line in more detail.

The experiments were carried out in a commercial dilution refrigerator (Oxford Instruments). The dilution unit has a maximum cooling capacity of 500 μW at a mixing chamber temperature of 100 mK and a circulation rate of 1000 μmol/sec. The sample cell is adapted to study atomic hydrogen with electron spin resonance, and is the one used by van Yperen et al. [1] with some modifications. In this geometry, the cell is part of a light pipe system, guiding the microwaves. It consists of a copper tube (inner diameter: 5 mm, outer diameter: 9 mm, length: 20 cm), and is vacuum sealed at the top with a mylar window, which is transparant to the microwaves. A heavy copper bar, which surrounds the upper part of the light pipe, transports the heat load on the cell to the mixing chamber. This bar is soldered to the cell with Woods metal. At low temperatures, this joint is superconducting and has a low thermal conductivity. In a field of the order of 100 Gauss it becomes normal and remains in the normal state after the field has been reduced to zero. This hysteresis effect results from the freezing-in of flux. The copper bar is connected to the mixing chamber by a screw contact. This screw contact is

Fig. 2.1 (opposing page) Cryogenic apparatus

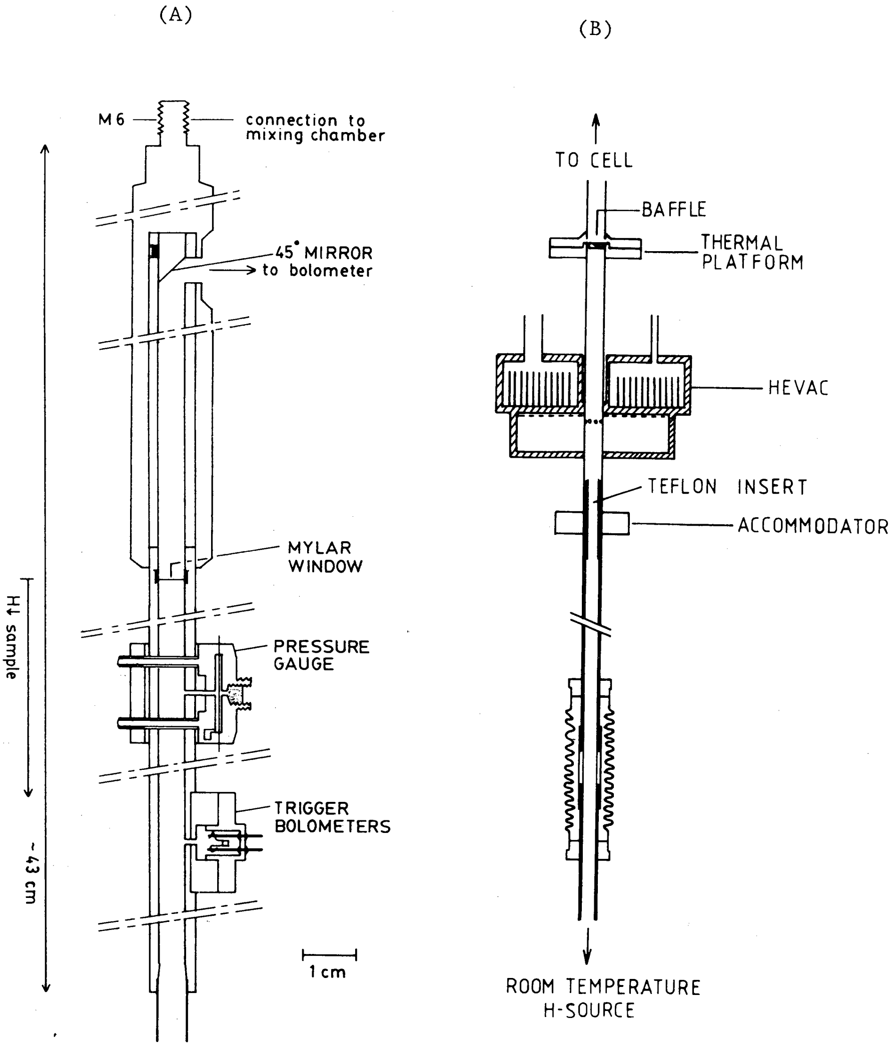

Fig. 2.2 (A) Hydrogen stabilization cell.

(B) Filling system

the weakest link in the thermal connection of the sample container to the mixing chamber. With a heat load on the cell of 40 microwatts, the temperature difference between the liquid inside the mixing chamber and the sample cell was 90 mK (cell temperature: 160 mK).

The cell is mounted inside the bore of a superconducting magnet which produces a maximum field of 7.5 Tesla with a $1:10^5$ homogeneity in a 1 cc volume. A set of sweep coils is placed near the center of the main field. Care was taken to avoid magnetic impurities at the walls of the cell, which cause rapid relaxation of the nuclear spins of the sample of atomic hydrogen. All copper parts were plated with gold to prevent oxidation in air and carefully etched in HCl and HNO_3. Stycast 1266[7] epoxy was used to seal the electrical feedthroughs and the mylar window. The geometry of the cell is such that the German-Silver parts of the filling line are practically in zero field. This prevents first order surface relaxation from taking place in the tail of the density distribution. The sample chamber is provided with a pressure gauge and a set of trigger bolometers[2] to destroy the sample. The microwave radiation is detected with a composite bolometer consisting of a NiCr-plated sapphire sheet with a doped Germanium sensing element.

Atomic hydrogen is produced at room temperature by dissociating H_2 in a microwave discharge. The atoms are allowed to enter the fill line by opening a Teflon valve. To minimize recombination losses in the fill line and the sample chamber, suitible wall materials have to be chosen. A Teflon tube extends from room temperature to the accommodator, where the atoms are cooled down to about 5 Kelvin by wall collisions. Below 1 Kelvin, superfluid helium-4 or a helium-3/helium-4 mixture is used as the coating material. The accommodator is coated with solid hydrogen. More details of the production of cold atomic hydrogen can be found in ref. 3.

The presence of a superfluid helium film in the stabilization cell presents a cryogenic problem. The temperature gradient along the filling line drives the film towards the warmer parts, where it evaporates. The vapor refluxes to the cold parts, where it condenses. This convection mechanism turns the filling line into a heatpipe. The heat load $\dot{Q}$ due to this process is found from:

$$\dot{Q} = \pi \; d \; v_c \; \delta \; L \tag{2.1}$$

d being the tube diameter, v_c the critical velocity of the superfluid film, δ the film thickness and L the heat of condensation per unit volume. The estimated heat load assuming a saturated film of thickness 300 angstrom and a critical velocity of 30 centimeter/second amounts 0.5 milliWatts. Surface roughness may increase this by a factor of four, as is known from beaker flow experiments [4]. To avoid such a heat load on the stabilization cell, the filling line should be pinned at a temperature of about 0.5 Kelvin. At this temperature the helium vapor is effectively condensed. In practice we also use a second thermal pinning point (to which we refer as thermal platform, see fig. 2.1) which normally operates at 300 mK.

The required cooling power for these pinnings is available in the dilution unit. Several milliWatts may be extracted from the still. However, a disadvantage of the still as a heat sink is the fact that it operates at a temperature of 700 mK. Another possibility is the continuous heat exchanger. The dilute stream, flowing from the mixing chamber to the still, represents a much larger enthalpy flow than the condensed stream, flowing in the reverse direction. At a temperature of 500 mK, the enthalpy of the dilute phase H_{3D} (T = 500mK) $\simeq$ 8.5 J/mole [5]. The enthalpy of the condensed phase H_{3C} (T = 500mK) $\simeq$ 1.5 J/mole at this temperature. Thus there is a net cooling term on the still, which is normally wasted by electrical heating, but useful for our purpose. Assuming that both phases have the same temperature (T), a heat input

$$\dot{Q} \simeq \dot{n}_3 \; [H_{3D}(T) - H_3(T)] \tag{2.2}$$

is needed to heat both streams from the mixing chamber temperature to the temperature T, where $\dot{n}_3$ is the circulation rate and the enthalpies of both phases at the mixing chamber temperature have been neglected. In the dilute stream the helium-3 concentration is a function of temperature due to osmotic effects. Therefore the quantity H_{3D} is sometimes referred to as the osmotic enthalpy[5]. From the above relation it follows that at a circulation rate of 300 micromole/second (this corresponds to a normal operating condition for our dilution refrigerator) about 2 mW cooling power may be extracted from the continuous heat exchanger at a temperature of 500 mK, which is appropriate for our purpose.

The thermal platform is connected to the cold plate. This plate is situated between the continuous and first step heat exchanger, and is in contact with the dilute stream through a copper sinter. An off the shelf bar of electrolytic copper (length 50 cm, cross-sectional area 1 cm^2) transports the heat from the thermal platform to the cold plate. To increase the thermal conductivity, the copper has been annealed in a flame.

The major part of the heat load due to the film is absorbed in the HEVAC (he̲lium va̲por c̲ompressor). Apart from condensing the helium vapor, this device also acts as a miniature diffusion pump for the hydrogen atoms. The HEVAC is connected to the continuous heat exchanger at a point about 10 cm apart from the still. Here we are faced to another problem: transporting several milliWatts over a distance of 60 cm, thereby producing a small temperature gradient as possible. In finding a remedy, we were guided by the cause of the problem itself: the heatpiping action of the filling tube of the sample chamber. Thus we utilized a heat pipe, filled with helium-3, transferring the heat load on the HEVAC to the continuous heat exanger. Figure 2.3 shows the HEVAC, the heat pipe and the connection to the continuous heat exchanger in detail. The heat is transported by evaporation at the bottom of the heatpipe and condensation at the top. The difference in vapor pressure between the warm and the cold end drives the gas flow; the liquid, condensed at the top, flows towards the bottom due to gravity. The temperature drop ΔT along a tube of length l, radius a, in case of a heat load $\dot{Q}$, is found from Poiseuille's law:

$$\Delta T/l = 8\ \eta\ R\ T\ \dot{Q}/[\pi\ a^4\ P_{av}\ (dP_v/dT)\ L] \qquad (2.3)$$

where η is the viscosity of the gas, R the gas constant, P_{av} the average pressure, P_v the vapor pressure and L the molar heat of evaporation. For a 5 mm i.d. tube, equation 2.3 leads to a temperature gradient of 4 μK/cm at a temperature of 0.5 Kelvin, and a heat load of 1 mW. A standard quality copper bar of the same dimensions gives 10 mK/cm. Thus the transfer of heat by a gas, carrying its heat of vaporization is much more efficient than the heat transfer by electrons or phonons in a conducting solid. This principle has been widely applied in refrigation technology[6], using cooling agents ranging from liquid hydrogen to liquid sodium. In practice the performance of the heatpipe is limited by the Kapitza resistance at the copper-liquid helium interface. Therefore, if a large heat flux has to be transported over a long distance, a heat pipe should be considered as a possible alternative for a copper bar.

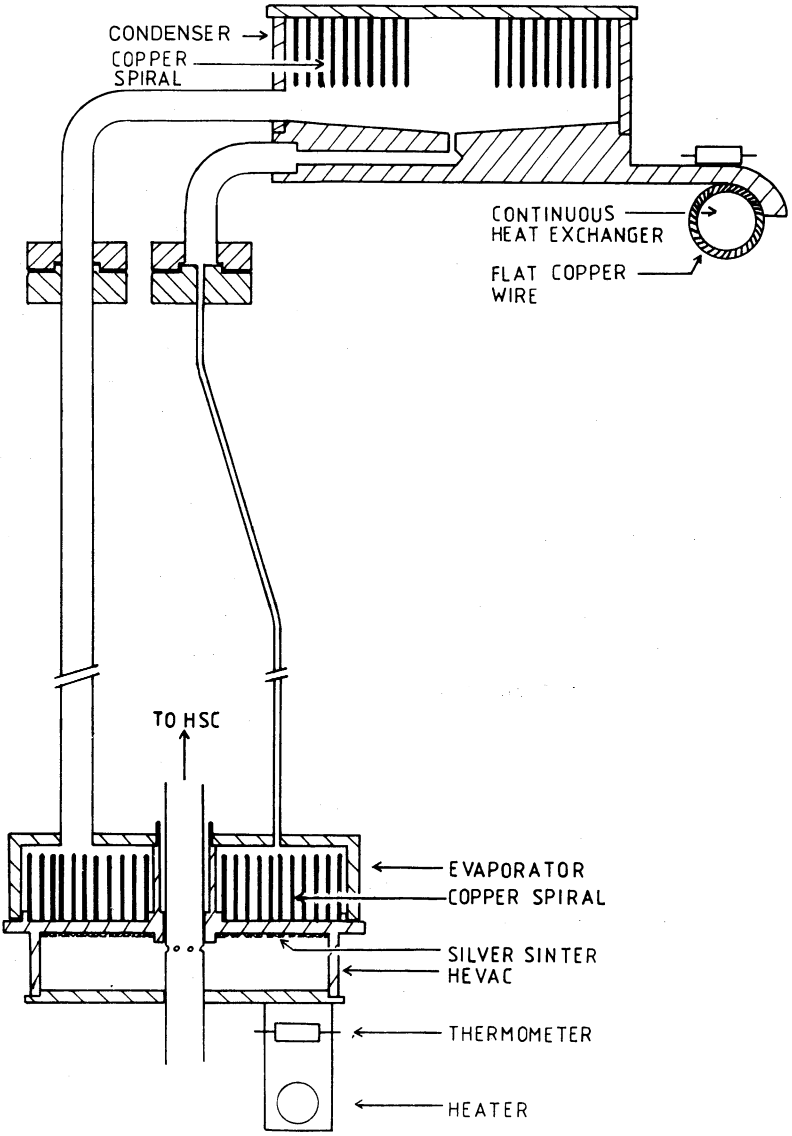

Fig. 2.3 Heatpipe cooling system, transporting the heat load on the HEVAC from condensing vapor in the filling system to the continuous heat exchanger in the dilution unit.

To overcome the Kapitza problem, both the evaporator and the condensor are equiped with a spiralized copper plate, 0.5 mm thick, 15 mm wide and having a length of about 1 m. To enlarge the contact area with the liquid, the surface was deformed mechanically and sandblasted. Both spirals have a geometrical area of 400 cm^2. Larger areas are more easily realized with sinters, however a temperature gradient is set up inside the sinter due to the blocking of convective flow and the poor thermal conductivity of liquid helium-3 and the sinter material in the temperature regime of interest. An analysis of the heat transfer inside the sinter shows that there exists a temperature dependent optimum sinter thickness: for a thin sinter, the heat transfer is limited by the Kapitza resistance, whereas for a thick sinter the thermal conductivity of the liquid and the sinter material is the limiting factor. At a temperature of 500 mK, the estimated optimum thickness amounts 25 microns for a silver sinter, which is impractically thin. Another reason to abandon the use of sinters inside the heatpipe is the possible formation of gas bubbles, particularly at the warm side of the heat pipe.

A Kapitza resistance also exists between the dilute stream and the walls of the continuous heat exchanger, and between the helium and the copper inside the HEVAC. The continuous heat exchanger is a copper-nickel tube, 1 meter long, wound in the form of a spiral. To make contact to this tube, the tube was thermally shorted over a distance of 13 cm by soft soldering flat copper wire around the tube, resulting in a 15 cm^2 effective contact area with the liquid. The copper connection to the condenser, the flat copper wire and the tube of the heat exchanger are soldered together with Woods metal. As the sample chamber and the filling line is normally covered with pure helium-4, a 0.4 mm thick silver sinter was used inside the HEVAC. In this case the temperature gradients inside the sinter are less of a problem.

Test results of the heat pipe are shown in fig. 2.4. Calibrated carbon resistance thermometers were mounted at the HEVAC, the condenser and the continuous heat exchanger. This third thermometer measures the temperature of the dilute stream. The HEVAC is provided with a heater. The estimated circulation rate is 300 micromole/second, which is typical for our experiments. These measurements were carried out with a constant heat input to the still. Therefore, the circulation rate will vary somewhat with the heat, applied to the HEVAC. The estimated heat input by conduction from the accommodator is 800 μW. The horizontal scale of fig. 2.4. is displaced over this amount. At a heat load of about 1 mW the Kapitza resistance between the

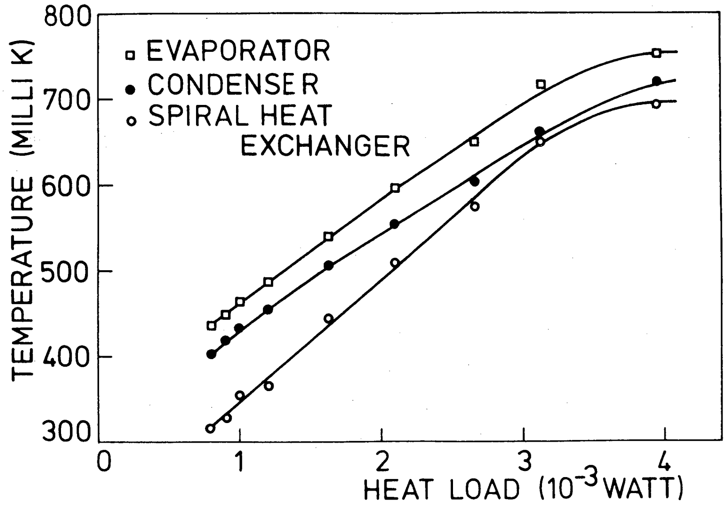

Fig 2.4. Test results of the heatpipe.

dilute stream and the wall of the heat exchanger determines the overall behaviour of the heat pipe; at a heat load of about 4 mW the Kapitza resistance between the copper and the helium-3 dominates.

2.2 Design and construction of the pressure transducer

A measurement of the pressure of atomic hydrogen is the most direct way of demonstrating its gaseous nature. A pressure transducer is an attractive tool to study the density decay with a non-destructive technique. A sensitive diaphragm type pressure transducer has been developed, which operates in a low temperature environment and in strong magnetic fields.

The transducer is shown in fig. 2.5. The pressure difference across the diaphragm results in a displacement from the equilibrium position, which is detected with a capacitive technique. The streched Kapton diaphragm is 0.012 mm thick and gold plated on one side. It is sandwiched between two pieces (1 and 2) of copper. Piece 1 is the fixed capacitor plate, and faces the gold covered surface of the diaphragm. Piece 2 contains the sample and is in contact with the HSC. The diaphragm is glued to the copper pieces with Stycast 1266 epoxy [7]. The sandwiched structure was choosen to provide an overload protection. Stycast 1266 has a good adhesion to both copper and

Kapton. The seal is very strong and superleak-tight if the epoxy is allowed to cure under mechanical pressure. The space between the capacitor plates is in direct contact with the inner vacuum can of the cryostat. A copper sinter in the interconnecting tube prevents dust particles from entering this vacuum chamber. Electrical contact to the diaphragm is made through a gold strip extending from the gold plated central section. To isolate this strip from the central section, a small portion of copper is replaced by Stycast 1266 before the vacuum chamber is machined into the fixed plate.

The displacement of the diaphragm from the equilibrium position can be described with a simple model, where a uniform tension T provides the restoring force. The tension in terms of the relative strain e, the diaphragm thickness t and the Youngs modulus E is given by:

$$T = Eet \qquad (2.4)$$

Balancing the forces on a circular annulus of radius r results in the following differential equation for the displacement u(r):

$$(1/r)\, d/dr\, (r\, du/dr) = -\, p/T \qquad (2.5)$$

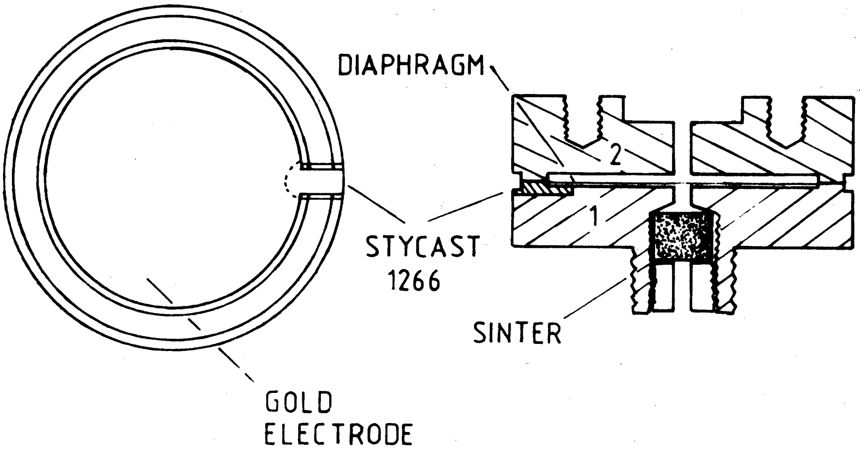

Fig. 2.5. The pressure gauge. Left: the gauge as seen from the top with piece 2 removed, showing the gold pattern on the membrane. Right: cross-sectional view of the gauge

where p is the pressure difference across the diaphragm. Integration of the above equation gives:

$$u(r) = (p/4T)\ (R^2 - r^2) \tag{2.6}$$

where R is the radius of the diaphragm. The capacitance C of the transducer neglecting fringing fields is:

$$C = (4\pi\epsilon_0 T/p)\ \ln[(1 - (pR^2)/(4Td))^{-1}] \tag{2.7}$$

d being the depth of the vacuum chamber. Under normal operating conditions, the non-linearity is unimportant, because in our application the pressure is small ($< 10^{-3}$Torr). However, the sensor is calibrated at pressures of the order of 1 Torr, where non-linearity effects are significant. It follows from a Taylor expansion of equation 2.7 that the reciprocal capacitance is a more linear function of the pressure than the capacitance itself. Thus, for the purpose of calibration, the linear coefficient in the expansion is best obtained from a plot of 1/C versus p. On the other hand, the capacitance bridge, to be described below, measures the value of C; to get an impression of the non-linearities in the pressure reading, C versus p should be plotted.

The sensitivity of the transducer defined as $|(1/C)\ dC/dp|$ follows from eq. (2.7):

$$|(1/C)\ dC/dp| = R^2/(8Eetd) \tag{2.8}$$

Thus the sensitivity can be optimized by maximizing the diaphragm radius and minimizing the strain, thickness of the diaphragm and the depth of the vacuum chamber. The bore of the magnet sets an upper limit to the available space and therefore to the diaphragm radius. A vacuum chamber with a uniform depth of some tens of microns may be realized with standard machining procedures by a skilled instrument maker. The strain is determined by the strain at room temperature and the differential thermal contraction of copper and Kapton between room temperature and low temperature. To make sure that there is no electrical contact between the gold electrode and the fixed plate, the diaphragm is prestressed at room temperature. The estimated strain at low temperatures is about 2 percent.

The transducer is assembled using the construction jig shown in fig. 2.6.

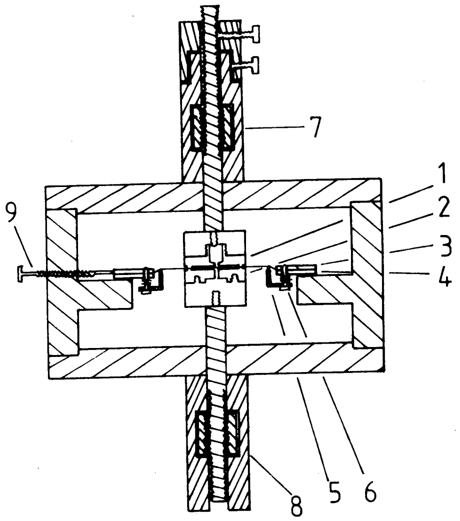

1 Fixed capacitor plate
2 Copper piece 2 with sample space
3 Brass ring
4 Brass ring
5 Membrane stretching brass ring
6 Tightening screws with springs
7 Screw mechanism for normal motion of fixed capacitor plate
8 Screw mechanism for normal motion of piece 2
9 Screw mechanism for lateral motion of membrane with respect to copper housing

Fig. 2.6. Construction jig, used to assemble the pressure gauge.

With this jig, the diaphragm and the copper pieces (1) and (2) can be aligned and brought into contact with each other. It allows for curing under mechanical pressure. Because of its compactness, it can be placed in a small oven, thus allowing for a cure at elevated temperatures. Provisions are made to monitor the capacitance between the fixed plate (1) and the gold electrode during assembly.

The diaphragm is clamped between two flat brass rings (3) and (4); a third ring with a smooth edge (5) together with springs and tightening screws (6) is used to stretch the foil. Before the gold is evaporated, a mask (not shown in the figure) is added and the whole assembly is cleaned ultrasonically in Freon. The evaporation is carried out in a clean vacuum system, to prevent the foil from contaminating with magnetic impurities.

After the fixed plate (1) and the diaphragm are aligned, the fixed plate is temporarily removed to apply the epoxy. Care has to be taken not to allow the vacuum chamber to fill with epoxy. To this end a very small quantity of epoxy is used, just enough to wet the copper surface. The screw mechanism (7-9) is used to bring the fixed plate into contact with the foil in a controllable manner. The same procedure is used to glue the other copper

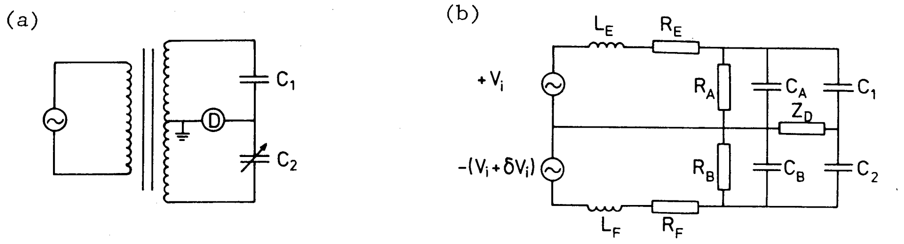

Fig. 2.7. (a) Simplified circuit of transformer bridge. (b) Equivalent circuit of the bridge, showing the parasitic impedances.

piece (2) to the Kapton. Screws (7) and (8) are tightened to apply pressure. The epoxy is cured for 24 h at room temperature and post-cured for a few hours at 60 °C. After the superfluous Kapton is removed, a brass spring is attached to make a clamped electric contact to the gold finger providing the contact with the gold electrode.

The capacitance of the transducer is measured with an equal ratio arm transformer bridge (General Radio, model 1615). A simplified circuit is shown in fig 2.7.a. By connecting the center tap of the secondary windings to ground, most parasitic capacitances that affect the bridge reading are shunted to ground. We use the equivalent circuit [8] of fig. 2.7.b to analyse the errors and the noise performance of the detection electronics. C_1 is the capacitance of the gauge, C_2 the balancing capacitor of the bridge. C_A and C_B represent the total effective capacitances shunting the secondary windings of the transformer, R_A and R_B are their corresponding losses. R_E, R_F, L_E and L_F represent the ohmic losses and the self inductances of the interconnecting cables. Z_D is the total impedance shunting the detector input. A mismatch of the secondary windings is represented by δV_i. The transducer is connected to the bridge terminals with coaxial cables to suppress the influence of the capacitance between the leads, which may vary in time. In the low temperature part of the apparatus we use commercial coaxial cable supplied by Lake Shore Cryotronics, which unfortunately has a large capacitance between the center conductor and the shielding of about 1 nF and a resistance of 10 Ω. These dominate C_A and R_E. A typical value of the self inductance of the leads is 1 μH. The balance condition of the bridge is approximately:

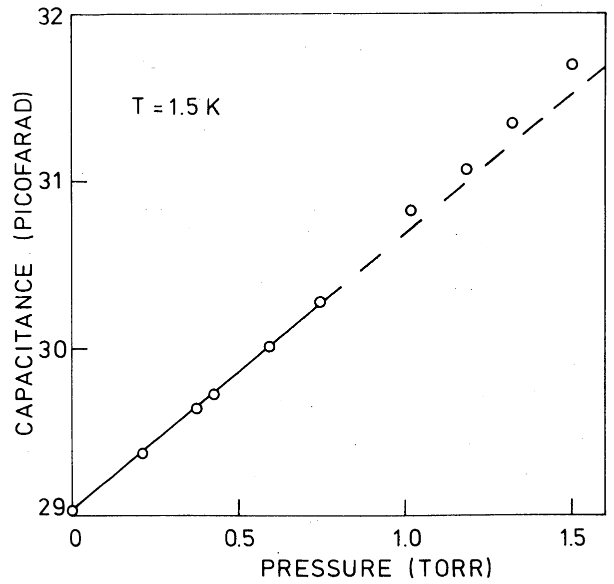

Fig. 2.8. Calibration of the pressure-capacitance relation of the gauge.

$$C_1/C_2 = 1 + \delta V_i/V_i - \omega^2 L_E (C_1 + C_A) + R_E/R_A + \omega^2 L_F (C_2 + C_B) - R_F/R_B \quad (2.9)$$

At a frequency of 1 kHz all terms containing L_E, L_F, R_E or R_F are of the order of 10^{-5}. The sensitivity of the bridge reading to variations in the corresponding components is quite small. The only important component that affects the stability is the balancing capacitor C_2. A good capacitor has a long term stability of 10 ppm, which may be improved by stabilizing its temperature. In principle a low temperature reference capacity provides the best result, but this solution appeared not to be required as we were limited by slow drifts in the pressure gauge.

If the bridge is in balance at zero pressure, the out of balance signal may be used to monitor the pressure. The out of balance signal U_d in terms of the variation ΔC_1 neglecting the parasitic terms is given by:

$$U_D = - V_i \times \Delta C_1/[C_1 + C_2 + (j\omega Z_D)^{-1}] \quad (2.10)$$

The smallest detectable capacitance change is determined by the input noise of the detector amplifier. A common value of the noise figure at 1 kHz and a source resistance of 100 kΩ, which is a typical value of the impedance between the detector terminals, is 0.2dB. The excitation voltage of the bridge is of the order of 10 Volts. This results in a minimum detectable relative capacitance change of $5\text{x}10^{-7}$.

The transducer was calibrated at 1.5 Kelvin with helium gas against a Barocel strain gauge. The results are shown in fig. 2.8. The data are corrected for thermomolecular effects [9]. Below a pressure of 1 Torr a linear relation exists between the capacitance and the pressure. The slope gives a sensitivity of 1.65 pF/Torr. The smallest detectable density at 200 mK is about $1\text{x}10^{14}$/cc.

2.3 ESR Spectrometer

ESR has proved to be a valuable tool to study the decay kinetics of atomic hydrogen. It allows for a determination of the density of both the lower hyperfine states separately. The spectrometer is of a FIR broadband transmission like design. It consists of a long tube, filled with a localized sample. Changes in the transmission due to the presence of the sample are detected by a semiconductor bolometer, which operates at a temperature of 0.5 Kelvin.

A detailed description of the spectrometer and the relevant resonance theory has been given by van Yperen et al [1]. Therefore only a brief discussion of these items will be given here.

In a conventional ESR experiment a linearly polarized oscillating magnetic field is applied, in a direction perpendicular to a static field. The transition rates may be found from a perturbation treatment. In the case of atomic hydrogen, the allowed transversal ESR transitions are between the |a> and |d> state and the |b> and |c> state. If the oscillating field has an amplitude B_1, the transition rates W_{BC} and W_{AD} are given by:

$$W_{AD} = (1/4)\ B_1^2\ (\gamma_e + \epsilon\gamma_p)^2\ \delta(\nu - \nu_{AD}) \qquad (2.11a)$$

$$W_{BC} = (1/4)\ B_1^2\ (\gamma_e - \epsilon\gamma_p)^2\ \delta(\nu - \nu_{BC}) \qquad (2.11b)$$

The resonance conditions are in the high field limit:

$$\nu_{AD} \simeq \ (1/2)\ a/h + g_e\mu_B B/h \tag{2.12a}$$

$$\nu_{BC} \simeq -(1/2)\ a/h + g_e\mu_B B/h \tag{2.12b}$$

In a 5.6 Tesla field the resonance frequency is 157 GHz. The dominant broadening mechanism is due to the spatial inhomogeneity of the static field. The power loss due to the absorption of radiation of resonant atoms in hyperfine state i is expressed via the ratio P_{out}/P_{in}, where P_{out} is the transmitted power and P_{in} the incoming power:

$$P_{out}/P_{in} = \exp\ [-\int dz'\ \alpha(\nu,z')] \tag{2.13}$$

$$\alpha(\nu,z) = (\mu_o/8c)\ (\gamma_\epsilon \pm \epsilon\gamma_p)^2\ \delta(\nu - \nu_i(z))\ h\nu\ n_i(z) \tag{2.14}$$

where ν is the frequency of the radiation, $\nu_i(z)$ and $n_i(z)$ the resonance frequency and the density of the |i>-state atoms. In equation 2.14 the plus sign applies to the |a>-|d> transition and the minus sign to the |b>-|c> transition. Both ν_i and n_i are a function of z via the field profile. It is assumed that there are only longitudinal field gradients present. To a first approximation the absorption as a function of frequency is given by:

$$P_{out}/P_{in} = \exp[\ -(\pi\mu_o/4c)\ (\gamma_e \pm \epsilon\gamma_p)^2\ (h\nu/\gamma_e)\ (dB(z)/dz)^{-1}\ n_i(z)] \tag{2.15}$$

The divergences of this expression at the field extrema may be removed by incorporating the transverse field gradients. From eq. 2.15 it follows that the lineshape reflects all the fine details of the static field profile. At a density of 10^{16}/cc, 10 % of the radiation is absorbed at resonance if the field has an inhomogeneity of 10^{-5} in a 1 cc volume.

The density of the two lower hyperfine states is measured as a function of time by alternately bringing the two states into resonance and monitoring the resonance line. The cell is provided with two coils for this purpose producing a maximum field of 250 and 50 Gauss, respectively. The 250 Gauss coil is used to switch between the hyperfine states by reversing the current; the 50 Gauss coil is used to sweep the field through resonance.

There are two problems associated with this approach:

-The absolute inhomogeneity of the 250 Gauss coil is about four times better than the inhomogeneity of the main field. Reversing the current of this coil

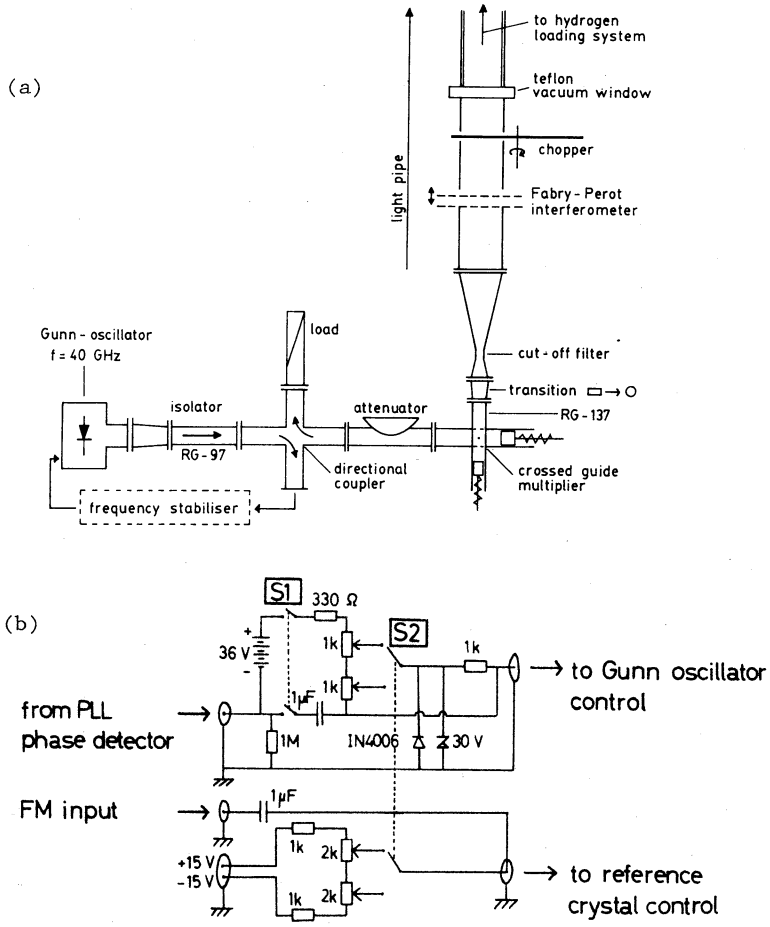

Fig. 2.9. (a) Room temperature part of the ESR spectrometer. (b) Circuit used to switch between different harmonics of the reference crystal of the frequency stabilizer.

results in a slightly different field profile of the combined coils, but this is enough to produce a completely different line shape.

-Because of the finite resistance of the persistent mode switch of the main coil, the field has a drift of 3 Gauss/hour. This drift has to be compensated by the sweep coil, which results in a field pattern and thus a lineshape varying in time, making it hard to calibrate the system.

Part of these problems may be overcome by switching the microwave frequency exactly over 1420 Mhz, the hyperfine frequency. This guarantees

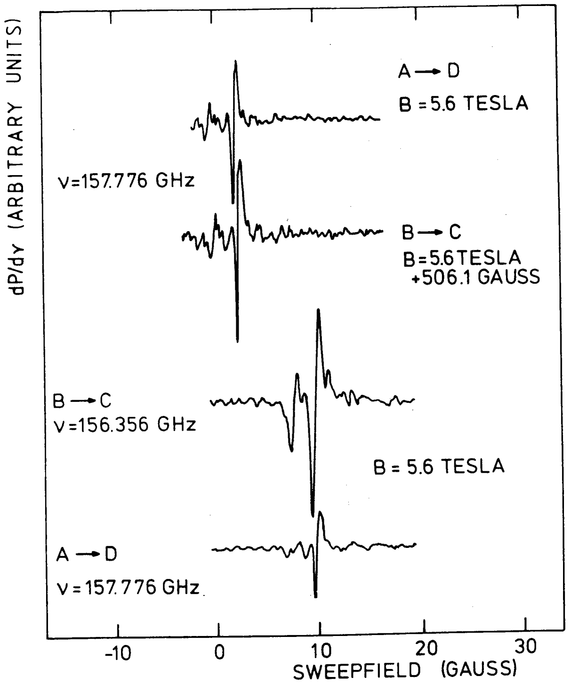

Fig. 2.10. Resonance lineshapes for both transitions at constant frequency (a) and constant field (b), showing that the shapes are field and frequency dependent.

that the field distribution is the same at resonance at both transitions, if the time between the two measurements is short. In the original version of the spectrometer a 1 % frequency deviation was beyond the tuning range. A simple modification of the spectrometer proved to be effective.

The room temperature part of the spectrometer is shown in fig. 2.9a. Microwaves are generated by a Gunn Oscillator, which operates at 39 GHz and is voltage tunable over a range of 1%. Higher harmonics are produced in a crossed guide harmonic generator, with a GaAs Schottky-barrier diode as the nonlinear element. The desired harmonic ($n=4$) is selected by the cut-off of the wave guide and a Fabry-Perot interferometer. A Microwave Systems MOS 3600 frequency stabilizer locks the Gunn Oscillator to a high ($n > 215$) harmonic of an oven stabilized 15 MHz crystal oscillator, which has a tuning range of 0.3%. This crystal oscillator limited the tunability of the spectrometer. The circuit shown in fig. 2.9b overcomes this problem. Normally, the output of the phase detector of the PLL system (MOS APC out) is fed to the Gunn oscillator voltage tuning input. The frequency of the system may be tuned by applying a voltage to the crystal oscillator (MOS Sweep input). The circuit of fig. 2.9.b adds a switch selectable voltage to both the tuning input of the crystal oscillator and the output of the phase detector of the phase locked loop. Thus it allows for jumping between different harmonics of the crystal, keeping the loop in lock. This extends the effective tuning range of the stabilizer by about two orders of magnitude. Frequency modulation is used to employ phase sensitive detection of the derivative of the resonance signal.

Fig. 2.10 shows some typical line shapes. In fig 2.10a the microwave frequency is kept constant and the main field changed over 506 Gauss, to go from the a→b to the b→c transition. This ensures that the field distribution is the same in these two situations. The two lineshapes in fig. 2.10a are the same. In fig. 2.10b the frequency switching technique, described above, is used, the main field is kept constant. Despite the fact that the field distribution should be the same at the two transitions, there is still a marked difference between the two lineshapes. Thus we are led to the conclusion that the microwave frequency plays some role in the lineshape too. A possible explanation is the existence of standing waves, resulting from reflections at irregularities in the sample chamber, such as the entrance of the pressure gauge or the FIR bolometer. The system is calibrated for both transitions at a high temperature, under conditions where the recombination is slow and the relaxation is fast. In this case, both hyperfine levels are equally populated. Comparision of the signals with the pressure gauge provides an absolute calibration for the density of both hyperfine states.

2.4 Trigger Bolometers

A couple of bolometers is mounted inside the HSC to trigger the recombination of the hydrogen atoms. They are used to destroy the sample in the following situations:

- at the end of a measurement of a pressure decay to establish the baseline of the pressure gauge. Thus it is possible to correct for drift in the zero-reading of the gauge.

- by a rapid destruction of the sample, the total number of atoms present in the HSC can be determined with a calorimetric measurement. Furthermore, the current-voltage characeristics contain information about the thickness of the helium film and the presence of helium-3 impurities in the cell. These bolometer applications will be explored below.

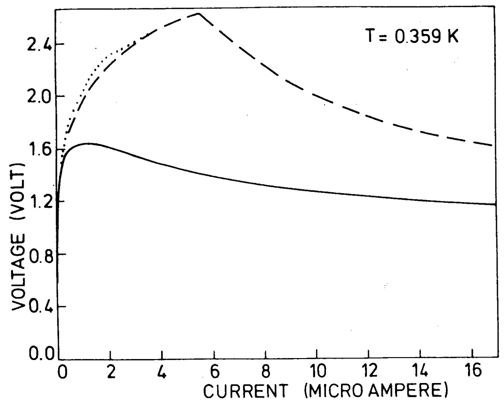

Fig. 2.11 Bolometer current - voltage characteristics. Full curve: bare bolometer. Dashed curve: ^{4}He-covered bolometer. Dotted curve: bolometer covered with a 1 ppm ^{3}He-^{4}He mixture.

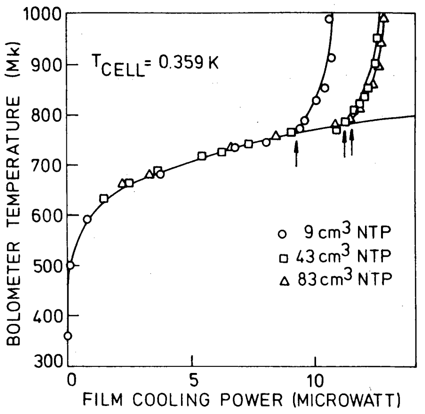

Fig. 2.12 Determination of film critical cooling powers from the bolometer current voltage characteristics. The arrows correspond to the values of P_{crit} at different helium coverages.

The bolometers consist of a small (1 * 0.3 * 0.3 mm^3) piece of resistive material such as carbon or doped Germanium, and a pair of fine copper wires, providing a weak thermal link between the bolometer body and the sample cell.

Fig. 2.11 shows some typical current-voltage characteristics of a germanium bolometer. When helium-4 is introduced in the cell, the curve follows the characteristic of the bare bolometer (i.e. uncovered with helium) at low currents, whereas the maximum is shifted towards a higher current, having a different shape. In the case of a helium covered bolometer, part of the Ohmic heating is carried away by evaporation of helium, which is replenished by superflow along the wires. This extra cooling term is related to the thickness of the helium film. To obtain the film contribution to the cooling of the bolometer, the heat carried by the leads has to be subtracted from the total dissipation. The contribution from the leads follows from the I - V characteristic of the bare bolometer.

The results of this procedure are shown in fig. 2.12 for different amounts of helium in the cell at a cell temperature of 0.359 Kelvin. To relate the bolometer resistance to its temperature, the bolometer was calibrated against the cell thermometer.

Below 0.6 Kelvin, film cooling is ineffective because the helium-4 vapor pressure is too low in this temperature range. The point, where the steep rise at high flow rates sets in corresponds to the maximum in the current-voltage characteristic. At this point the superflow velocity along the wires approaches the critical value. Thus the critical velocity, the circumference of the wires and the film thickness set an upper limit to the cooling power of the film (see also equation 2.1).

A current pulse through the bolometer beyond the maximum in the characteristic triggers a rapid recombination of the hydrogen atoms. This indicates that part of the protecting helium coating disappears from the bolometer if the evaporating helium is not replenished by superflow.

To derive a value of the film thickness from the critical cooling powers (arrows in fig. 2.12), we need to know the critical velocity and the effective circumference of the bolometer leads. The effective circumference of the leads differs from the geometrical circumference due to surface roughness. To calibrate the bolometer as a film thickness detector, the superflow experiments have been repeated at a temperature of 1.3 Kelvin. At this temperature some data on the adsorption of helium-4 on different substrates are available. Thus the film thickness follows from the saturation P/P_o where P is the pressure of the vapor in equilibrium with the adsorbed phase and P_o is the vapor pressure of the bulk liquid. By measuring the critical film cooling power at different saturations P/P_o, the relation between this power and the film thickness may be determined experimentally. We use the adsorption isotherms of Bowers et al. on aluminium [10] and Strauss on jewelers rouge [11] for this purpose. The results are shown in fig. 2.13. The critical power P_{crit} as a function of film thickness d is given by:

$$P_{crit} = 0.9\ (d - d_o) \qquad \text{(microwatt)} \qquad (2.16)$$

d being given in atomic layers, and d_o being number of immobile layers at the substrate, which cannot contribute to the cooling power. Extrapolation of P_{crit} to zero gives a value of 2 for d_o, consistent with other experiments.[15] Below 1 Kelvin, we use a value of 1.5 for d_o.[4]

To check the validity of the above analysis, we calculate the film thickness as a function of the amount of helium, introduced in the cell. A

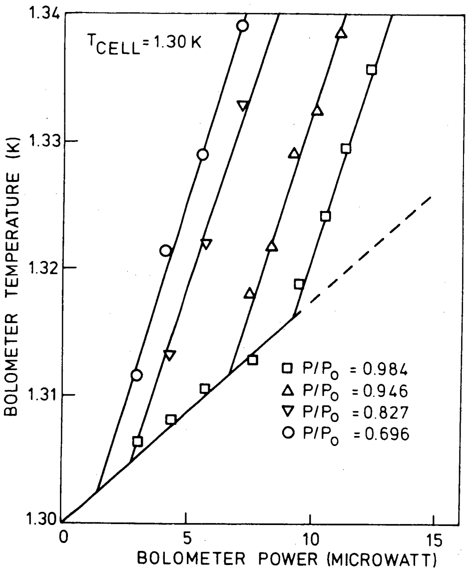

Fig. 2.13. Bolometer response at different saturations P/P_0.

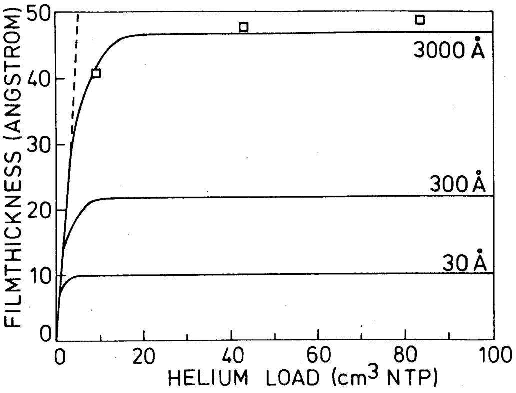

Fig. 2.14. Comparison of film thicknesses as determined from the bolometer response (points) and calculated values for various sinter pore sizes (curves).

complicating factor is the presence of a silver sinter in the HEVAC. We model the system as a completely flat surface (i.e. the walls of the cell) and a large rough surface, having many dimples of characteristic radius r (the sinter). The value of r is associated with the sinter pore size. The film distribution in this system is governed by gravitational, Van der Waals, and capillary forces.

If both the flat and the rough surface are at a height h above the surface of the bulk liquid, the chemical potentials at the two film-gas interfaces are given by

$$\mu_{flat} = \mu_o + mgh - V(d_{flat}) \tag{2.17a}$$

$$\mu_{sinter} = \mu_o + mgh - V(d_{sinter}) - m\gamma/\rho r \tag{2.17b}$$

where μ_o is the chemical potential of the liquid, m is the helium atomic mass, g is the gravitational acceleration, V(d) is the Van der Waals potential at a distance d from the substrate, γ is the surface tension and ρ the density of the liquid. The additional surface tension term arises from the decrease in surface free energy. Because the chemical potential is constant through the system, the film thicknesses follow from

$$mgh - V(d_{flat}) = 0 \tag{2.18a}$$

$$mgh - V(d_{sinter}) - m\gamma/\rho r = 0 \tag{2.18b}$$

For the Van der Waals potential we use the calculations of Anderson and Sabisky [12]; we approximate their result by

$$V(d) = \alpha d^{-3} \tag{2.19}$$

with α = 25 Kelvin (layers)^3 as the appropriate Van der Waals constant for a gold surface.

Both film thicknesses may be calculated with the help of eqs (2.18 a) and (2.18 b), for different values of h and r. The total amount of helium in the system follows then from the film thickness in the sinter and the surface area of the sinter. A detailed study of submicron silver sinters has been made by Robertson er al [13]. Our sinter is estimated to have a pore size of about 0.5 micron and a total surface area of 1 m^2. The model described here is valid for undersaturated films; near saturation the shape of the liquid surface becomes strongly dependent upon the amount of helium in the system.

Figure 2.14 shows the results of the calculations for three values of the sinter pore size, together with the results obtained from the bolometer current-voltage characteristics. At low coverages the film distribution is completely determined by Van der Waals forces. When more helium is introduced in the system, the sinter becomes filled with bulk liquid whereas the film thickness on the flat surface saturates at a value determined by the pore size. This continues until the sinter is almost completely filled and our simple model breaks down. The sinter is completely filled if about 30 cm^3 NTP helium is loaded in the system, so we are safely below saturation. The bolometer results are quite well described by this model if we use a sinter pore diameter of .3 micron. Note that the calculated thickness is rather insensitive to the choice of the relevant parameters (pore size, Van der Waals constant) because of the form of the Van der Waals potential. Thus we may have some confidence in the bolometer results.

Addition of a small quantity of ^{3}He has a marked effect on the shape of

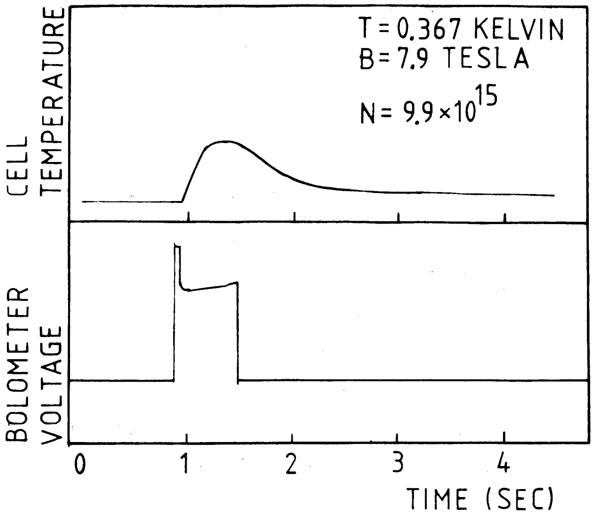

Fig. 2.15. Destruction of hydrogen atoms by a bolometer current pulse. Lower trace: bolometer voltage response. The steep drop in the bolometer voltage marks the evaporation of the film on the bolometer and the onset of recombination. Upper trace: cell temperature response. Reproducing this trace by a current pulse in the cell heater gives the total number of atoms in the cell.

the current-voltage characteristic. A gradient in the ^{3}He concentration, arising from evaporation on the bolometer body, drives the helium-3 along the wires. This results in a cooling effect, known as the heat flush effect [16]. A 1 ppm ^{3}He impurity may be easily observed in the form of a shoulder on the bolometer current-voltage characteristic at low currents (dotted line in fig. 2.11). Thus the bolometer may be used to check the purity of the helium-4, or to signal the presence of a leak.

The recombination of two hydrogen atoms results in the release of an energy of E/k_B = 52,000 K. Figure 2.15 illustrates how this effect allows for a destructive determination of the total number of atoms present in the cell. In the figure the temperature response of the cell after triggering is shown. This trace is easily converted into a recombination energy by reproducing the wave form electronically with the cell heater. Very low densities, of the order 10^8 - 10^9/cm^3 may be detected if the bolometer is used both as a trigger device and as a temperature sensing element. A high sensitivity can be obtained if the flow impedance of the gas to the element is low, to destroy the gas in a short period of time, of the order of 10 milliseconds.

2.5 Thermometry

Several 200 Ω 1/8 W Matsushita [14] resistors were mounted in the cryostat to monitor temperatures below 1 Kelvin. The resistance was measured using a bridge circuit described by Van Yperen et al.[1]. The following standards were used to calibrate the thermometers:

- a NBS SRM 768 superconducting fixed points device for temperatures below 200 mK.
- in situ helium-3 vapor pressure thermometry, with the pressure gauge described in section 2.2, in the range 200 - 600 mK. The 1962 ^{3}He vapor pressure scale was used[16].
- a calibrated Germanium resistor (Lake Shore Cryotronics) in the range 600 mK - 1000 mK.

The vapor pressure may be used to calibrate the thermometer in a nonzero magnetic field. The magnetoresistance was measured to obtain a field dependent calibration below 200 mK. The calibration of the cell thermometer was always repeated after cycling to room temperature. We believe that our thermometry has an accuracy better than 3 milliKelvin below 300 mK, and 5 milliKelvin between 300 and 600 mK.

References

1. G.H. van Yperen, J.T.M. Walraven, I.F. Silvera, Phys. Rev. B30, 2386 (1984).
G.H. van Yperen, Thesis, University of Amsterdam (1984).
2. I.F. Silvera, J.T.M. Walraven, Phys. Rev. Lett. 44, 164 (1980).
3. J.T.M. Walraven, I.F. Silvera, Rev. Sci. Instr. 53, 1167 (1982).
4. For a recent review about helium films, see *The Physics of Liquid and Solid Helium*, vol. II, K.H. Benneman and J.B. Ketterson eds., Wiley-Interscience (1976).
5. O.V. Lounasmaa, *Experimental Principles and Methods below 1 K*, Academic Press (New York, 1974).
6. P. Dunn and D.A. Treay, *Heat Pipes*, Pergamon Press, Oxford 1978.
7. Emerson and Cuming Inc., Nijverheidsstraat 24,

B-2431 Oevel, België.

8. A.M. Thompson, Trans. Inst. Radio Engrs. 7, 245 (1958).
9. T.R. Roberts and S.G. Sydoriak, Phys. Rev. 102, 304 (1956).
10. R. Bowers, Phil. Mag. 44, 485 (1953).
11. Strauss, Thesis, University of Chicago (1952).
12. E.S. Sabisky and C.H. Anderson, Phys. Rev. A7, 790 (1973).
13. R.J. Robertson, F. Guillon and J.P. Harrison, Can. J. Phys. 61, 164 (1983).
14. Sinhachiro Saito and Takashi Sato, Rev. Sci. Instr. 46, 1226 (1975).
15. E. Long and L. Meyer, Phys. Rev. 98, 6, 1616 (1955).
16. D.S. Betts, *Refrigeration and Thermometry below one Kelvin*, Sussex University Press, 1976.

CHAPTER III EXPERIMENTAL MEASUREMENTS

The results, described in this chapter, were obtained in two series of experiments. The motivation of the first series (section 3.1), was to rigorously demonstrate the gaseous nature of atomic hydrogen and the feasibility of pressure measurement in the study of decay processes. The second series was devoted to the same type of experiments in an extended temperature and field range and a better defined geometry (section 3.2) and some studies using a combination of pressure measurement and electron-spin resonance. Section 3.3 covers the heat transfer between the gas and the walls of the sample container; a search for the existence of spin waves is described in section 3.4. ESR pumping experiments are covered in detail in chapter 4.

3.1 Pressure measurement of atomic hydrogen[1]

The first stable samples of atomic hydrogen immediately established the feasibility of pressure studies using a capacitive tranducer. Deflections of a flexible membrane due to applied pressure down to a fraction of an angström may be observed experimentally, and correspond to a detection limit of $\simeq 10^{-6}$ Torr. This corresponds to a density of $3\text{x}10^{13}$ cm^{-3} at a temperature of 300 milliKelvin. Most of our experiments are carried out at densities of 10^{15}-10^{16} cm^{-3}. Non-linearities in the pressure response are neglible up to a pressure of about 1 Torr. The capacitive transducer has become a common detector in atomic hydrogen research due to its sensitivity, accuracy and convenience of operation.

In this section we present the results of the first experimental study of atomic hydrogen using a strain gauge. Pressure measurement was used to demonstrate the gaseous nature of atomic hydrogen at low temperatures, and to study the temperature and field dependence of the surface recombination rate. We give a brief description of the apparatus, used for our first pressure measurements and emphasize the differences with the system described in chapter II.

3.1.1 Apparatus

The first measurements with the pressure gauge were carried out in the

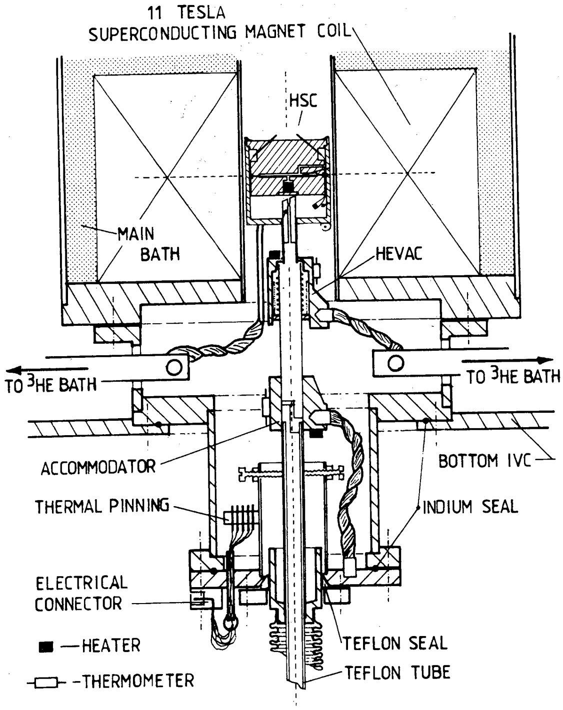

Fig. 3.1 Experimental system, showing the filling line and the sample chamber with the pressure gauge.

same cryogenic system where the early observations of atomic hydrogen were made; only the sample chamber was replaced. In this system both the sample chamber and the HEVAC were pinned to separate helium-3 evaporation coolers. The total running time was limited to about two hours, the lowest attainable temperature being 270 mK. The low temperature part of the apparatus is shown in fig. 3.1.

The sample container is positioned in the center of an 11 Tesla superconducting coil of low homogeneity. The pressure gauge, shown in fig. 3.2, is an integral part of the sample container. In this design, the sample fills the space between the fixed plate and the flexible membrane of the capacitive transducer. This makes the sensor sensitive to variations in the helium film thickness. In later designs, this problem was avoided by measuring the deflection of the membrane across the vacuum reference side of the gauge. The measured sensitivity of this manometer was 11.1 pF/Torr and

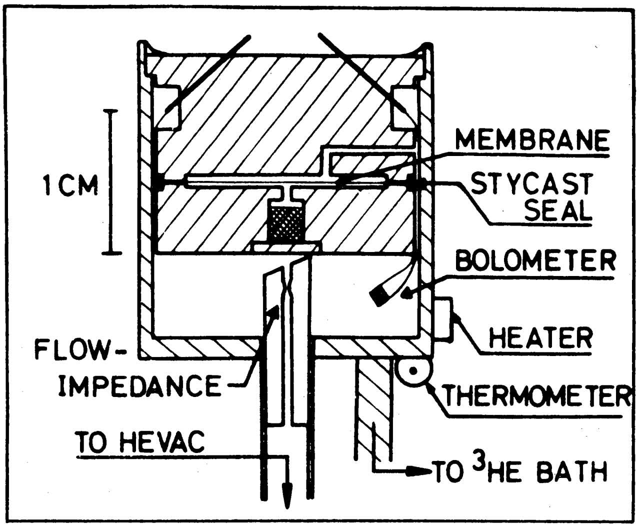

Fig. 3.2 Sample chamber with pressure gauge.

the minimum relative capacitance change was 1.7x10^{-7}, corresponding to a pressure of 10^{-6} Torr.

A valve was mounted in the filling line near the entrance of the sample chamber, to close the cell at the bottom. The valve could be operated from outside the cryostat using a spring mechanism and a nylon thread along the axis of the filling tube. The valve was necessary because in this system with its short filling tube the atoms may escape from the cell and penetrate the H_2 coated zone in a single shot. This process, thermal escape (see section 1.3), was studied in an earlier experiment in the same system[3]. A typical value for the time constant τ of 2000 seconds in an 8 Tesla field was observed. It was not possible, to close the valve completely, as a small leak remained. As such, the valve was effective as a controllable flow impedance.

The cell temperature was measured with a 270 Ohm Speer resistor, which was calibrated against a Germanium thermometer. A bolometer was used to trigger the recombination of the atoms. With this system, the total number of atoms, present in the cell, could be determined with the calorimetric technique, described in chapter 2.

No precautions were taken to keep the sample chamber free from magnetic impurities. At the time the system was prepared for the measurements, we were unaware of the relaxation limited recombination process [40].

3.1.2 Equation of state

The relation between the pressure and the density for a weakly interacting gas of boson particles is given by[4]

$$p = nk_BT + 4\pi\hbar^2 an^2/m \qquad (3.1)$$

where a is the hard core radius. A value, representative for atomic hydrogen a = 0.72 Angström was calculated by Friend and Etters[5]. Under typical conditions ($n = 10^{16}$ cm^{-3}, T = 300 mK) the relative contribution to the pressure due to the interactions is of order 10^{-5}, and ideal gas behavior is therefore expected.

A linear relationship between the pressure and the total number of atoms, determined by the calorimetric method, could be established by a simultaneous measurement of these quantities. The results are shown in fig. 3.3. A systematic deviation from the ideal gas law of 25 % is believed to result from uncertainties in the cell volume; we also believe that after triggering, part of the hot molecules are blown out of the cell without releasing their full recombination energy. Thus the values for the total number of atoms in

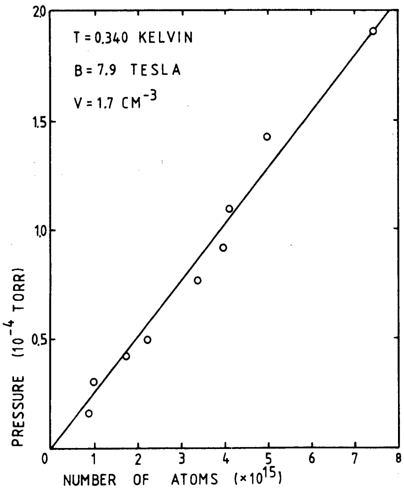

Fig. 3.3 Relation between the pressure and the total number of atoms in the cell.

the cell are a lower bound. The data of fig. 3.3 provide the first direct evidence that atomic hydrogen is a gas at low temperatures.

3.1.3. Surface recombination rate

Under conditions, typical for this experiment, recombination takes place at the walls of the sample container. The temperature dependence of the rate constant is mainly determined by the temperature dependent surface coverage. Although second order surface recombination is extensively studied in experiments no detailed theory is available in the literature. We therefore use the simple kinetic model, described in section 1.4, to analyse the experimental data.

By studying the temporal behavior of the gas density as a function of temperature, the surface binding energy of H on ^{4}He could be determined. This method was successfully applied to the case of atomic deuterium adsorption on helium-4 by Silvera and Walraven[2]. In the limit of fast relaxation and equal populations of the lower hyperfine states, the only loss terms are due to recombination and thermal escape, and the total density decays according to

$$dn/dt = -K_s^{eff}\, n^2 - n/\tau + \varphi/V_o \qquad (3.2)$$

where we also included a term due to the filling flux φ; V_o is the effective volume of the density distribution (see eq. 1.25). The terms third order in the density, we found to be small. This is confirmed by later experiments[6,7]. The effective surface recombination rate constant is given by

$$K_s^{eff} = (1/2)\ (A_{eff}/V_o)\ (K_s^{aa} + K_s^{ab})\ \lambda_{th}{}^2\ \exp[2E_A/k_BT] \qquad (3.3)$$

where K_s^{aa} and K_s^{ab} are the surface rate constants for a-a and a-b recombination respectively. The solution of the differential equation (3.2) in terms of the pressure p(t) is given by ($\varphi = 0$):

$$p(t) = p(0)\ \exp(t/\tau)\ \{1 + [p(0)\ K_s^{eff}\ \tau\ (1 - \exp(t/\tau))/k_BT]\}^{-1} \qquad (3.4)$$

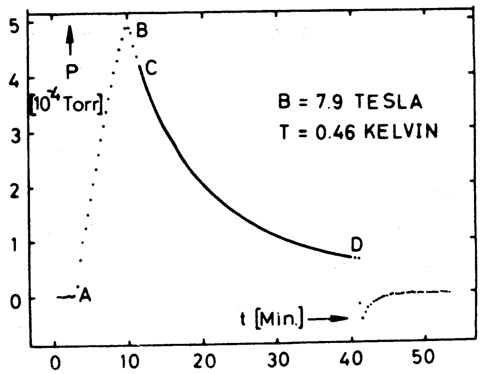

Fig.3.4 Typical pressure fill-decay plot. See text for explanation.

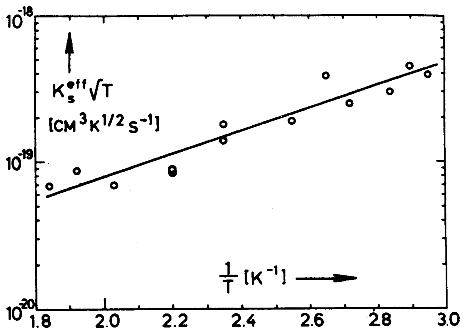

Fig. 3.5 Logarithmic plot of K_s^{eff} vs 1/T. The adsorption energy is determined from the slope.

3.1.4 Results

A typical pressure fill-decay plot is shown in fig. 3.4. The cell is filled for a period of 5-10 min. with $H\downarrow$ starting at point A. At point B the discharge is turned off and the cell cools to the point C, where the temperature is actively stabilized to within a milliKelvin. The pressure decay is then observed for periods up to one hour to point D, where the remaining $H\downarrow$ is destroyed with a bolometer, to establish the baseline of the gauge. The slow negative going pressure transient after triggering is caused by a small leak between the sample chamber and the vacuum chamber of the pressure gauge. This leak only contributed to the first order time constant, but did not influence the second order constant. The data were sampled by a Nicolet 1174 transient recorder and transmitted to a PDP 11 computer. A non-linear least squares fitting procedure was used to fit the data to a function of the form (3.4). The data were corrected for drifts in the baseline of the gauge.

To determine the adsorption energy E_A, K_s^{eff} was measured as a function of temperature in the range 0.34-0.54 Kelvin. All data were taken at a magnetic field of 7.9 Tesla. To extract the adsorption energy E_A from the data we plot $K_s^{eff}\sqrt{T}$ as a function of 1/T as shown in fig. 3.5. The factor $\sqrt{T}$ arises from the temperature dependence of the thermal velocity and the thermal wavelength. From the slope of this plot we find $E_A/k_B = 0.89 \pm 0.07$

Kelvin. Many values of E_A for H↓ have been published in the literature; in table 3-1 we compare them all. Most measurements use some surface process (recombination or relaxation) as a probe, the only exceptions being the measurements of Morrow et al.[8] and Reynolds et al.[9]. Morrow et al.[8] investigated the shift of the hyperfine frequency with NMR at zero field. This quantity is directly related to the surface residence time. These authors also determine E_A from the recombination decay, which gives the same result. This is the only experimental evidence, that the use of the above mentioned factor $\sqrt{T}$ is correct. Recently, a satellite line in the ESR

Table 3-1

Measured binding energies (H on ^{4}He)

E_A(Kelvin)	Method	$K_sB^2/\sqrt{T}$ ($cm^2T^2sec^{-1}K^{-1/2}$)	Measured by
1.15	Hyperfine shift	-	UBC[8]
1.15	Recombination	-	UBC[8]
0.89	Recombination	$2.6x10^{-7}$	Amsterdam[1]
1.01	Recombination	$4.0x10^{-8}$	MIT[11]
1.06	Recombination	$4.1x10^{-8}$	Cornell[13]
1.15	Recombination	$4.0x10^{-8}$	Amsterdam, see section 3.2
1.10	Recombination	$5.7x10^{-8}$	UBC[14]
0.96	Recombination	$5.9(5)x10^{-8}$	Harvard[10]
1.00	ESR	-	UBC[9]

spectrum of H↓ was observed by Reynolds et al.[9], shifted from the main resonance. The shift was density dependent. This feature was attributed to adsorbed atoms, feeling a slightly different field due to magnetic dipole interactions [16]. This has enabled still another measurement of E_A.

The values for the binding energy in table 3-1 range from 0.89 to 1.15 Kelvin. This spread in E_A results in an unacceptably large uncertainty in the surface coverage, especially at low temperatures. At a temperature of 100 mK this leads to a factor 13 uncertainty in the surface coverage. Possible errors in the determination of E_A may result from[10]: thermometry, helium-3 contamination, unknown or varying polarization of the lower two hyperfine states, time varying surface area due to H_2 build up, heating of the gas due to recombination and a Kapitza resistance at the gas/film or film/wall interface. We will return to this point in the next section.

3.1.5 Field dependence of the surface recombination rate

The field dependence was measured at a temperature of 0.385 Kelvin in the field range between 5 and 10 Tesla. For the case of strong fields, the model, described in chapter 1, predicts a field dependence of the form: $K_s^{eff}(B) = K_s^{eff}(0) x 2\epsilon^2$. The results are shown in fig. 3.6, where we plot $(K_s^{eff})^{-1}$ vs B^2. A fairly linear relationship is observed, consistent with the Van der Waals recombination model. The dotted line in fig. 3.6 relates to a value $K_s B^2/\surd T = 2.6 \pm 0.8 * 10^{-7}$ $cm^2 T^2 sec^{-1} K^{-1/2}$. This is about a factor of five larger than most of the measurements in table 3-1. This large difference is related to the difference in binding energy. A more detailed comparision of the results will be given in section 3.2.

3.1.6 Implications for BEC

These results have serious implications for observing BEC in this type of geometry. It has been shown, that in order to attain BEC, the surface must be saturated with a surface coverage $n_s^{sat} = E_A/2\alpha_2 = 10^{14}$ cm^{-2} (see section 1.2). The maximum surface coverage in this experiment is about 10^{11} cm^{-2}. Under BEC conditions, surface recombination will therefore be five orders of magnitude faster than in the present experiment. If the sample container is free from magnetic impurities, then the overall rate will be determined by magnetic dipolar relaxation, as a result of the relaxation bottleneck [40].

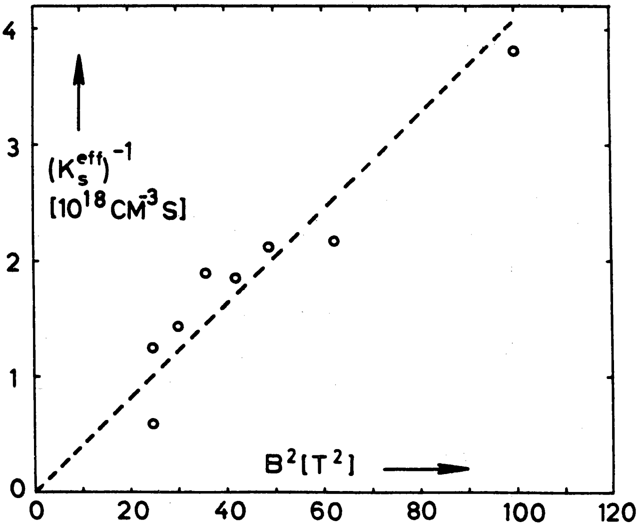

Fig. 3.6 Field dependence of the surface recombination rate plotted as $(K_s^{eff})^{-1}$ *vs* B^2 *for* $T = 0.385$ *K.*

Other mechanisms which more severely limit the attainable densities have been found[6,7], but are beyond the scope of this thesis.

A possible means of reducing the surface recombination rate is working with a surface, that has a lower saturation density, and therefore, a lower binding energy. To investigate this aspect, some preliminary experiments were carried out with a 0.2 % ^{3}He-^{4}He mixture. A reduction of $K_s{}^{eff}$ with a factor of 6.1 was observed, compared with the pure ^{4}He case. If this change in K_s^{eff} is completely attributed to a change in adsorption energy, we estimate $E_A/k_B = 0.59$ K for the mixture. Helium-3 floats on top of the helium-4 surface, especially at low temperatures[15]. Therefore, a small addition of ^{3}He may have a large effect. We were unable to get reliable data with more ^{3}He in the system, since the fluctuating ^{3}He vapor pressure contributes to the noise. In a subsequent experiment[17], in which a dilution refrigerator was used to achieve lower temperatures, the binding energy on a saturated ^{3}He-^{4}He mixture was measured to be 0.34 Kelvin. Thus a substantial reduction of the binding energy results from using a mixture, but this leaves the role of the surface unchanged as being a major barrier to BEC.

3.2 Temperature and field dependence of the surface recombination rate

3.2.1 Introduction

The measurements of the temperature and field dependence, using the method described in section 3.1, were extended to a larger temperature and field range, and carried out in a better defined geometry. This geometry is characterised by a more homogeneous field, leading to a density profile of approximately rectangular shape, and a high impedance to the warm parts of the filling line, which results in a low contribution to the decay rate due to thermal escape. This allowed for the measurement of the rate constant at low values of the magnetic field.

It was verified with ESR that all data were taken under conditions with a nuclear polarization $(n_b - n_a)/(n_b + n_a)$ close to zero. A density determination using ESR combined with a pressure measurement provides information about the temperature of the gas. This technique was used to check that the gas was in thermal equilibrium with the walls of the sample container. The thickness of the helium film was estimated from the current-voltage characteristics of a helium film bolometer; the I-V characteristics were also used to check for the presence of a helium-3 contamination (the addition of a 1 ppm helium-3 impurity was easily observable). A detailed description of the apparatus, used in this experiment, is given in chapter 2.

3.2.2 Temperature dependence results

Two sets of data were taken at a field of 5.6 Tesla, and at estimated film-thicknesses of 42 Å and 48 Å. In the following discussion we will refer to these as the "thin" and the "thick" film respectively. The results are shown in fig. 3.7. Both sets of data yield a two-dimensional recombination cross-section of 0.4 Å. At high temperatures, the data deviate from the fits. We considered several possiblities, to explain this effect: thermal population of the upper hyperfine states, two body recombination with gaseous helium acting as the third body, and thermal escape trough an open ended geometry. As there is a large surface area of about 1 m^2 in the silver sinter in the HEVAC, this last process may effectvely contribute to the second order rate constant. None of these provides a satisfactory explanation of the observed increase of the recombination at high temperatures.

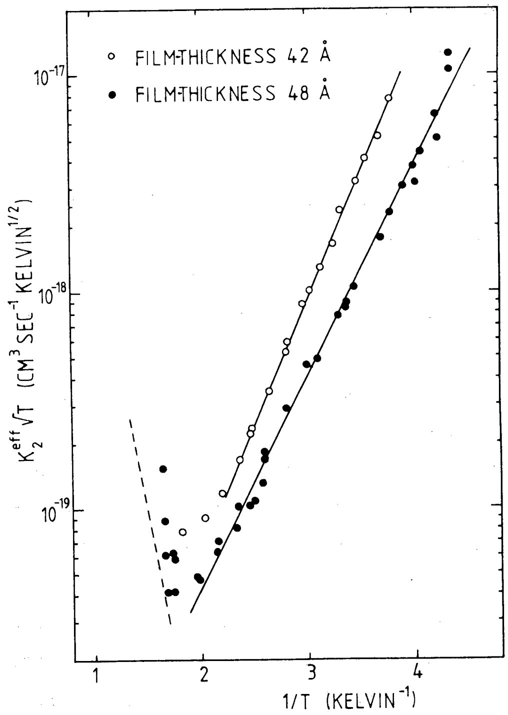

Fig. 3.7. Temperature dependence of the recombination rate at B = 5.6 Tesla. The open circles correspond to a film-thickness of 42 Å and a surface binding energy of 1.31 K. The closed circles correspond to a thickness of 48 Å and an energy of 1.15 K. Dotted line: resonance recombination with Δ = 0.7 K and τ = 7 μs.

A similar effect was observed by Statt[44] and later by Reynolds et al.[20], who measured K_{ab} and K_{aa} as a function of temperature in a 4 Tesla field with ESR. Their sample chamber had a closed geometry. Their data of K_{aa} show an upturn at temperatures above 0.5 Kelvin, which was attributed to resonance recombination (see section 1.3.1). The data were fitted using equation 1.14, yielding a quasi-molecule dissociation energy of 0.7(0.1) Kelvin, and a quasi-molecule lifetime of 7 microseconds. The dotted line in fig. 3.7 corresponds to the same mechanism with the same parameters. The rates, observed in our experiment are somewhat faster than resonance recombination can account for. However, it is difficult to obtain reliable data in this temperature regime, as is witnessed by the large scatter in the data. We conclude therefore that resonance recombination is the most likely process at high temperatures.

The thin film results may be fitted with a surface binding energy of 1.31 Kelvin, and the thick film results with a value of 1.15 Kelvin. A variation of the binding energy with film-thickness may result from the penetration of the Van der Waals potential due to the solid substrate through the film, which affects the binding of the atoms to the surface in two ways: the helium is compressed in the Van der Waals field near the substrate, which leads to a stronger attraction between the liquid and the adsorbed atoms; also the Van der Waals potential due to the solid itself may contribute to the binding. An estimate of the latter effect was made by Zimmerman and Berlinsky[18], and Godfried et al.[10]. At a thickness of 40 Å the effect of the Van der Waals potential is small; we estimate that the Van der Waals potential for a metal is of the order of 10 milliKelvin at a distance of 40 angström[19]. However, the observed change in binding energy is much larger than this value may account for.

These measurements were followed by a systematic study of the dependence of E_A and K_s on the film-thickness by Godfried et al. [10]. They used a capacitive transducer to measure the film-thickness. In fig. 3.8 we plot the effective surface rate at constant temperature and field as a function of film-thickness. The data of Godfried et al. have been scaled to our field and surface to volume ratio. Also shown is their calculated thickness dependence of the rate, based on a model of penetration of the Van der Waals potential of the solid substrate through the liquid. The model predicts a substantial increase of the rate at thicknesses of about 20 Å and below, whereas the experimental data show the influence of substrate effects up to a thickness of about 100 Å. At such a distance from the substrate, the Van der Waals potential has a value of roughly 1 mK.

We have explored the role of surface roughness as a possible explanation for the results, mentioned above. To facilitate the calculations, we consider an eggbox-like surface: a surface covered with hills and valleys of spherical shape, all with the same radius of curvature. We keep this system in contact with an atomically flat surface; the purpose of the flat surface is to provide a reference, as the film thickness is an ill defined quantity on a rough surface. Thus, specifying a film-thickness on the flat surface (in the following discussion denoted by d), sets the chemical potential throughout the system. In fact, the experimentally determined thickness from the bolometer current-voltage characteristic or the thickness gauge capacitance is related to the chemical potential. In the case of the bolometer this is the consequence of the calibration procedure, outlined in section 2.4.

The film distribution in this system is governed by Van der Waals and surface tension forces. We may follow the same lines of reasoning as we did before in connection with sinters (see section 2.4). Within this context, it

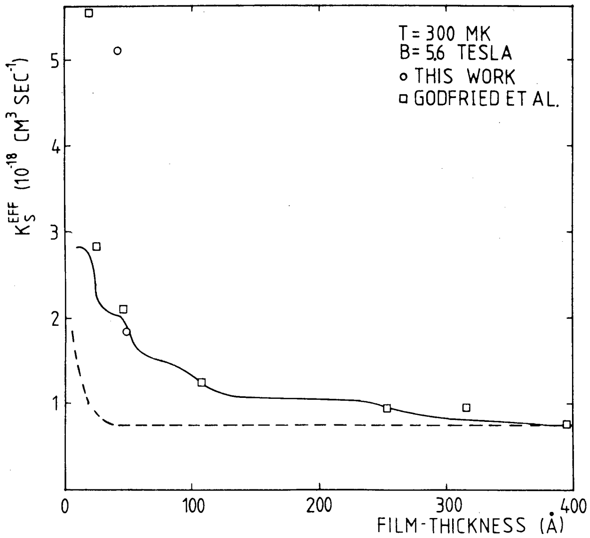

Fig. 3.8. Effective surface recombination rate at constant temperature and field as a function of film-thickness. Squares: measurements by Godfried et al.[10]*. Circles: this work. The dashed curve gives the predicted thickness dependence for a flat surface. The stepped curve gives the calculated dependence for a rough surface.*

is useful to define a critical thickness d_o, where both forces have the same magnitude. For a solid hydrogen substrate, using the potential of Godfried et al. [10] we find $d_o = 3.5\ r^{1/3}$, where r is the radius of curvature (both d_o and r given in Å). If the film-thickness on the flat surface is below this value, then the Van der Waals forces dominate and the film distribution is uniform. If $d > d_o$, then the situation on top of the hills differs from the situation in the valleys. On the hills, the Van der Waals and surface tension forces counteract each other, and tend to stabilize the thickness at a value d_o. In the valleys, both forces act in the same direction and the thickness becomes unstable with respect to variations in d. As soon as $d > d_o$, the valleys become quickly filled with liquid.

Surface roughness, in principle, affects the recombination rate in two ways. On top of the hills, where the film is locally thin due to the surface tension, the Van der Waals potential of the solid substrate enhances the binding of the hydrogen atoms. To give a numerical example, consider a surface covered with spheres with a radius of 100 Å. For $d < 100$Å, about 10 % of the surface will be covered with small potential wells with a depth of 100 mK and a radius of 100 Å. This will increase the overall binding energy by about 10 mK. We conclude that this effect is too small to account for the observed variation of the rate with thickness.

Roughness will also affect the rate via the magnitude of the surface area. As more helium is added to the system, the rough structure of the solid substrate will be smoothed by the film, leading to a smaller surface area. Due to capillary filling of the valleys in the surface, a considerable reduction of the surface area may result if the thickness, as measured by some thickness measuring device, varies by a relatively small amount. We have constructed a roughness distribution that may account for the observed rate variation with thickness as observed by Godfried et al. The distribution consists of four length scales (r = 400 Å, 4000 Å, 40000 Å and 400000 Å). The calculated rate variation with thickness, which follows from the variation of the surface area with thickness, is shown in fig. 3.8. One notes that the area may vary by a factor 2.5. The step-like shape of the curve results from the discrete nature of the distribution.

We summarize our considerations as follows. We have shown that substrate effects are important in both sets of measurements, and that these are much larger than a model, based on penetration of the Van der Waals potential of a flat substrate, can account for. It is possible to construct a surface roughness distribution that explains the results of Godfried et al. However, it is not clear whether such a distribution is realistic. We also note, that the roughness model is inadequate to explain our own experimental results.

Finally, we note that the presence of surface roughness may result in the formation of a potential, which randomly fluctuates along the surface, especially if the film is thin, of the order of 20 Å and below. This is the necessary ingredient for Anderson localization[38]. It does not affect the measurements described, but may be of importance at very low temperatures and low surface densities of hydrogen atoms, if only these localized states are occupied. The usual free particle-like motion along the surface is then blocked; the transport of particles occurs by jumping from one localized state to another, assisted by the absortion or emission of excitations, ripplons in our case. Transport via localized states is observed in electronic systems; it should, at least in principle, be observable in an atomic system too.

3.2.3. Field dependence

The magnetic field dependence was measured at T = 300 mK and T = 381 mK in the field range between 1.5 and 7.5 Tesla. The results are shown in fig. 3.9. At high fields (B > 3 Tesla), the rate is proportional to B^{-2}. At lower fields, a deviation from the square law arises from thermal occupation of the upper hyperfine states. We have calculated the rate as a function of field, assuming a thermal distribution over the four hyperfine states, using a binding energy of 1.15 Kelvin and a two-dimensional cross-section of 0.4 Å for all possible pair collisions:

$$K_s^{eff} = 2\surd 2\ (A_{eff}/V_o)\ f(B)\ \delta_o \bar{v} \lambda_{th}{}^2\ \exp[2E_A/k_BT] \qquad (3.5)$$

The contribution of the four hyperfine states is expressed via f(B) (see section 1.3.1 for the definition of f(B) and the other symbols in this equation). The solid lines in fig. 3.9 are the calculated results. Also shown are the zero field values from Morrow et al.[8]; these values were derived from their data by interpolation and scaling to our surface-to-volume ratio. The agreement between the calculations and the measured data is rather good. At a field of about 2 Tesla the data are almost temperature independent. The contribution of the upper hyperfine states to the rate constant is roughly proportional to $\exp[(2E_A - 2\mu_B B)/k_BT]$. At a field of 1.7 Tesla both Boltzmann factors cancel.

The assumption of thermal equilibrium of the four hyperfine states implies the presence of a fast relaxation process and deserves further investigation. To maintain thermal equilibrium, an electronic relaxation process is needed with a rate, at least comparable to the recombination rate. In search for a candidate, we considered several electronic dipolar and spin-exchange relaxation processes. It turns out that aa-ac spin- exchange in the tail of the density distribution is marginally able to maintain thermal equilibrium.

In fig. 3.10 we show a compilation of all measured data, together with calculated curves for some field values between 0 and 10 Tesla. The solid lines have been calculated using a value E_A = 1.15 K and δ_o = 0.4 Å. Three body recombination with ^{4}He vapor atoms as the third body has been studied by Jochemsen et al.[21]; they observed at high temperatures (≃1 Kelvin) and zero field a density decay of the form

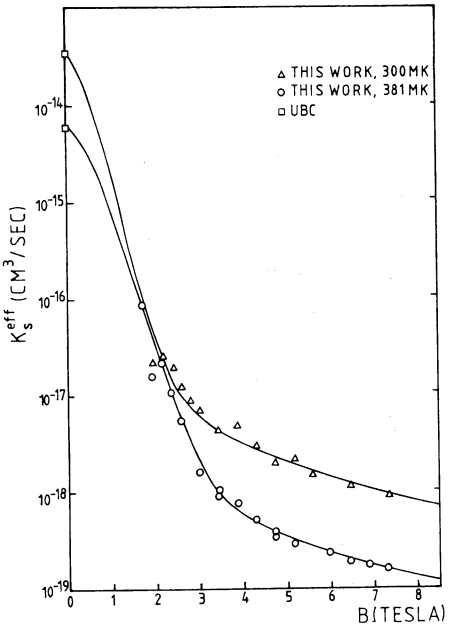

Fig. 3.9. Field dependence of the surface recombination rate. The solid lines have been calculated using equation 3.5, assuming a thermal occupation of the four hyperfine states. The squares were obtained by scaling and interpolating the zero field measurements by Morrow et al.[8].

$$dn_H/dt = -K_3 n_H^2 n_{He} = -K_v n_H^2 \qquad (3.6)$$

with $K_3 = 2.8*10^{-33}$ $cm^6 s^{-1}$, n_H and n_{He} are the densities of the hydrogen and helium gas atoms. The dotted lines in fig. 3.10 have been calculated assuming a field dependence of the form $K_v(B) = K_v(0)*2\epsilon^2$.

All measured data have been scaled to a surface to volume ratio of 10 cm^{-1}. We feel that this is the best way of comparing the experimental data, since an error in E_A directly propagates into the pre-exponential factor $K_s B^{-2} T^{-1/2}$ and vice versa. This causes our initial value for $K_s B^{-2} T^{-1/2}$ to deviate from the values, obtained by others (see table 3-1), although the actual observed rates are in close agreement with one another. A possible explanation of the low value of E_A obtained in our first experiment is the limited temperature range in which the measurements could be carried out. At the highest temperatures, the data might have been affected by resonance recombination in the tail of the density distribution.

In part surface roughness may account for the large variation in K_s

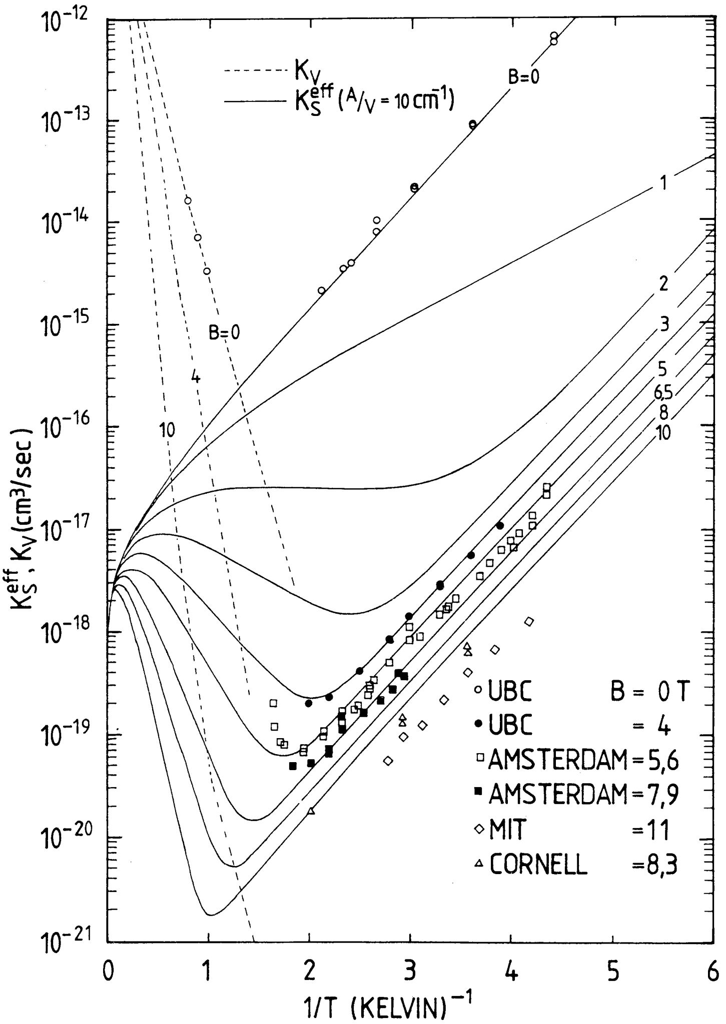

Fig. 3.10. Compilation of all measured values of k_s^{eff} and K_V as a function of 1/T, for H on a ^{4}He surface. Solid lines: calculated field and temperature dependence of K_S^{eff}; dashed lines: calculated K_V.

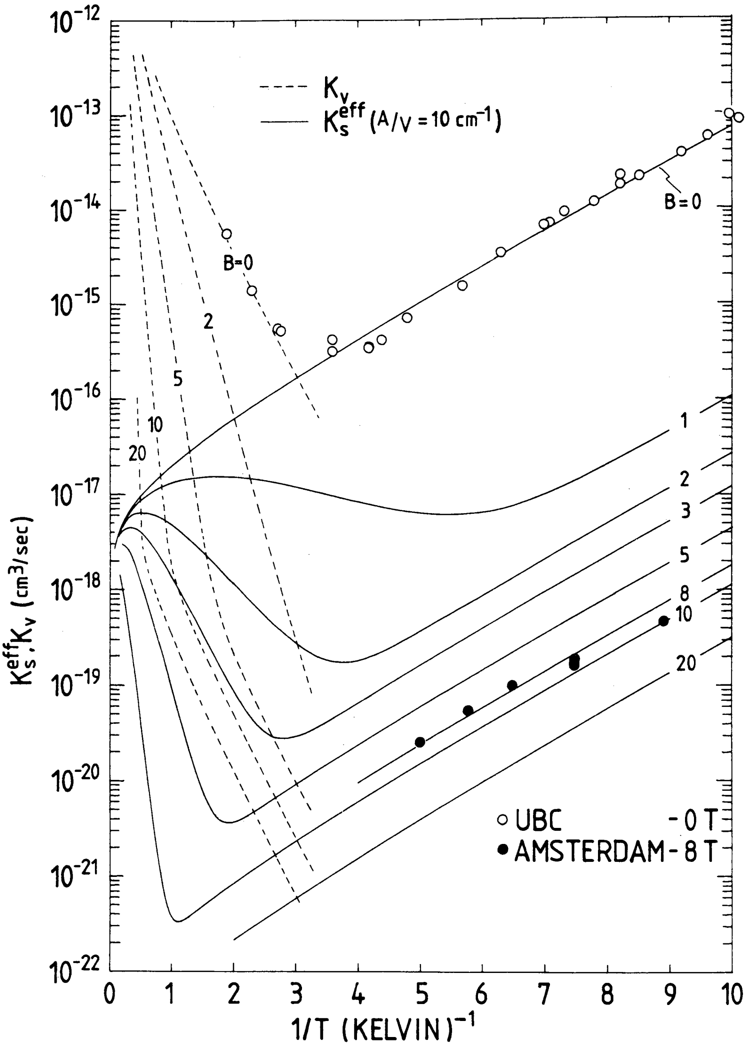

Fig. 3.11. Same as fig. 3.10 for H on a ^{3}He or ^{3}He-^{4}He surface. After Silvera and Walraven[39].

quoted in the literature (see also table 3.1). Leaving aside our own early results, the data in fig. 3.10 still show a variation of 50 % in K_s, indicating that surface roughness may be important, even in the case of thick films.

In fig. 3.11 we give an analogous plot for the data, observed in a ^{3}He covered sample chamber[17,22]. The curves have been calculated using a cross-length $\delta_o = 0.4$ Å and a binding energy $E_A = 0.34$ K. Both plots show qualitatively the same picture. In the case of ^{3}He, bulk recombination at high temperatures is somewhat more important.

3.2.4 Deuterium

Atomic deuterium has a binding energy on liquid helium-4 of 2.6 Kelvin[2] and a recombination cross-length of 400 Å[23]. Since the value of the cross-length exceeds the hydrogen value by three orders of magnitude, it is not obvious that the present Van der Waals recombination model applies to deuterium. No experimental data at low fields are available. In the present apparatus, no observable quantities of deuterium could be stabilized, whereas the first successfull stabilisation of deuterium took place in the system, described in section 3.1. A comparision of both systems provides information that may be of help in the design of an apparatus for stabilizing atomic deuterium.

Both systems differ with respect to their filling lines: in the "old" system, the atoms enter the cold part below 1 Kelvin of the apparatus in a region where the field is about half the value at the center; in the present system, the atoms must travel a distance of about 10 cm along a tube in zero field. Assuming that the present model of recombination also holds in the case of deuterium, the recombination losses in this part of the filling tube may be estimated. Recombination losses in a tube were treated by Walraven and Silvera[24]. We find that a flux of 10^{13} s^{-1} will pass the tube without appreciable losses in a 6 Tesla field at a temperature of .7 Kelvin. If the field however is zero, only a small fraction ($\approx 10^{-4}$) survives without recombination. These results indicate that it is of vital importance to cool deuterium atoms down below 1 Kelvin in a reasonably strong field.

3.3 *Recombination heating*

3.3.1 *Introduction*

Recombination of atomic hydrogen into the molecular state with a dissociation energy of 4.476 eV is accompanied by the production of large amounts of heat. As a result, substantial temperature differences may develop between the gas and the liquid that surrounds the sample, or across the liquid-solid interface near the metal wall of the sample container. This may prevent low temperatures in a high density gas, thus providing another barrier on the route to BEC. In this section an experimental investigation of the heat transfer from the gas to the thermal bath, using a combination of ESR and pressure measurement will be described.

Recombination results in the formation of molecules in a highly excited vibrational-rotational state near the continuum level, releasing their excess energy in a multi-step process, involving several collisions with hydrogen atoms in the gaseous phase or collisions with the surrounding liquid helium surface. Hence there are two distinct paths along which the recombination heat can flow: one goes from the "hot" molecules directly into the liquid and the underlying substrate, the other uses the gas of hydrogen atoms as an intermediate step. We may depict the flow of recombination heat by the following diagram:

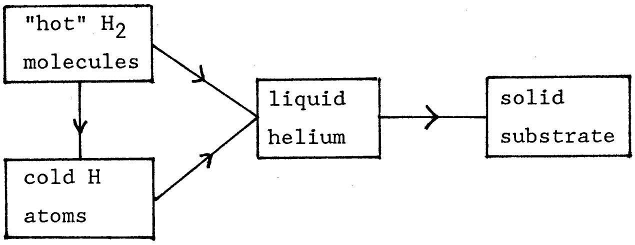

Fig. 3.12 Model of recombination heat flow

Atoms exchange in a single collision with the surface an amount of energy, characterized by the accommodation coefficient a, defined by:

$$a = (T_i - T_r)/(T_i - T_s) \tag{3.7}$$

where T_i is the temperature of the particles that hit the surface, T_r is the temperature of the reflected particles and T_s is the temperature of the surface. The net heat flux $\dot{Q}$from the gas to the surface and the temperature difference $T_g - T_s$ are related by:

$$T_g - T_s = R_k.\dot{Q} \tag{3.8}$$

This linear relationship only holds for small $T_g - T_s$. The Kapitza resistance R_k may be expressed in terms of the accommodation coefficient:

$$R_k = (2k_B\nu a)^{-1} \tag{3.9}$$

where ν is the gas to surface collision rate. The atoms thermalize with the surface either by entering a surface bound state (sticking) or inelastic scattering due to ripplon emission or absorption. Calculations[25-28] show that below 300 mK sticking is the most efficient energy transfer mechanism and that it has a relatively weak temperature dependence: $R_k \simeq 1/T^n$, with $0<n<1$. The accommodation coefficient was measured by Salonen et al. [29,30] on a pure ^{4}He surface, yielding a value of 0.3 at 200 mK, decreasing with increasing temperature. They employed ballistic heat pulses and a steady state heat fluxes to study the energy transfer between the gas and the liquid. Recently, Helffrich et al. [42] found an increasing accommodation coëfficient with increasing temperature using a similar technique. The sticking coëfficient s was measured by Jochemsen et al.[22] using magnetic resonance. They found $s=0.046$ at $T\simeq200$ mK for ^{4}He surfaces and $s=0.016$ for ^{3}He surfaces at $T\simeq100$ mK. Recently, the sticking coëfficient was determined by Berkhout et al.[41] from the flow of hydrogen atoms through a capillary, yielding $s=0.33T$ both for ^{3}He and ^{4}He surfaces. The measured Kapitza resistance between liquid helium and a metal susbstrate such as copper is given by $R_kT^3 = 0.05\ k^4W^{-1}m^2$[31]. Third sound experiments yield a large value of R_k between a thin film and a solid substrate [32].

Little is known about the energy transfer between hot H_2 molecules and the cold gas atoms or the surrounding walls. With known values of the accomodation coefficient, an upper bound of the gas temperature may be obtained assuming that all recombination heat is transferred to the surface

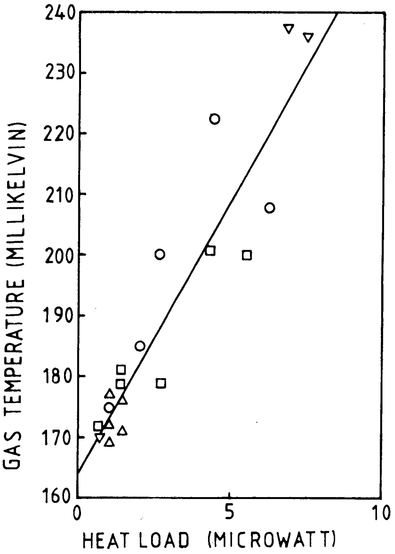

Fig. 3.13 Gas temperature as a function of recombination heating power. The slope gives the Kapitza resistance.

by the gas atoms. The only reliable way of determining the gas temperature is therefore a direct measurement.

3.3.2 Results.

Given the ideal gas law, $T_g = p/(k_B(n_a + n_b))$, the gas temperature may be determined by a simultaneous meausurement of p using a pressure gauge and the total density $(n_a + n_b)$ using ESR. The total heat production Q follows from the time derivative of the total density:

$$\dot{Q} = -V_o.(1/2)E_d \; d(n_a + n_b)/dt \qquad (3.10)$$

where E_d is the dissociation energy per molecule and V_o the effective volume. The derivative $d(n_a + n_b)/dt$ is obtained by differentiating the smoothed ESR data with respect to time. To obtain the data for T_g and $\dot{Q}$, both the pressure and the density in the lower hyperfine states are recorded as a function of time. The experiments were carried out in a ^3He-^4He lined sample chamber, with the wall kept at a temperature of 164 milliKelvin. The results of four runs are plotted in fig. 3.13. At a density of 10^{16} cm^{-3}, the gas heats up 70 mK. The slope of the data yields a Kapitza resistance R_k = 9000 K/W. The scatter in the data results from the differentiation procedure to obtain $\dot{Q}$. In our geometry, the contact area between the sample and the surface is 20

cm^2. Using the relations, given at the introduction of this section, we estimate the Kapitza resistance between the gas and the liquid to have a value of 2000 K/W; the Kapitza resistance at the liquid metal interface is estimated to be 5700 K/W. These results suggest, that the Kapitza resistance at the liquid-metal interface is the most important in our geometry. As this resistance has a stronger temperature dependence than the gas-liquid resistance, we expect it to be more important at low temperatures. The use of a silver sinter generally reduces the temperature drop at this interface. However, this reduction is always limited due to temperature gradients inside the sinter (see section 2.1 for a detailed discussion).

3.4 Search for spin waves

The internal magnetic structure of the hydrogen atom has been predicted to have strong effects on its transport properties[33, 34, 43]. The so called identical spin rotation effect originates from succesive binary collisions between identical particles, transferring their transverse magnetization. This may lead to coherent propagation of spin oscillations. Exchange effects are important if the thermal de Broglie wavelength λ_{th} exceeds the range of the interatomic potential, even in a non-degenerate, weakly interacting gas. This condition is easily met at currently attainable densities. Standing waves may be observed in a closed geometry in a field gradient, driven by an RF field.

Spin waves have been observed in NMR spectra[35,36], in the form of a density dependent modulation. We have undertaken an investigation of the ESR lineshape in a gradient field, to explore the possible existence of these waves in the ESR spectrum. Several derivative spectra at different densities and field gradients were recorded using the frequency modulation technique. An illustrative example is shown in fig. 3.14, which was obtained by integrating the derivative of the ESR spectrum. A reproducible fine structure is always observed, even when the applied gradient is zero. The field gradient merely smears out the main resonance peak. The fine structure varies with the applied field gradient and the microwave frequency, but does not depend on the density. This leads to the conclusion, that the observed fine structure cannot be interpreted in terms of spin waves.

More probably, the observed fine structure in the ESR spectrum is related to an inhomogeneous distribution of the RF field, resulting from reflections

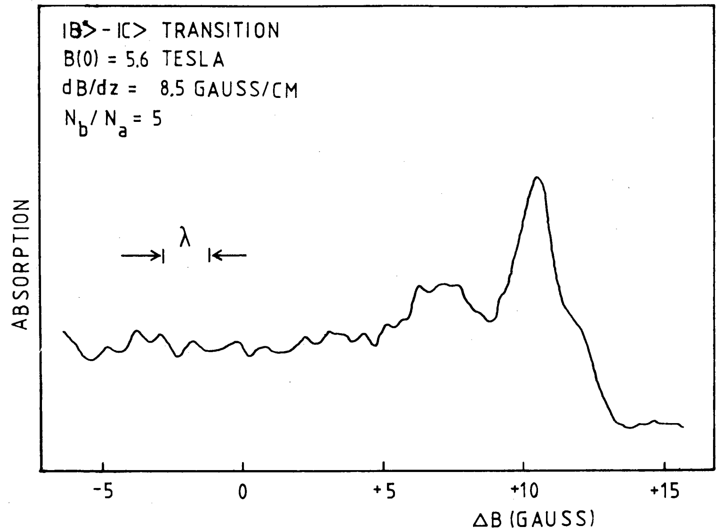

Fig. 3.14. ESR lineshape in a gradient magnetic field. For a given field gradient, the horizontal scale may be translated into an axial distance. The wavelength of the microwave radiation is shown for comparison.

at wall irregularities such as the inlet of the pressure gauge. This effect was discussed in section 2.3, in relation to the observed behavior of the ESR lineshapes as a function of frequency and field. If we assume that the spatial density distribution is uniform and the field distribution is linear, then fig. 3.14 may be considered as a one dimensional mapping of the RF field distribution. With the known value of the field gradient, the horizontal scale may be converted into a distance along the axis. In fig. 3.14, the pattern is probed over a distance of 1.5 cm. The wavelength λ of the RF radiation is shown for comparison. The close correspondence between λ and the typical period of the oscillations supports the idea of a relationship between the fine structure in the spectra and a non-uniform distribution of the RF field.

Finally we note that Statt[37] also failed to observe spin waves in the ESR spectrum. These results indicate that for some reason it is more difficult to observe these waves with ESR than with NMR. We also note that we did not design our system with the possibility of these waves in mind.

References

1. A.P.M. Mattheij, J.T.M. Walraven and I.F. Silvera, Phys. Rev. Lett. 46, 668 (1981).
2. I.F. Silvera and J.T.M. Walraven, Phys. Rev. Lett. 45, 1268 (1980).
3. J.T.M. Walraven, I.F. Silvera and A.P.M. Mattheij, Phys. Rev. Lett. 45, 449 (1980).
4. K. Huang in *Studies in Statistical Mechanics II,* J. de Boer and G.E. Uhlenbeck eds., North-Holland Publ. Co. Amsterdam (1964).
5. D.G. Friend and R.D. Etters, J. Low Temp. Phys. 39, 409 (1980).
6. R. Sprik, J.T.M. Walraven and I.F. Silvera, Phys. Rev. Lett. 51, 479 (1983).
   R. Sprik, J.T.M. Walraven and I.F. Silvera, Phys. Rev. B32, 5668 (1985).
7. H.F. Hess, D.A. Bell, G.P. Kochanski, D. Kleppner and T. Greytak, Phys. Rev. Lett. 51, 483 (1983).
   H.F. Hess, D.A. Bell, G.P. Kochanski, D. Kleppner and T. Greytak, Phys. Rev. Lett. 52, 1520 (1984).
   D.A. Bell, H.F. Hess, G.P. Kochanski, S. Buchman, L. Pollack, Y.M. Xiao, D. Kleppner and T. Greytak, Phys. Rev. B34, 7670 (1986).
8. M. Morrow, R. Jochemsen, A.J. Berlinsky and W.N. Hardy, Phys. Rev Lett. 46, 195 (1981); erratum 47, 455 (1981).
9. M.W. Reynolds, I. Shinkoda, W.N. Hardy, A.J. Berlinsky, F.W. Bridges and B.W. Statt, Phys. Rev. B31, 7503 (1985).
10. H.P. Godfried, E.R. Eliel, J.G. Brisson, J.D. Gillaspy, C. Mallardeau, J.C. Mester, and I.F. Silvera, Phys. Rev. Lett. 55, 1311 (1985).
11. R.W. Cline, T.J. Greytak and D. Kleppner, Phys. Rev. Lett. 47, 1195 (1981).
12. R. Sprik, J.T.M. Walraven, G.H. van Yperen and I.F. Silvera, Phys. Rev. Lett. 49, 153 (1982).
13. B. Yurke, J.S. Denker, B.R. Johnson, N. Bigelow, L.P. Levy, D.M. Lee and J.H. Freed, Phys. Rev. Lett. 50, 1157 (1983).
14. B.W. Statt, W.N. Hardy, A.J. Berlinsky and E.J. Klein, Journal of Low Temp. Phys. 61, 471 (1985).
15. F.M. Ellis, R.B. Hallock, M.D. Miller and R.A. Guyer, Phys. Rev. Lett. 46, 1461 (1981).

16. A. Lagendijk, Phys. Rev. B25, 2054 (1982).
17. G.H. van Yperen, A.P.M. Mattheij, J.T.M. Walraven and I.F. Silvera, Phys. Rev. Lett. 47, 800 (1981).
18. D.S. Zimmerman and A.J. Berlinsky, Can. J. Phys 61, 508 (1983).
19. E. S. Sabisky and C.H. Anderson, Phys. Rev. A7, 790 (1973).
20. M.W. Reynolds, I. Shinkoda, R.W. Cline and W.N. Hardy, Phys. Rev. B34, 4912 (1986).
21. W.N. Hardy, M. Morrow, R. Jochemsen, B.W. Statt, P.R. Kubrik, R.M. Marsolais and A.J. Berlinsky, Phys. Rev. Lett 45, 453 (1981).
22. R. Jochemsen, M. Morrow, A.J. Berlinsky and W.N. Hardy, Phys. Rev. Lett. 47, 852 (1981).
23. R. Mayer and G. Seidel, Proc. LT 17, 455 (1984).
24. J.T.M. Walraven and I.F. Silvera, Rev. Sci. Inst. 53, 1167 (1982).
25. B. Castaing and M. Papoular, J. Phys. Lett. 44, L-537 (1983).
26. Yu. Kagan, G.V. Shlyapnikov and N.A. Glukhof (1985), JETP Lett. 40, 1072 (1984).
27. B. W. Statt, Phys. Rev. B32, 7160 (1985).
28. V.V. Goldman, Phys. Rev. Lett. 56, 612 (1986).
29. K.T. Salonen, I.F. Silvera, J.T.M. Walraven and G.H. van Yperen, Phys. Rev. B 25, 6002 (1982).
30. K.T. Salonen, S. Jaakkola, M. Karhunen, E. Tjukanov and T. Tommila, Proc. LT 17, Physica, p. 543.
31. O.V. Lounasmaa, 'Experimental Principles and Methods below 1 K', Academic Press (New York 1974).
32. J.E. Rutledge, W.L. McMillan and J.M. Mochel, Physica 107B, 401 (1981).
33. C. Lhuillier and F. Laloë, J. de Phys. 43, 197 (1982).
34. C. Lhuillier and F. Laloë, J. de Phys. 43, 225 (1982).
35. B.R. Johnson, J.S. Denker, N. Bigelow, L.P. Levy, J.H. Freed and D.M. Lee, Phys. Rev. Lett. 52, 1508 (1984).
36. T.O. Niinikoski, S. Pentillä, J.-M. Rieubland and A. Rijllard, Proc. 4th. Int. Workshop on Polarized Target Materials and Techniques W. Meyer Ed., Physikalisches Institut, Universitah"t Bonn (1985).
37. B.W. Statt, Ph.D. Thesis, University of British Columbia, unpublished (1984).
38. P.W. Anderson, Phys. Rev. 109, 1492 (1958).
39. I.F. Silvera and J.T.M. Walraven, *Progress in Low*

Temperature Physics, Vol. X, Chapter D, D. Brewer Ed., North Holland Publ. Amsterdam (1986).

40. B.W. Statt and A.J. Berlinsky, Phys. Rev. Lett <u>45</u>, 2105 (1980).
41. J.J. Berkhout, E.J. Wolters, R. van Roijen, J.T.M. Walraven, Phys. Rev. Lett. <u>57</u>, 2387 (1986).
42. J. Helffrich, M.P. Maley, M. Krusius and J.C. Wheatley, Phys. Rev. <u>B34</u>, 6550 (1986).
43. J.P. Bouchaud and C. Lhuillier, J. Phys. <u>46</u>, 1781 (1985).
44. B.W. Statt, private communication.

CHAPTER IV

ESR PUMPING EXPERIMENTS IN SPIN-POLARIZED ATOMIC HYDROGEN

A.P.M. Mattheij[+], J. van Zwol[++], J.T.M. Walraven,
Natuurkundig Laboratorium, Universiteit van Amsterdam,
Valckenierstraat 65, 1018 XE Amsterdam, The Netherlands.

Isaac F. Silvera
Lyman Laboratory of Physics, Harvard University,
Cambridge, MA 02138, USA.

Pumping experiments were carried out in atomic hydrogen using an ESR technique. A model of the decay of the four hyperfine states in the presence of a moderately strong resonant microwave field is described and compared with experimental results. The results indicate that due to spin exchange relaxation, it is difficult to influence the nuclear polarization of the lower hyperfine states by means of ESR pumping. The model is applied to the design of an ESR operated beam source of spin polarized atomic hydrogen. We estimate that in our experiments the maximum flux of particles, ejected from the source was $5x10^{13}$ sec^{-1}.

[+] Present address: Hogeschool West Brabant, PO Box 90.116,
4800 RA Breda, The Netherlands.

[++] Present address: Philips Natuurkundig Laboratorium, PO Box 80.000
5600 JA Eindhoven, The Netherlands.

Introduction

Electron spin resonance has proven to be a valuable tool in the study of the decay kinetics of spin polarized atomic hydrogen. Using ESR, the densities in the lower hyperfine states may be determined separately. ESR has been succesfully applied to study various magnetic relaxation and recombination processes[1-4], and to observe atomic hydrogen in a surface bound state[3]. Alternatively, instead of using ESR as a detection scheme, it may be applied at a high power level to directly influence the populations of the hyperfine states. In a strong resonant microwave field, the electron spins of the atoms will be reversed, which results in the creation of electron spin-up atoms in a background gas of spin-down atoms. The atoms in the upper hyperfine states, created by ESR in an inhomogeneous magnetic field, will be driven by magnetic forces to low magnetic field regions, or recombine with spin-down atoms. ESR-pumping and subsequent ejection from a magnetic field has been proposed as a means of production of a doubly spin polarized atomic hydrogen beam [5]. Conceivably, very pure doubly polarized hydrogen may be produced by removing the |a> state atoms with ESR [6]. To explore these potential applications of the ESR pumping technique, a study was made of the effect of microwave pumping on the decay of the lower hyperfine state densities. The pumping experiments were carried out in a ^{3}He-^{4}He lined sample chamber at a temperature of 160 mK and a magnetic field of 5.6 Tesla. We shall present a model of ESR pumping and beam extraction, and compare this model with experimental results. Our model will include various processes, such as recombination, spin-exchange relaxation, diffusion and effusion (escape from the source). Our results show that at moderate densities spin exchange plays a crucial role in relaxing the upper hyperfine states before they can be ejected, thus giving substantially different results than predicted from a more naive picture. Our model is used to analyze the limitations and the optimum operating conditions of an ESR pumped beam source.

A model for the density decay during microwave pumping

First we briefly discuss our experimental geometry, sketched in fig. 1(a). The apparatus is the same as the one used by Van Yperen et al.[1] with some minor modifications. For a more detailed description of the apparatus,

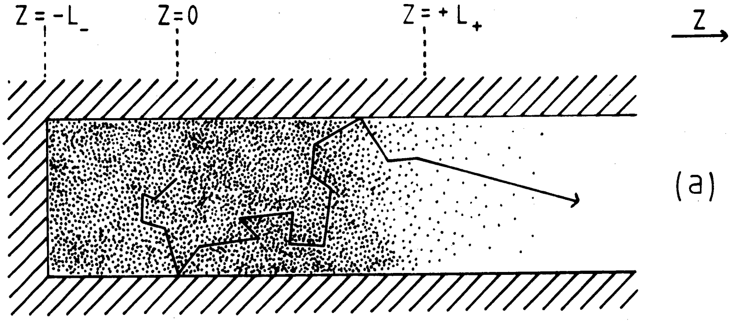

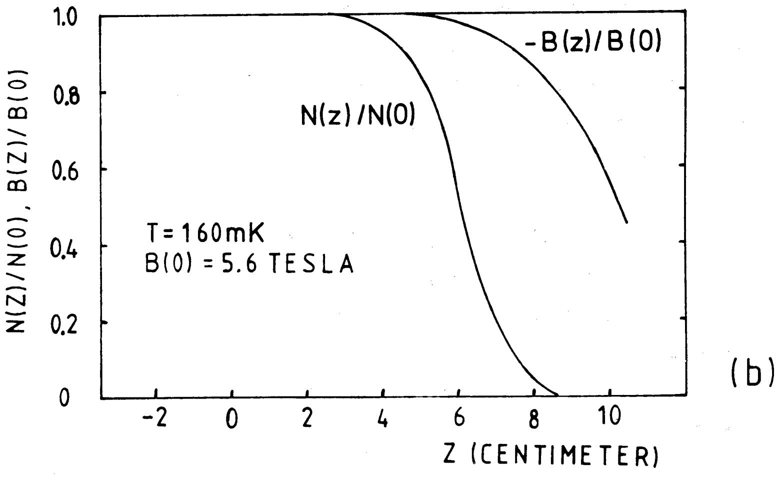

Fig. 1.a. Experimental geometry. Electron spin-up atoms are created by ESR in a background gas of spin-down atoms. A typical trace of a spin-up particle is shown.

Fig. 1.b. Magnetic field distribution and equilibrium density distribution of the lower hyperfine states.

the reader is referred to this paper. The spectrometer is of a FIR broadband design, operating at a frequency of 157 Ghz, and a central field of 5.6 Tesla. It consists of a long cylindrical tube, filled with a localized sample. Changes in the transmission due to the presence of the sample are detected by a semiconductor bolometer, which operates at a temperature of 0.5 Kelvin. ESR transitions create a small population of electron spin-up atoms in the center of the magnetic field, in the middle of a background gas of spin-down atoms. In fig. 1(a) we also depict a possible path of a spin-up atom. In fig. 1(b) we show a calculated typical axial density distribution of the atoms in the lower hyperfine states together with the magnetic field profile. The density profile is approximately rectangular in shape, and has a length of 10 cm, extending from $z = -L_-$ to $z = L_+$. In our coordinate system, $z = 0$ corresponds to the center of the magnetic field and $z = -L_-$ corresponds to the location of a mylar window, where the density abruptly falls to zero. The width of the zone at the field center where the ESR transitions are induced is determined by the field homogeneity. At resonance, this zone has a width of about 1 cm in our system. In the following treatment we shall for simplicity assume that all transitions take place at $z = 0$. To escape without recombination at the walls, the atoms with reversed spin have to traverse the zone to $z = L_+$, a distance of about 6 centimeter, where the field gradient is practically zero and where their motion is diffusion like due to collisions with the background gas and the sample container walls. Collisions in the gas phase may result in spin exchange, while wall collisions may result in recombination with atoms in the lower hyperfine states. Once the spin-up atoms have left the background gas, they will be rapidly accelerated due to the field gradient.

The calculation of the temporal behavior of the densities of the four hyperfine states in the presence of a strong resonant microwave field involves the solution of four coupled partial differential equations, describing the occupation of the four hyperfine levels as a function of space and time. We use a one-dimensional treatment for simplicity. The form of these equations is governed by conservation of mass, including terms due to recombination, relaxation, ESR and transport due to diffusion and drift in the field gradient. Using a shorthand notation a,b,c,d for $n_a(z,t)$, $n_b(z,t)$, $n_c(z,t)$ and $n_d(z,t)$, and $n = a + b + c + d$ the equations are

$$\partial a/\partial t = -\,2K_{aa}\,a^2 - K_{ab}\,ab - K_{ac}\,ac - K_{ad}\,ad + G^{imp}\,(b - a)$$

$$+\,G_{ex}\,(bd - ac) - W_{ad}^{ESR}\,(a - d) - \partial J_a/\partial z + G_{ad}{\downarrow}\,nd \qquad (1a)$$

$$\partial b/\partial t = -\,K_{ab}\,ab - K_{bc}\,bc - K_{bd}\,bd - G^{imp}\,(b - a)$$

$$-\,G_{ex}\,(bd - ac) - W_{bc}^{ESR}\,(b - c) - \partial J_b/\partial z + G_{bc}{\downarrow}\,nc \qquad (1b)$$

$$\partial c/\partial t = -\,2K_{cc}\,c^2 - K_{ac}\,ac - K_{bc}\,bc - K_{cd}\,cd$$

$$+\,G_{ex}\,(bd - ac) + W_{bc}^{ESR}\,(b - c) - \partial J_c/\partial z - G_{bc}{\downarrow}\,nc \qquad (1c)$$

$$\partial d/\partial t = -\,K_{ad}\,ad - K_{bd}\,bd - K_{cd}\,cd$$

$$-\,G_{ex}\,(bd - ac) + W_{ad}^{ESR}\,(a - d) - \partial J_d/\partial z - G_{ad}{\downarrow}\,nd\,. \qquad (1d)$$

The K's refer to the two-body surface-recombination rate constants. As the densities in our experiments do not exceed a value of 10^{16} cm^{-3}, we neglect all three-body terms. The impurity-relaxation rate constant for the lower hyperfine states is denoted by G^{imp}, $G_{ad}{\downarrow}$ and $G_{bc}{\downarrow}$ are the two-body dipolar relaxation rate constants for d→a and c→b relaxation[11]. We neglect two-body dipolar relaxation of the lower hyperfine states, as it is dominated by impurity relaxation in our experiments. The rate constant for spin-exchange relaxation is given by G_{ex}. In a strong magnetic field, the only spin exchange channel with a non-vanishing cross section involves collisions between ac or bd pairs[7]. This process is normally unimportant at strong fields, if the occupation of the upper hyperfine states is zero. However, in the case of a small population of the upper states, in the present case created by ESR, the spin-exchange rate may be very important. The rate constants W_{ad}^{ESR} and W_{bc}^{ESR} represent the transition rates due to ESR; as outlined before, we assume that all transitions take place at $z = 0$ or $W^{ESR}(z) = W^{ESR}\,\delta(z)$, with $\delta(z)$ the delta function. As spin-up atoms after generation by ESR may relax back to the lower hyperfine states, the effective generation rate is reduced. For this reason we will not treat these relaxation terms explicitly, but rather include them in the net ESR generation rates. Finally, J_a, J_b, J_c and J_d are the current densities due to diffusion or migration; their form will be discussed in the following sections.

In the following we shall solve these equations with a simple approximate model, rather than finding a rigorous solution, for instance by means of a Monte Carlo simulation. The analysis yields a rather simple picture in terms of a few characteristic lengths, and explains all of the salient features of the pumping experiments. We estimate the accuracy of our model to be of the level of tens of percent.

In our experiments, to be described later, with a moderately strong microwave power of about 100 nW, it takes at least a hundred seconds to remove the sample. With equal occupations of the four hyperfine states, the gas has a lifetime of a fraction of a second at a total density of 10^{16} cm^{-3}. This implies that the densities of the upper hyperfine states are small compared to the lower hyperfine state densities. This considerably simplifies the analysis. The recombination terms in equations (1a-1d) containing products of upper hyperfine state densities and the contributions of these states to the ESR transition rates may be neglected. Furthermore, we treat the density distributions as quasi stationary, neglecting transient effects such as switching on the microwave field. This allows us to effectively decouple the time and the spatial dependence of the densities. To justify this step, we estimate the time required to build up a stationary density in the upper hyperfine states. After a time t, the spin-up atom has diffused over an average distance $<z> = (2Dt)^{1/2}$, where D is the diffusion coefficient. An electron spin-up atom therefore roughly spends a time $\tau = L_+^2/2D$ in the background gas, before it escapes to low field. We find $\tau = 0.1$ sec. at a total density of 10^{16} cm^{-3} (a more detailed discussion of diffusion processes will be given later). After switching on the microwave field, the density in the upper hyperfine states builds up with the same time constant τ. As the total density decays on a much slower time scale, we may regard the spatial density distributions as quasi stationary. Thus we may proceed in two steps: first calculate the density distributions, neglecting the time derivatives of the densities in equations (1a-1d), and then solve the rate equations for the densities, averaged over the spatial distributions. Our final object will be the calculation of the recombination losses, the intensity of the emerging beam of spin-up atoms and the nuclear polarization of the beam.

Density distributions

Our system, sketched in fig. 1b, may be divided into three parts: the central part where the field gradient is vanishingly small, a zone where the field falls off approximately linearly, and a zone where the field is almost zero. Spin-up atoms, entering the zero-field region, will eventually recombine there, as they have a small probability to return to the field center. We assume that all densities are zero in the zero-field region and also neglect the tail in the density distribution of the lower hyperfine states beyond $z = L_+$. We approximate the real field distribution by a field having a trapezoidal shape:

$$B(z) = B(0) \qquad z < L_+, \tag{2a}$$

$$B(z) = B(0)\,[1 - (z - L_+)/\Delta z] \qquad L_+ < z < L_+ + \Delta z, \tag{2b}$$

$$B(z) = 0 \qquad z > L_+ + \Delta z. \tag{2c}$$

where Δz is the distance over which the field drops from its maximum value to zero. In our geometry the field gradient has a value of approximately 1 Tesla/cm and $\Delta z = 5.6$ cm.

In the central portion of the density distribution, the atomic motion is diffusive, and the current density is of the form $J = -D\partial n/\partial z$, where D is the diffusion coefficient. The differential equations for the quasi-stationary density distributions of the upper hyperfine states follow from equations (1c) and (1d). Retaining only the leading terms, we get

$$D\,(d^2/dz^2)\,c(z) = K\,(a + b)\,c(z) + G_{ex}\,[ac(z) - bd(z)] \tag{3a}$$

$$D\,(d^2/dz^2)\,d(z) = K\,(a + b)\,d(z) - G_{ex}\,[ac(z) - bd(z)] \tag{3b}$$

G_{ex} is the spin-exchange rate constant and we have assumed that all recombination processes between spin-up and spin-down atoms have a common rate constant K. Using a spin-exchange cross section of 1 Å^2 [12] we find $G_{ex} = 8.2\times10^{-13}$ cm^3/sec. The surface recombination rate has been measured by Hardy et al. [8] for a ^{3}He surface and by Van Yperen et al. [9] for ^{3}He-^{4}He mixtures. Using a binding energy of 0.39 K and a two-dimensional cross length of 0.18 Å for all processes involving a spin-up and a spin-down particle we find $K = 2.3\times10^{-15}$ cm^3/sec at a field of 5.6 Tesla and a temperature of 0.16 Kelvin.

Both particle-wall and particle-particle collisions contribute to the diffusion coefficient. The overall diffusion is estimated by simply adding the flow impedance due to both kinds of collisions; this gives

$$1/D = 1/D_o + 1/D_k \ , \tag{4}$$

where $D_k = (2/3)a\bar{v}$ is the Knudsen diffusion constant (a is the tube radius and $\bar{v}$ the thermal velocity). Here we neglect specularity in atom-wall collisions as observed by Berkhout et al.[13]. This seems justified as no particular care was taken to obtain a flat substrate for the helium film. Our results are not too sensitive to the value of the diffusion coefficient. We use $D_o\ (a + b) = 1.8\times10^{18}$ cm^{-1}sec^{-1}. [10]

Another set of two equations, similar to equation (3a) and (3b), holds for the lower hyperfine state distributions, with additional terms for a-a and a-b recombination and b-a relaxation. To create spin-up atoms at $z = 0$, a supply of down-state atoms by diffusion is needed. The density gradients in the four hyperfine states are therefore of the same order of magnitude. Assuming that the densities of the upper states are small compared to the lower state densities, one expects that the presence of the upper state distributions will cause a relatively small density variation along the z-axis in the lower states. We shall neglect this perturbation of the lower states. Then the spin-down distributions reduce to the equilibrium distributions, sketched in fig. 1b, which we approximate by a rectangular distribution, extending from $z = -L_-$ to $z = +L_+$.

It is instructive to introduce three characteristic length scales to express the relative importance of recombination and spin-exchange phenomena:

$$L_{rec} = [D/(K\ (a + b))]^{1/2} \tag{5a}$$

$$L^c_{ex} = [D/(G_{ex}\ a)]^{1/2} \tag{5b}$$

$$L^d_{ex} = [D/(G_{ex}\ b)]^{1/2} \tag{5c}$$

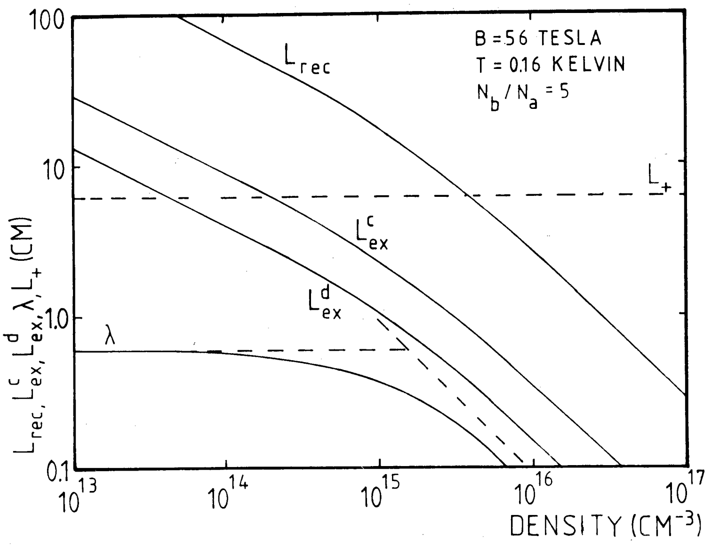

Fig. 2. Density dependence of the characteristic lengths L_{rec}, L^c_{ex}, L^d_{ex} and the mean free path ℓ. Also shown is the characteristic length scale of the experimental geometry (L_+).

In terms of these quantities, equations (3a) and (3b) may be rewritten:

$$(d^2/dz^2)\ c(z) = (L_{rec})^{-2}\ c(z) - (L^c_{ex})^{-2}\ c(z) + (L^d_{ex})^{-2}\ d(z) \qquad (6a)$$

$$(d^2/dz^2)\ d(z) = (L_{rec})^{-2}\ d(z) + (L^d_{ex})^{-2}\ c(z) - (L^d_{ex})^{-2}\ d(z)\ . \qquad (6b)$$

The physical meaning of L_{rec}, L^c_{ex} and L^b_{ex} may be understood as follows. A lifetime $\tau = (Kn)^{-1}$ is associated with the recombination process, corresponding to an average diffusion length of $(2D\tau)^{1/2}$. The quantity L_{rec} may thus be regarded as the typical distance a spin-up particle drifts in the axial direction before it is lost by recombination with a down-state atom. Similar considerations apply to L^c_{ex} and L^d_{ex}. From equations (6a) and (6b) it is clear that these lengths determine the contours of the density distributions.

The density dependence of all relevant characteristic lengths is plotted in fig. 2. At all densities a constant nuclear polarization $n_b/n_a = 5$ has been assumed. At low densities ($<10^{14}cm^{-3}$) the particles principally collide with the walls, and the mean free path is of the order of the diameter of the sample chamber; in this density regime L_{rec}, L^{c}_{ex} and L^{d}_{ex} are proportional to $n^{-1/2}$. In the high density regime ($>3\times10^{15}$cm^{-3}) collisions in the gas phase dominate and these lengths, together with the mean free path λ are proportional to n^{-1}. In fig. 2 the asymptotic behavior at low and high densities is also shown (dashed line). From the figure it is easy to observe which processes are important at a given density. If the corresponding characteristic length is longer than L_{+}, the width of the distribution, then the particle may escape, without getting involved in the process under consideration (recombination or spin exchange).

The experiments were carried out in the density regime of 10^{15}-10^{16} cm^{-3}, where $L_{rec} \simeq L_{+}$; from the behavior of L^{c}_{ex} and L^{d}_{ex} it is clear that a flipped spin is involved in several spin-exchange collisions before it is ejected.

Adding equations (6a) and (6b) gives a simple differential equation for the total spin-up distribution in the central field region:

$$(d^2/dz^2)\ [c(z) + d(z)] = L_{rec}^{-2}\ [c(z) + d(z)]\ . \tag{7}$$

The solution of this equation is a sum of exponentials.

In the region $z > L_{+}$, the spin-up particles are driven to low-field regions by the density and field gradients. The diffusional motion is slowed down by wall collisions. In a field gradient, the atoms move with a drift velocity $\mu|\mathrm{grad}\ B|$. Here the mobility μ is given by

$$\mu = D_k\mu_B/k_BT\ , \tag{8}$$

where D_k is the Knudsen diffusion constant and μ_B the Bohr magneton. Summing the contributions from the density gradient (diffusion) and the field gradient (drift) leads to the following expression for the current density:

$$J = -\ D_k\ dn{\uparrow}(z)/dz\ -\ n{\uparrow}D_k\mu_B/k_BT\ dB/dz \tag{9}$$

where $n{\uparrow} = n_c + n_d$. Since there is no loss of particles due to recombination, the current density should be independent of z. This leads to the following differential equation for the density distribution:

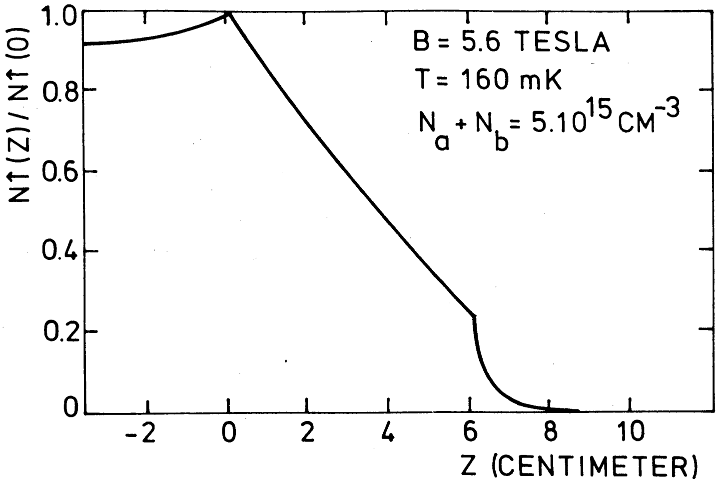

Fig. 3. Normalized spin-up density distribution.

$$d^2n\uparrow/dz^2 - 1/L_B \; dn\uparrow/dz = 0 \; . \tag{10}$$

The spin-up density falls off exponentially in this region with characteristic length L_B, where $1/L_B = -\mu_B/k_BT \; dB/dz$. For our geometry L_B has a value of 0.24 cm. The solution of (10), satisfying the boundary condition $n\uparrow(L_+ + \Delta z) = 0$ is given by

$$n\uparrow(z) = [n\uparrow(L_+)/(f - 1)] \; [f - \exp((z - L_+)/L_B)] \tag{11a}$$

$$f = \exp[\mu_B B(0)/k_BT] \; . \tag{11b}$$

The resulting particle flux Φ is given by

$$\Phi = AD_k/L_B \; (f/(f - 1)) \; n\uparrow(L_+) \simeq AD_k \; n\uparrow(L_+)/L_B \tag{12}$$

Here A is the cross sectional area of the tube.

The last step in finding the spin-up density distribution is to match the solution in the gradient-free region and the density distribution in the gradient zone. The distributions must satisfy the following boundary conditions:

-no flux at the location of the mylar window, i.e. $d(n_c + n_d)/dz = 0$ for

$z = -L_-$;

-the sum of the fluxes at $z = 0$ in the positive and negative z-direction equals the ESR generation rate;

-the density distributions and the particle flux are continuous functions of z, except at $z = 0$, where a discontinuity exists in the flux.

The spin-up density at the field center may be found by solving the coupled equations (1a-1d). A typical spin-up distribution is shown in fig. 3. The estimated density of the upper hyperfine states at $z = 0$ under conditions typical for our pumping experiments is of the order of 10^{12} cm^{-3}.

To calculate the individual |c> and |d> state distributions, the coupled differential equations (6a) and (6b) have to be solved. It follows from our analysis that the individual distributions differ from the sum distribution in a region near $z = 0$ of width L_{ex}^{c} or L_{ex}^{d} due to the spin-exchange terms. The distribution of the state which is created by ESR shows a peak, more pronounced than the maximum of the sum distribution, whereas the other state shows a dip at this location. Since in our experiment L_{ex}^{c} and $L_{ex}^{d} \ll L_+$, we may with reasonable accuracy put the individual distributions equal to the sum distribution.

Once the density distributions are known for the various hyperfine levels, the losses due to recombination and the particle flux due to ejection at $z = L_+$ are easily calculated as a function of the total density of the lower hyperfine states. As the density distributions of the |c> and |d> states are the same, it is convenient to express the ejection fluxes Φ_c and Φ_d in terms of the time τ_v spent by the atoms in the background gas between generation by ESR and ejection by the field, and V, the volume associated with the spin-up density distribution:

$$\Phi_c = c\ V/\tau_v \tag{13a}$$

$$\Phi_d = d\ V/\tau_v\ . \tag{13b}$$

Here c and d refer to the upper hyperfine state densities at $z = 0$. The expression for τ_v follows from equation (12):

$$\tau_v = (V/A)[n\uparrow(0)/n\uparrow(L_+)]\ (L_B/D_k)\ . \tag{14}$$

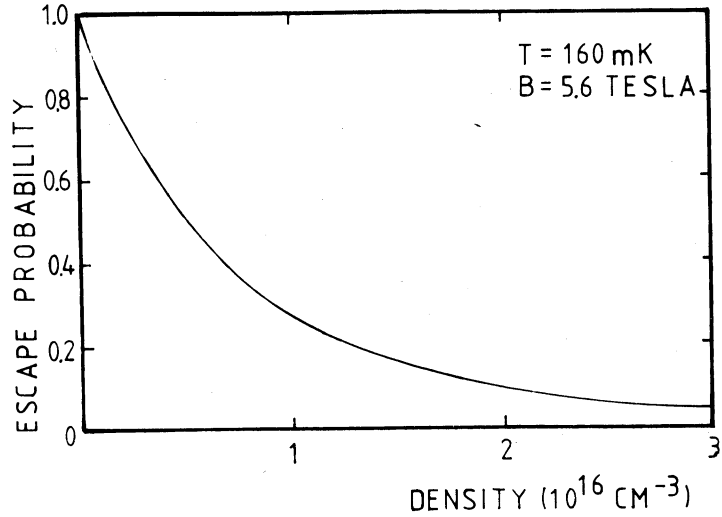

Fig. 4. Calculated escape probability for a spin-up particle versus the density of the lower hyperfine states.

The time constant τ_v is a function of the total density only. In fig. 4 we plot the probability that a spin-up particle, after generation by ESR, will be ejected (i.e. not lost by recombination with a spin-down particle). The escape probability is small if the total density exceeds a value of 10^{16} cm^{-3}. If a high flux is wanted, the total density should remain below this value.

The calculated flux of ejected particles as a function of the total density at a constant microwave power level is shown in fig. 5. A constant density ratio $n_b/n_a = 5$ has been assumed. The effect of spin-exchange relaxation is clearly visible in the fluxes at densities of 10^{15} cm^{-3} and above, where $\varphi_c/\varphi_d = 5$, the same ratio as the density ratio of the lower hyperfine states. At densities of $3\text{x}10^{13}$ cm^{-3} and below, spin exchange is of less importance, but still visible. The maximum in the fluxes displayed at high densities results from recombination between spin-up and spin-down atoms. Thus at our current power level, the maximum flux is $5\text{x}10^{13}$ sec^{-1}.

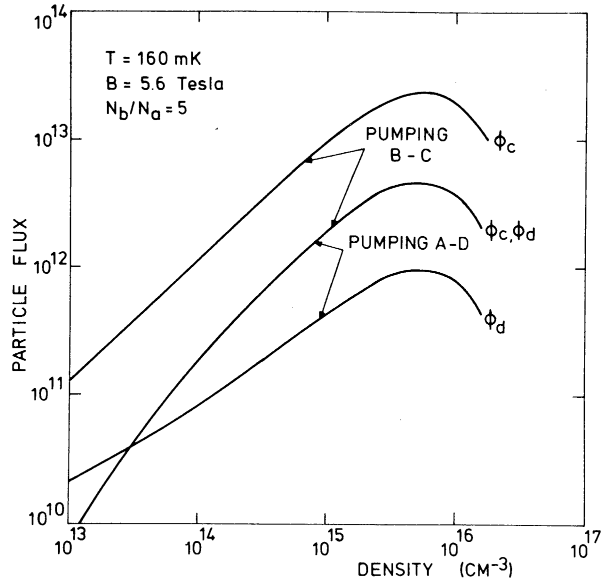

Fig. 5. Calculated flux of |c> and |d> state atoms as a function of total density and at a microwave power of 0.2 W. A density-independent ratio n_b/n_a= 5 has been assumed. Note that the difference in φ_d (pumping the b-c transition) and φ_c (pumping the a-d transition) is imperceptible on this scale.

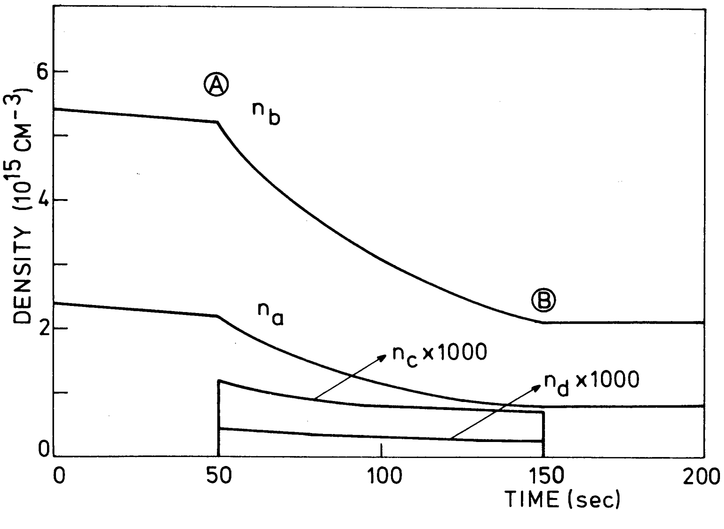

Fig. 6. Computer simulation of ESR pumping.

Solution of the rate equations

Within the approximations discussed in the last sections, equations (1a-1d) may be rewritten:

$$da/dt = -2K_{aa}\, a^2 - K_{ab}\, ab - K\, a(c + d) - W_{ad}^{ESR}\, a + G^{imp}\, (b - a) + G_{ex}\, (bd - ac) \qquad (15a)$$

$$db/dt = - K_{ab}\, ab - K\, b(c + d) - W_{bc}^{ESR}\, b - G^{imp}\, (b - a) - G_{ex}\, (bd - ac) \qquad (15b)$$

$$dc/dt = - K\, c(a + b) + W_{bc}^{ESR}\, b + G_{ex}\, (bd - ac) - c/\tau_v \qquad (15c)$$

$$dd/dt = - K\, d(a + b) + W_{ad}^{ESR}\, a - G_{ex}\, (bd - ac) - d/\tau_v\ . \qquad (15d)$$

Here a, b, c and d denote the densities at z = 0. In the above equations we neglect the differences in the effective volume of the four hyperfine states. To our estimate this introduces an error of 20 percent. We have ignored the diffusion terms in equations 15a and 15b. The values of G^{imp}, W_{ad}^{ESR} and W_{bc}^{ESR} were obtained by fitting the calculated decay curves to the experimental data. A rather large value for G^{imp} of $3x10^{-4}\ s^{-1}$ was necessary to obtain a good fit. For this reason, two-body dipolar b-a relaxation was not included in the analysis.

The above set of equations was solved with the help of a computer. Some typical results are shown in fig. 6 where we plot the densities of the four hyperfine states as a function of time. At the point A the microwave power, tuned to the |b>-|c> transition, is switched on. At B the microwave power is switched off. Soon after pumping has started, a density of |c> and |d> state atoms is built up. Similar results are found if pumping the |a>-|d> transition is simulated numerically. One finds the surprising result that ESR pumping of one of the lower hyperfine states does not change the b/a ratio, i.e. the final nuclear polarization of the lower hyperfine states turns out to be always the same, irrespective of the transition being pumped or if there is no pumping at all.

This type of behavior is a direct consequence of the spin-exchange relaxation rates, which are at least two orders of magnitude faster than all other rates. The transient behavior after switching on the microwave field may be understood as follows. Soon after one of the upper hyperfine states is created by ESR, the other is created by spin exchange; this process goes on until the net spin-exchange rate is small. The term bd-ac is driven to zero by spin exchange. Only a small fraction of the atoms is in the upper hyperfine states; consequently, the populations of the lower hyperfine states do not change very much by pumping. Spin exchange thus provides a feed-back mechanism, which locks the ratio c/d to the ratio b/a, unless the microwave power is so high, that the density in the upper hyperfine levels becomes comparable to the density in the lower hyperfine states. In our system this occurs at power levels of 1 milliWatt and above. Then the above analysis no longer applies.

Experimental results

The effects of ESR pumping were studied by measuring the density decay of the lower two hyperfine states under different pumping conditions. ESR was used both to disturb the population of the four hyperfine states and to measure the density in the lower hyperfine states. To pump one of the transitions, the magnetic field was manually tuned to resonance; the densities were measured by switching the microwave frequency between the two resonance regions and sweeping the field through resonance at constant time intervals. Since it is not possible with our ESR equipment to pump one of the transitions and perform a density determination at the same time, a pressure transducer was used to monitor the total density. A constant microwave power $P_{in} \simeq 0.2$ μW was used. This power level destroyed 5% of the total density every passage through resonance. No attempt was made to reduce this level since our signals were quite noisy.

The data were taken at a temperature of 160 milliKelvin, the walls of the sample container being covered by a ^{3}He-^{4}He mixture. Results are shown in fig. 7, where we plot the measured densities n_a and n_b and the polarization $P = (n_b - n_a)/(n_b + n_a)$ as a function of time. Three situations are compared

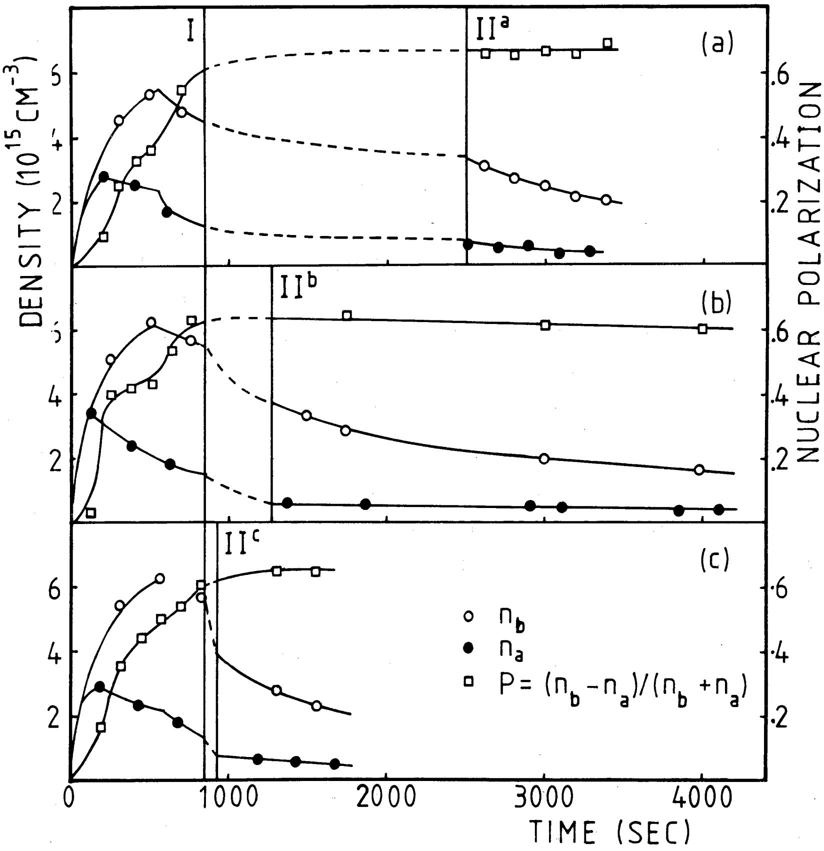

Fig. 7. Experimental results. See text for a discussion.

in this figure: no pumping (fig. 7a), pumping the $|a\rangle$-$|d\rangle$ transition (fig. 7b) and pumping the $|b\rangle$-$|c\rangle$ transition (fig. 7c).

The measurement without pumping of fig. 7a was taken for reference to separate the effect of pumping from the unwanted destruction by a density determination with ESR. After the cell is filled with a density of about 10^{16} cm^{-3} a moderate nuclear polarization ($n_b/n_a \simeq 5$) builds up in the initial portion of the decay. Starting at a total density of 6×10^{15} cm^{-3} (point I in fig. 7) the microwave power is switched off to allow for a free decay, undisturbed by ESR (dotted lines in fig. 7a). When the total density has fallen to a value of 3×10^{15} cm^{-3} (point IIa in fig. 7) the microwave power is switched on again to resume measuring the densities n_a and n_b.

At point I in fig. 7b the power is not switched off as in fig. 7a but in contrast the decay is perturbed by pumping the |a>-|d> transition in the density interval 6x10^{15} cm^{-3} - 3x10^{15} cm^{-3} (dotted line in fig. 7b). This increases the decay rate by a factor of four, the final polarization turns out to be unchanged. In fig. 7c the decay is perturbed by pumping the |b>-|c> transition in the same density interval. This results in the most rapid decay, since the rate at which spin-up particles are created is proportional to n_b and $n_b/n_a \simeq 5$. The final polarization is about the same in figs. 7a, 7b and 7c.

Our experimental results reflect the same behavior as the numerical calculations. Therefore, we attribute the observed behavior to spin-exchange relaxation. However, from our measurements no conclusion can be drawn regarding the precise value of the spin-exchange rate constant. From our numerical calculations we estimate that the maximum ejection flux was 5x10^{13} sec^{-1}, containing c and d state atoms in a ratio 5 : 1.

Possible applications of the ESR pumping technique

The model developed in this paper may be of help in evaluating the applications of ESR pumping mentioned in the introduction. Pumping the |a>-|d> transition in a fairly pure |b> state gas is likely to be followed by spin exchange, resulting in |a>-|c> pairs. This process is inhibited at sufficiently low densities (below 3x10^{13} cm^{-3} in our geometry, see fig. 2). Purifying a gas of |b> state atoms with a small |a> state impurity by pumping the |a> state is therefore restricted to low densities unless the value of L_+ is small. If we take 1 cm as a practically achievable lower bound for the width of the density distribution, then this technique will be effective up to densities of the order 10^{15} cm^{-3}. This is easily seen from fig. 2.

Generating an atomic beam by ESR pumping seems more promising. The factors affecting the particle flux and the nuclear polarization of the emerging beam are the total density, microwave power, magnetic field and geometry (field configuration). In this section we discuss how the best choice for each of these parameters may be found, to obtain the maximum particle flux.

The temperature and the field mainly affect L_{rec}. With a ^{3}He-^{4}He covered sample chamber the recombination rate will be minimum at a temperature of 200 mK[7]. At this temperature, the volume and the surface contributions to the recombination rate are equal. Our experiment was performed near this optimum, so L_{rec} cannot be made more than a factor of two longer by working at a different temperature or field. The role of the field configuration (homogeneity) is expressed via L_+. A smaller value of L_+, the width of the distribution, may be obtained by reducing the homogeneity of the field. This also reduces the ESR pumping rate, which is no problem if a high power source such as a far infrared laser or a carcinotron is available. However, in practice it will not be possible to obtain a value of L_+ much below 1 centimeter. The most important parameter governing both recombination and spin exchange is the density of the spin-down background gas. Recombination will be unimportant at densities below 3×10^{15} cm^{-3}; spin exchange will be unimportant below 10^{13} cm^{-3}. Optimizing the system allows for working at a higher density and results in a higher flux. One order of magnitude in operating density may be gained before recombination losses become appreciable.

To illustrate the above considerations, we estimate the ejection flux from a high power source. A moderate homogeneity magnet coil (inhomogeneity 1×10^{-3} in a 1 cc volume) yields a value for L_+ of approximately 1 cm for a central field of 5.6 Tesla and a temperature of 200 mK. For a density of 5×10^{16} cm^{-3} and a microwave power of 200 milliWatt the flux is 5×10^{18} sec^{-1}.

The following conclusions apply to the nuclear polarization of the emerging beam:

-pumping an ESR transition in an unpolarized or moderately nuclear spin polarized background gas of high density will result in a mixture of the two upper hyperfine states in the beam;

-|c> state atoms may live relatively long in an almost pure |b> state environment, since there are no |a> state partners for spin exchange available. Pumping the |b>-|c> transition therefore results in a doubly polarized beam of |c> state atoms if $L^c_{ex} \gg L_+$;

-pumping the |a>-|d> transition in an almost pure gas of |b> state atoms also results in a low intensity doubly polarized beam of |c> state atoms: the |d> state atoms created by ESR are quickly converted into the |c> state due to spin exchange but cannot relax back (they may relax to the |b> state by the dipolar mechanism). Thus the production of a pure |d> state beam is only possible at densities of 10^{14} cm^{-3} and below.

The following conclusions apply to the particle flux:

-a high ESR pumping efficiency favors a homogenious magnetic field, whereas a high escape probability requires a narrow density profile and thus an

inhomogeneous field;
-if the density of the background gas exceeds a certain temperature dependent value, pumping will be inefficient due to recombination.

Summary

The importance of various relaxation, recombination and diffusion processes depends on density, temperature, magnetic field and the width of the density distribution. It is elucidating to distinguish between the different regimes of these parameters by considering the characteristic lengths L_{rec}, L^c_{ex}, L^d_{ex}, and L_+, using a plot such as fig. 2. Recombination of spin-up and spin-down atoms is unimportant if $L_{rec} \ll L_+$; similar conditions hold for spin exchange with characteristic lengths L^c_{ex} and L^d_{ex}. The experiments were carried out at densities of 10^{15}-10^{16} cm^{-3}, where spin exchange is important for both upper hyperfine states and where $L_{rec} \simeq L_+$. The experimental observations may be summarized as follows: pumping one of the ESR transitions at our currently available power levels only affects the time scale of the decay, not the nuclear polarization. We attribute this behavior to spin-exchange relaxation. This is supported by numerical estimates. From the experimental results no conclusion can be drawn regarding the precise value of the spin-exchange rate constant G_{ex}. However the measurements clearly confirm that G_{ex} is large compared to all other terms.

Acknowledgements

It is a pleasure to thank O.H. Höpfner for technical support, and R. Sprik and J.J. Berkhout for assistance with the measurements. The financial support of the Stichting FOM and the Department of Energy Grant DE-FG02-85ER 45190 is gratefully acknowledged.

References

1. G.H. van Yperen, J.T.M. Walraven, I.F. Silvera,
   Phys. Rev. B30, 2386 (1984).
2. B.W. Statt, W.N. Hardy, A.J. Berlinsky and E.J. Klein,
   Journal of Low Temp. Phys. 61, 471 (1985).
3. M.W. Reynolds, I. Shinkoda, W.N. Hardy, A.J. Berlinsky,
   F.W. Bridges and B.W. Statt, Phys. Rev. B31, 7503.
4. M.W. Reynolds, I. Shinkoda, R.W. Cline and W.N. Hardy,
   Phys. Rev. B34, 4912 (1986).
5. T.O. Ninnikoski, S. Pentillä, J.M. Rieubland and A. Rijllard,
   "Polarized Proton Ion Sources", G. Roy and P. Schnor, Eds;
   AIP Conference Proceedings, p. 139.
   S. Pentillä, Thesis, University of Turku, Finland (1985).
6. D. Kleppner and T.J. Greytak, Proceedings of the 5th Int. Conf. High
   Energy Spin Physics, Brookhaven 1982, G.M. Bunce Ed.,
   AIP Conf. Proc., No. 95 (1983) p.546.
7. I.F. Silvera and J.T.M. Walraven, *Progress in Low Temperature
   Physics*, Vol. X, Chapter D, D. Brewer Ed.,
   North Holland Publ. Amsterdam (1986).
8. R. Jochemsen, M. Morrow, A.J. Berlinsky and W.N. Hardy,
   Phys. Rev. Lett. 47, 852 (1981).
9. G.H. van Yperen, A.P.M. Matthey, J.T.M. Walraven and I.F. Silvera,
   Phys. Rev. Lett. 47, 800 (1981).
10. J.P. Bouchaud and C. Lhuillier, J. Phys. 46, 1781 (1985).
11. R. Sprik, J.T.M. Walraven and I.F. Silvera,
    Phys. Rev. B32, 5668 (1985).
12. A.J. Berlinsky and B. Shizgal, Can. J. Phys. 58, 881 (1980).
    M. Morrow and A.J. Berlinsky, Can. J. Phys. 61, 1042 (1983).
13. J.J. Berkhout, E.J. Wolters, R. van Roijen, J.T.M. Walraven,
    Phys. Rev. Lett. 57, 2387 (1986).

Summary

The subject of this thesis is an experimental investigation of the stability of electron-spin polarized atomic hydrogen at low temperatures with respect to recombination towards the molecular state. A systematic study was carried out of the decay rate as a function of temperature, magnetic field and the density of the sample.

Chapter I provides the theoretical framework for the experiments. Single atom properties, pair interactions and the interaction between a hydrogen atom and a liquid helium surface are briefly reviewed. An overview is given of all processes, that may eventually lead to recombination, with emphasis on those that are important at densities between 10^{14}-10^{16} cm^{-3}, the density range covered in the experiments. Recombination results from a collision between two atoms with antiparallalel electron spin and a third body to conserve energy and momentum. If the sample is electron-spin polarized, the atoms may exist in two hyperfine states |a> and |b>. Due to the hyperfine interaction between the proton and the electron, an |a> state atom has a small magnetic field dependent probability to have its electron spin reversed. Recombination is likely to occur at the surface, surrounding the sample and acting as a third body. Knowledge of the atom-surface interaction is therefore of vital importance.

Chapter II deals with experimental techniques. The cryogenic part of the apparatus has to handle large amounts of heat, produced by the sample or transported to the low temperature parts by the superfluid helium film. Large amounts of heat may be transported over long distances at low temperatures using a heatpipe, filled with helium-3. A description is given of the construction and the operation of a sensitive capacitive transducer, measuring the pressure of the sample. Pressure measurement has become a common tool in atomic hydrogen research. Small semiconductor bolometers were found to serve various purposes: they can detect the sample at extremely low densities, destroy the sample (which is sometimes necessary), and may provide information about the thickness of the helium film and its helium-3 content.

Most of the experimental results and their interpretation are covered in chapter III. Two series of experiments are described. The first series

demonstrated the feasibility of pressure measurement in the study of the recombination kinetics, and presented the direct proof of the gaseous nature of spin polarized atomic hydrogen. From the temperature dependence of the second order rate constant, a value of the binding energy of 0.89 Kelvin was determined. The rate constant was found to be proportional to B^{-2}, consistent with the model described in chapter I. In the second series, the pressure decay was studied in a broader temperature and field range, and a better defined geometry. Electron-spin resonance was used to verify that both hyperfine states were equally populated. The temperature and field dependence appears to be well understood in terms of the before mentioned model. Under suitible conditions, the recombination results from a resonance process. The observed change of the rate constant with film-thickness is somewhat obscure. A possible relation with the roughness of the substrate underneath has been explored, but the evidence is not conclusive. Using a combination of ESR and pressure measurement, both the density and the temperature of the sample may be determined simultaneously. We find that below 200 mK a substantial temperature difference may develop between the gas and the wall of the sample container. The bottlenecking factor in the heat transfer turns out to be the Kapitza resistance between the helium film and the solid substrate. Finally, an attempt was made to observe spin waves in the ESR spectrum, with a negative result.

Chapter IV is exclusively devoted to ESR pumping experiments. ESR is used to create a small non-equilibrium occupation of the upper hyperfine states. The resulting spin-up atoms will be expelled by the field gradient, if not lost by recombination. The decay was studied experimentally under different pumping conditions. The results are compared with a model, incorporating various processes such as diffusion, recombination and relaxation. The role of spin-exchange relaxation was found to be dominant. It follows from the analysis that generating a spin-polarized beam of hydrogen atoms by ESR pumping is feasible. The model may be used to design a source, based on this technique.

Samenvatting

Het onderwerp van dit proefschrift is een experimenteel onderzoek naar de stabiliteit van spin gepolariseerde atomaire waterstof. Onder normale condities gaat dit door recombinatie snel over in de moleculaire toestand. Informatie over de destabilisatie processen kan worden verkregen door de snelheid van het dichtheidsverval systematisch te bestuderen als functie van de temperatuur, het magneetveld en de dichtheid van het monster.

Hoofdstuk 1 beschrijft de theoretische achtergronden van de experimenten. Behandeld worden achtereenvolgens de statische eigenschappen van het waterstof atoom, de wisselwerking tussen de atomen onderling en de wisselwerking tussen het waterstofatoom en het oppervlak van vloeibare helium. Tenslotte wordt een overzicht gegeven van de processen, die uiteindelijk tot recombinatie kunnen leiden, waarbij de nadruk ligt op processen die werkzaam zijn in het dichtheidsgebied tussen 10^{14}-10^{16} cm^{-3}. In dit dichtheidsgebied vonden de meeste experimenten plaats. Recombinatie is het resultaat van een botsing tussen twee atomen met antiparallelle electron spins en een derde deeltje, teneinde aan de behoudswetten van energie en impuls te voldoen. Als de electron spins van het monster gepolariseerd zijn, kunnen de atomen voorkomen in twee hyperfijn toestanden $|a\rangle$ en $|b\rangle$. Ten gevolge van de hyperfijn interaktie tussen het proton en het electron, bestaat er, afhankelijk van het aangelegde magneetveld, een kleine kans dat de electron spin van een atoom in de $|a\rangle$ toestand een omgekeerde orientatie heeft; dit staat een volledige polarisatie in de weg. Recombinatie treedt vooral op aan de wanden, waarbinnen het monster is opgesloten. Kennis van de wisselwerking tussen het waterstof atoom en het oppervlak is daarom van vitaal belang.

Experimentele technieken worden behandeld in hoofdstuk 2. Het cryogene deel van de apparatuur moet grote hoeveelheden warmte kunnen afvoeren, die enerzijds het gevolg zijn van de warmte die bij de recombinatie van het monster vrijkomt, en anderzijds naar het lage temperatuur deel van de opstelling getransporteerd worden als gevolg van de aanwezigheid van een superfluide helium film. Een efficiente manier om warmte te transporteren bij lage temperaturen is het gebruik van een warmtepijp, gevuld met helium-3. Er wordt een beschrijving gegeven van de constructie en de werking van een gevoelige capacitieve opnemer, die de druk van het monster meet. Drukmeting wordt inmiddels algemeen gebruikt bij het atomaire waterstof onderzoek. Kleine halfgeleider bolometers bleken voor verschillende doeleinden geschikt te zijn: ze kunnen het monster detecteren bij extreem lage dichtheden, het monster vernietigen (hetgeen soms gewenst is), en kunnen informatie verschaffen over de dikte van de helium film en de mate waarin deze verontreinigd is met helium-3.

De meeste experimentele resultaten en de interpretatie ervan zijn vermeld in hoofdstuk 3. Er worden twee series experimenten beschreven. De eerste serie demonstreerde het nut van drukmetingen bij de bestudering van de recombinatiekinetiek, en leverde het direkte bewijs dat een monster van spin gepolariseerde atomaire waterstof zich in de gasvormige toestand bevindt. Uit de temperatuurafhankelijkheid van de tweede orde vervalconstante kon de waarde van de bindingsenergie van een waterstofatoom, gebonden aan een vloeibaar helium-4 oppervlak worden bepaald. Dit leverde een waarde van 0.89 Kelvin. De gemeten vervalconstanten waren bovendien evenredig met B^{-2}, hetgeen consistent is met een model, beschreven in het eerste hoofdstuk. Bij de tweede serie experimenten, werd het drukverval in een breder temperatuur en magneetveld bereik bestudeerd, en werd gebruik gemaakt van een beter gedefinieerde geometrie. Electron spin resonantie werd gebruikt om te verifieren dat de beide hyperfijn toestanden gelijk bezet waren. De temperatuur- en veldafhankelijkheid blijken goed beschreven te worden in termen van het hiervoor beschreven model. Onder bepaalde omstandigheden is de recombinatie het gevolg van een resonant proces. Niet duidelijk is het waargenomen verband tussen de vervalsnelheid en de dikte van de heliumfilm. Er is gezocht naar een mogelijke relatie met de ruwheid van het substraat onder de film, dit leidde echter niet tot een sluitende conclusie. Gebruik makend van een combinatie van ESR en drukmeting kunnen tegelijkertijd de dichtheid en de temperatuur van het monster worden bepaald. Het blijkt dat bij temperaturen lager dan 200 mK er een substantieel temperatuurverschil optreedt tussen het gas en de wand van de cel. Uit de metingen wordt geconcludeerd dat de faktor die het warmtetransport beperkt de Kapitzaweerstand is tussen de helium film en het onderliggende substraat. Tenslotte werd een poging gedaan om spin golven in het ESR spectrum waar te nemen, hetgeen een negatief resultaat opleverde.

Hoofdstuk 4 is gewijd aan ESR pomp experimenten. ESR wordt gebruikt om een kleine niet evenwichtsbezetting van de hoogste hyperfijn toestanden te creeren. De resulterende atomen met de spin omhoog zullen worden weggeschoten door de veldgradient, als ze tenminste niet verloren gaan door recombinatie. Het verval werd bestudeerd onder verschillende pompcondities. De resultaten worden vergeleken met een model, waarin de invloed van verschillende processen als diffusie, recombinatie en relaxatie wordt meegenomen. Het blijkt dat spin-exchange relaxatie een dominante rol speelt. Uit de analyse van de experimenten kan worden geconcludeerd dat het genereren van een spin gepolariseerde atomaire bundel door middel van ESR pompen haalbaar is. Het model kan worden gebruikt om een bron die volgens deze techniek werkt te ontwerpen.

NAWOORD

Resteert mij nog dank te betuigen aan al diegenen, die op een of andere wijze een bijdrage hebben geleverd aan de totstandkoming van dit proefschrift.

In het bijzonder wil ik hierbij noemen mijn promotor Ike Silvera en mijn co-promotor Jook Walraven. Door hun enthousiasme voor het werk en intensieve coaching hebben ze een substantiele bijdrage geleverd aan mijn ontwikkeling als experimenteel fysicus. Door het vaak teleurstellend werk dat ze in de jaren voorafgaand aan mijn onderzoek verrichten, hebben ze voor mij een comfortabel bed gespreid. Ik kwam juist binnen op het moment dat er geoogst kon worden, menig promovendus zou z'n vingers aflikken bij deze unieke mogelijkheden. De nacht waarin het eerste monster van spin gepolariseerde atomaire waterstof werd geboren zal me altijd bijblijven. De periode hierna werd gekenmerkt door een grote verscheidenheid aan experimenten, waarbij flink werd doorgewerkt om de concurrentie een stap voor te blijven. Het heilig vuur brandde tijdens de weekenden en ook vaak 's nachts. Op de kritieke momenten waren Ike en Jook op de werkvloer aanwezig, daarbij niet het handwerk schuwend, als dat nodig was. Jook ben ik bijzonder erkentelijk voor de wijze waarop hij me stimuleerde om de resultaten op te schrijven toen ik reeds een drukke baan in het onderwijs had, en de accuratesse waarmee hij de diverse concepten schoonde van onnauwkeurigheden.

Ik heb plezierig samengewerkt met mijn collega-promovendi Gert van Yperen, Kauko Salonen, Rudolf Sprik en Jaap Berkhout, en de studenten Tom Kerkhoven, Hans van Zwol en Erik Salomons. Ad Lagendijk en Victor Goldmann steunden de groep op het gebied van de theorie. Al met al een stimulerend gezelschap waaruit een ware waterval van ideeën en resultaten uit voortkwam. Op vrijdagmiddag leefden wij onze frustaties van de week uit op de groepsbespreking. De rol van spreker op zo'n bijeenkomst kostte mij vaak meer moeite dan het hanteren van een klas met Mavo leerlingen.

Dit werk zou niet mogelijk zijn geweest zonder de ondersteunende faciliteiten op het lab, zoals de instrumentmakerij, de electronische werkplaats en de glasblazerij. Ruud Scheltema assisteerde bij de ontwikkeling van de eerste drukmeter. Otto Höpfner heeft met vernuft diverse cellen en andere toebehoren voor de experimenten gebouwd, en verleende frequent een 'klaar terwijl U wacht' service. Bert Zwart ondersteunde bij vacuumtechnische problemen. Voor materiaalkundige problemen kon ik altijd terugvallen op Hugo

Schlatter en Ton Riemersma. Herman Pothoven en Nico Jonker zorgden voor in totaal enige duizenden liters vloeibare helium. Voor electronische problemen kon ik terecht bij Ad Veen, Charley Alderhout en Paul Langemeyer. Mariet Bos verzorgde de nodige correspondentie en zorgde dat de publicaties snel de deur uitgingen. Een groot aantal van de tekeningen zijn van de hand van Ben Leonards.

Tenslotte wil ik al diegenen die niet met name zijn genoemd van harte bedanken.

Omslagontwerp: Matthy Piebes
Lithografie omslag: Michel Stultiëns